Spring 2015

Macrophage COX-2 As a Target For Imaging And Therapy of Inflammatory Diseases Using Theranostic Nanoemulsions

Sravan Kumar Patel

MACROPHAGE COX-2 AS A TARGET FOR IMAGING AND THERAPY OF INFLAMMATORY DISEASES USING THERANOSTIC NANOEMULSIONS

A Dissertation

Submitted to the Mylan School of Pharmacy

Duquesne University

In partial fulfillment of the requirements for

the degree of Doctor of Philosophy

By

Sravan Kumar Patel

March 2015

MACROPHAGE COX-2 AS A TARGET FOR IMAGING AND THERAPY OF INFLAMMATORY DISEASES USING THERANOSTIC NANOEMULSIONS

By

Sravan Kumar Patel

Approved March 12, 2015

Dr. Jelena M. Janjic Associate Professor of Pharmaceutics Graduate School of Pharmaceutical Sciences (Committee Chair)	Dr. Carl A. Anderson Associate Professor of Pharmaceutics Graduate School of Pharmaceutical Sciences (Committee Member)
Dr. Ira S. Buckner Associate Professor of Pharmaceutics Graduate School of Pharmaceutical Sciences (Committee Member)	Dr. Peter L.D. Wildfong Associate Professor of Pharmaceutics Graduate School of Pharmaceutical Sciences (Committee Member)
Dr. John A. Pollock Professor of Biological Sciences Bayer School of Natural and Environmental Sciences (Committee Member)	Dr. Lisa C. Rohan Associate Professor, Department of Pharmaceutical Sciences, School of Pharmacy, University of Pittsburgh (Committee Member)
James K. Drennen, III, Ph.D. Associate Professor of Pharmaceutics Associate Dean for Graduate Programs and Research Mylan School of Pharmacy	J. Douglas Bricker, Ph.D. Dean, Mylan School of Pharmacy and the Graduate School of Pharmaceutical Sciences

ABSTRACT

MACROPHAGE COX-2 AS A TARGET FOR IMAGING AND THERAPY OF INFLAMMATORY DISEASES USING THERANOSTIC NANOEMULSIONS

By

Sravan Kumar Patel

March 2015

Dissertation supervised by Dr. Jelena M. Janjic

Personalized medicine can be an approach to address the unsatisfactory treatment outcomes in inflammatory conditions such as cancer, arthritis, and cardiovascular diseases. A common feature of chronic diseases is the infiltration of pro-inflammatory macrophages at the disease loci. Infiltrating macrophages have been previously utilized for disease diagnosis. These features suggest that macrophages can be broadly applicable targets for simultaneous therapy and diagnosis. Cyclooxygenase-2 (COX-2), an enzyme involved in the biosynthesis of a lipid inflammatory mediator, prostaglandin E_2 (PGE_2), is over expressed in macrophages infiltrating the pathological site. Inhibition of PGE_2 leads to reduced inflammation, pain and macrophage infiltration. To utilize macrophages for the purpose of simultaneous therapy and diagnosis, we proposed to integrate therapeutic and imaging capabilities on a single nanomedicine platform, referred as theranostics. A

stable ^{19}F MRI visible nanoemulsion platform was developed, incorporating celecoxib for COX-2 inhibition and near-infrared fluorescent dye(s) for fluorescence imaging. We hypothesized that inhibition of COX-2 in macrophages using a theranostic nanoemulsion will reduce the inflammation (and pain), and that this response can be visualized by monitoring changes in macrophage infiltration. *In vitro* characterization demonstrated that the theranostic displays excellent stability with no toxicity, and significant uptake in macrophages. Furthermore, it delivers celecoxib to macrophages and reduces PGE_2 production from these cells. *In vivo* studies in a murine paw inflammation model showed nanoemulsion presence at the inflamed site, specifically in COX-2 expressing macrophages compared to neutrophils. Supporting our hypothesis, celecoxib delivered through a nanoemulsion demonstrated time-dependent reduction in fluorescence from the inflamed paw, indicative of reduced macrophage infiltration. In a neuropathic pain model, celecoxib delivered to macrophages led to reduced pain concomitant with reduced macrophage infiltration at the inflamed site compared to free drug control (cross reference: Kiran Vasudeva, Dissertation, 2015). In conclusion, inhibition of COX-2 in macrophages using theranostic nanoemulsions proves to be an effective and generalized strategy facilitating simultaneous therapy and diagnosis, which can be applied to many chronic diseases. The diagnostic information during therapy can be used to tailor the treatment and reduce patient variability leading to personalized medicine.

DEDICATION

This dissertation is dedicated to my parents, Sreedevi and Veeresham, my brother, Arun, and my sisters, Sindhuja and Aishwarya.

ACKNOWLEDGEMENT

This work would not have been possible without the help of family, friends and colleagues. I would like to take this opportunity to thank those who helped shape my life professionally and personally at Duquesne University.

I am extremely grateful to my advisor Dr. Jelena M. Janjic, for providing me with the opportunity to pursue doctoral study in a highly collaborative environment. Her guidance, training, vision, and constructive criticism helped me face academic challenges successfully and grow professionally as a confident person. I will always remember and cherish the professional and personal support I received from her, when I needed the most.

I am immensely thankful to all my committee members for offering their insightful guidance, and valuable time in completion of my doctoral dissertation. I sincerely appreciate the valuable suggestions and training offered by Dr. John A. Pollock. I would like to offer special thanks to Dr. Carl A. Anderson for his valuable guidance throughout my time at Duquesne University, in courses as well as research. I would like to thank Dr. Lisa Rohan for valuable advice and for generously allowing me to utilize facilities in her laboratory at University of Pittsburgh. My other committee members, Drs. Buckner and Wildfong shaped my understanding of pharmaceutical field through their courses. I could always knock on their door for any technical questions and they graciously supported me.

I am indebted to the friendship and support of my lab members, Claire O'Hanlon, Yang Zhang, Konjit Amede, Meredith O'Hear, Robert Tunney, Jr., Simon George,

Jonathan, Xun Yang, Gregory Mountain, Christina Bagia, Irenej Jeric, Sherlock Lu, and Michelle Herneisey. My work has been a collaborative effort for which I am thankful to all the friends and collaborators, Drs. Wissam Beaino and Carolyn Anderson, Kiran Vasudeva, Muzamil Saleem, Dr. Anthony Balducci, Michael J. Patrick, Dr. Kevin Hitchens, Bratislav Janjic, Virgil Simpleanu, Haibing Teng, Dr. Gayathri Withers, and Dr. Lauren Ernst, without whom this work would not have been possible. Special acknowledgements go to Dr. Wilson S. Meng for valuable suggestions towards my research.

I will always be indebted to my friends, who were practically my family at Duquesne University for their encouragement and constant support. Special thanks to Sneha Potdar, Dipy Vasa, and Darshini Shah for their constant support and love. I thank Namita Dalal, Shikhar Mohan, Anik Alam, Vishwa Shah, Sapna Jaiswal, Mayur Parmar, Balasunder Dodda, Ravi Kumar Vyas, Karim Kutchi, Harsha Rathi, Rohith Kashyap, Apurva Kulkarni, and Somraj Gosh.

I extend my acknowledgements to Drs. Diane Rhodes and Joyce Kossol for providing me with necessary training to teach pharmacy labs. I am thankful to Graduate School of Pharmaceutical Sciences and Dr. James K. Drennen, III for providing me with financial support as teaching assistant. Thanks to Ms. Jackie Farrer, Ms. Deb Wilson, Ms. Mary Caruso, and Ms. Nancy Hosni for taking care of the administrative work and timely reminder of important events.

Special thanks to Carroline Lobo, for her love, support, patience, and friendship.

Finally, I thank my parents and family members. This dissertation is the result of their blessings, relentless support, and love.

TABLE OF CONTENTS

LIST OF TABLES

Page

LIST OF FIGURES

Page

LIST OF ABBREVIATIONS

AA	Arachidonic Acid
AD	Alzheimer's Disease
ANOVA	Analysis of Variance
^{19}F MRI	^{19}F Magnetic Resonance Imaging
CatB	Cathepsin-B
CAM	Cell Adhesion Molecule
CD	Cluster of Differentiation
CFA	Complete Freund's Adjuvant
CG	Carrageenan
COPD	Chronic Obstructive Pulmonary Disease
COX-2	Cyclooxygenase-2
CrEL	Cremophor® EL
CXBNE	Celecoxib Nanoemulsion
DFNE	Drug-free Nanoemulsion
DiD	1,1'-Dioctadecyl-3,3,3',3'-Tetramethylindodicarbocyanine Perchlorate
DiR	1,1'-Dioctadecyl-3,3,3',3'-Tetramethylindotricarbocyanine Iodide
DMSO	Dimethyl Sulfoxide
CT	Computed Tomography
DAMPs	Damage-associated Molecular Patterns
DC	Dendritic Cell

DIAD	Diisopropylazodicarboxylate
DLS	Dynamic Light Scattering
DPBS	Dulbecco's Phosphate-buffered Saline
ECM	Extracellular Matrix
ELISA	Enzyme Linked Immunosorbent Assay
Em	Emission
EPR	Enhanced Permeability and Retention
Ex	Excitation
FBS	Fetal Bovine Serum
FITC	Fluorescein Isothiocyanate
FSC	Forward Scatter
Gd	Gadolinium
GNR	Gold Nanorods
HPLC	High Performance Liquid Chromatography
IBD	Inflammatory Bowel Disease
IONP	Iron Oxide Nanoparticle
i.v.	Intravenous
LOD	Limit of Detection
LOQ	Limit of Quantitation
LPS	Lipopolysaccharide
MCP-1	Monocyte Chemoattractant Protein-1
MI	Myocardial Infarction
MMP	Matrix Metalloproteinase

MRI	Magnetic Resonance Imaging
NIR	Near-infrared
NIRF	Near-infrared Fluorescence
NMR	Nuclear Magnetic Resonance
NO	Nitric Oxide
NP	Nanoparticle
NSAIDs	Nonsteroidal Anti-inflammatory Drugs
OR	Ostwald Ripening
O/W	Oil-in-Water
P105	Pluronic® 105
P123	Pluronic® 123
PAMPs	Pathogen-associated Molecular Patterns
PDI	Polydispersity Index
PDIw/2	Half-width of Polydispersity Index
PDT	Photodynamic Therapy
PEG	Polyethylene glycol
PEO	Polyethylene Oxide
PET	Positron Emission Tomography
PFC	Perfluorocarbon
PFC-HC	Perfluorocarbon-Hydrocarbon
PFCE	Perfluoro-15-crown-5-ether
PFOB	Perfluorooctyl bromide
PFPE	Perfluoropoly (ethylene glycol) ether

PFTE	Perfluoro-*tert*-butyl ether
PGE_2	Prostaglandin E_2
PPO	Polypropylene Oxide
PTT	Photothermal Therapy
RA	Rheumatoid Arthritis
RES	Reticuloendothelial System
RFU	Relative Fluorescence Units
ROI	Region of Interest
ROS	Reactive Oxygen Species
RSD	Relative Standard Deviation
RT	Room Temperature
s.c.	Subcutaneous
SD	Standard Deviation
SEM	Standard Error of Mean
siRNA	Small interfering Ribonucleic Acid
SSC	Side Scatter
TAM	Tumor Associated Macrophages
TFA	Trifluoroacetic Acid
TNF-α	Tumor Necrosis Factor-α
USPIO	Ultrasmall Paramagnetic Iron Oxide
W/O	Water-in-Oil
^{90}Y	Yttrium-90

1 Macrophages as targets for simultaneous diagnosis and therapy of inflammatory diseases

1.1 Statement of the problem

Inflammation is involved in the pathogenesis of many common diseases such as cancer, rheumatoid arthritis (RA), obesity, cardiovascular-related ailments, chronic obstructive pulmonary disease (COPD), asthma, inflammatory bowel disease (IBD), diabetes, Alzheimer's, and infection-related diseases.[1-3] Although it is beneficial in defending the body from injury or infection, unresolved inflammation can lead to substantial tissue injury, which is involved in the initiation, promotion and progression of diseases.[1,3,4] Inflammatory diseases are associated with considerable economic burden. In 2003, the Centers for Disease Control and Prevention reported that total expenditures due to arthritis and other rheumatic disorders were $128 billion, which was equivalent to 1.2% of the 2003 United States gross domestic product.[5] The direct and indirect costs attributable to asthma increased by six percent from $53 billion in 2002 to $56 billion in 2007.[6] In 2010, cardiovascular diseases were estimated to have total costs of $444 billion.[7] Figure 1.1 shows the prevalence of heart diseases, diabetes and asthma in the United States.

Methods to effectively intercept pathways that lead to chronic inflammation are under intense development. While substantial progress has been made in the development of new drugs, inflammatory disease treatment and management still face significant problems. Inter- and intra-patient variability is one of the major factors contributing to the failure of current treatment approaches.[8-10] The traditional treatment strategies rely on

diagnosis of the disease and administration of the appropriate therapy based on the severity of the disease. Disease severity is obtained from generalized diagnostic methods and other patient-specific parameters such as body surface area, weight, and past and current medication. Although the treatment is, in a way, tailored to the patient based on the diagnostic profile, often times a great variability in efficacy is observed between patients leading to the failure of the treatment. This variability could be attributed to the inhomogeneity transpiring at the molecular level in disease pathogenesis i.e. differences in protein expression, genetic predisposition, resistance to therapy, and other similar factors. For example, inflammatory biomarkers detected in COPD show significant variability between patients.[11] Additionally, RA affecting synovial tissue in multiple joints can manifest as similar clinical symptoms in patients.[12] However, marked variability in leukocyte infiltration and cytokine profile has been observed in their synovial tissues.[13] This could be the reason for the variable clinical response to anti-inflammatory drugs such as infliximab, and etanercept, which reduce the inflammatory cytokine, tumor necrosis factor-α (TNF- α). Inter- and intra-patient variability can also be a result of variable pharmacokinetics among patients as observed for infliximab treatment.[14,15]

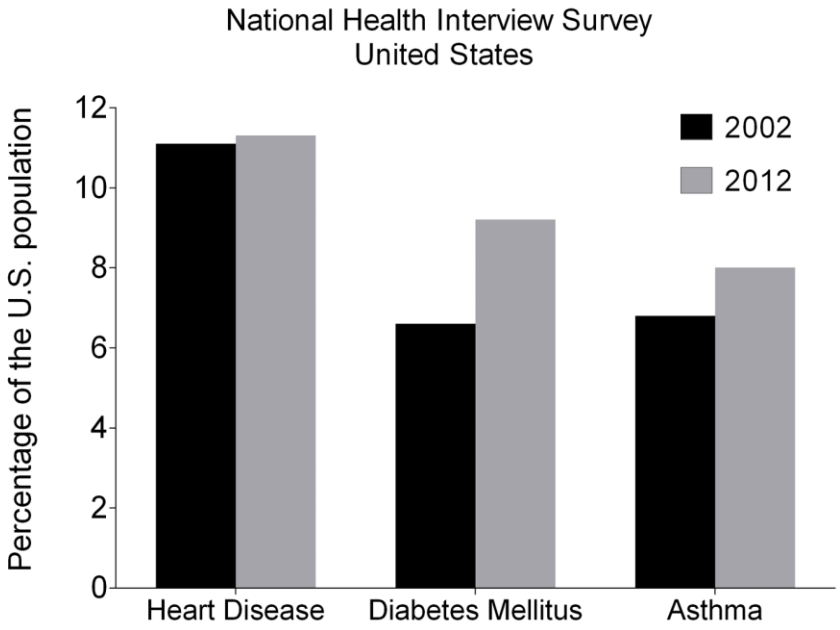

Figure 1.1. Self-reported presence of chronic diseases in the United States.

The above figure shows the prevalence of major inflammatory diseases in the United States according to the results of the National Health Interview Survey (2002 and 2012).[16,17] The numbers represent the percentage of people who had ever been told by a doctor or other health professional that they had heart diseases, diabetes mellitus or asthma.

Therefore, the traditional model of "one drug for all" has proven sub-optimal, at least for chronic diseases, and a paradigm shift has been observed towards patient-tailored treatment methods. Rapid advancements in genomics has led to the utilization of genetic information to stratify patient population known to respond to the therapy to increase efficacy and reduce unwanted side effects. This treatment model is referred to as personalized medicine.[12,18] According to the U.S. Food and Drug Administration,[19] personalized or precision medicine is described as "the right patient with the right drug at the right dose at the right time", and "the tailoring of medical treatment to the individual characteristics, needs and preferences of a patient during all stages of care, including

prevention, diagnosis, treatment and follow-up." For example, breast cancer presents in different forms, where certain patients do not respond to therapies due to changes in molecular expression of biomarkers.[20] These differences among patients are now recognized and treatment strategies are tailored leading to personalization of treatment. For example, treatment of metastatic breast cancer patients diagnosed positive for human epidermal growth factor receptor 2 (HER2) with an anticancer drug, Herceptin® (Trastuzumab), specific for these receptors increased the efficacy. Therefore, development of dedicated therapeutic interventions based on specific disease markers (companion diagnostics) is a new way of achieving the goal of personalized inflammatory diseases treatment.

The approach of combining a biomarker or a diagnostic method to tailor the therapy is referred to as "theranostics".[21] Theranostics are also defined as an integration of therapeutic and diagnostic or imaging functionalities on a single platform that can diagnose disease, deliver drugs and monitor therapy leading to individualized treatment.[18] In this dissertation, the latter definition is used to refer to theranostics. Nanotechnology has been central in the development of theranostics because therapeutic and diagnostic components can be integrated together using nanoparticles (NPs).[22] NPs offer several advantages such as high surface-area-volume ratio to obtain high loading of drug and imaging agents. They have been functionalized to increase blood circulation time by coating the surface with hydrophilic polymers such as polyethylene glycol (PEG).[23] Additionally, NPs can be functionalized to modulate the drug release based on environmental stimuli such as pH, temperature, enzymes, and redox potential, and their use can increase uptake in specific cells.[24] Due to their tunable size and surface

properties, anatomical and physiological changes during inflammation can be exploited for targeted NP accumulation, namely through leaky vasculature by enhanced permeability and retention (EPR) phenomenon and through utilization of macrophages' disease-homing characteristic.[25,26]

These multifunctional NPs have been utilized to longitudinally visualize bioaccumulation in a live animal and *ex vivo* in tissue samples, assess cellular uptake kinetics, optimize the physicochemical aspects of theranostics for desired results, and guide therapy based on imaging i.e. image-guided surgery and phototherapy.[2,18] The biodistribution information could guide clinical decision making such as continuing with therapy, changing dose or switching to a different therapy early in the treatment process. These entities can be assumed analogous to therapeutic radionuclides. For example, TheraSphere® technology uses microspheres containing radioactive Yttrium-90 (^{90}Y) to treat inoperable liver carcinoma.[27,28] These microspheres are delivered to liver through intra-arterial catheter-based delivery, where the internal radiation released by ^{90}Y kills the cancer cells. Because microspheres can be detected by positron emission tomography/computed tomography (PET/CT), their liver distribution can be visualized to identify poorly implanted tumor regions and assess treatment options.[27]

In addition to visualizing biodistribution, a significant challenge lies in monitoring the therapeutic response with theranostic NPs. There is a need to monitor the effectiveness of therapy because disease environment can change during therapy and/or develop resistance during therapy, leading to ineffective treatment. Cellular and molecular biomarkers are ever changing spatially and temporally during the disease pathogenesis and treatment. One particular mechanism relevant to inflammatory diseases

is the development of drug resistance observed in cancer, infectious diseases and RA.[20,29,30] The development of drug resistance in these diseases could vary among patients. Another example involves observing reduction in macrophage infiltration or lack thereof in response to anti-rheumatic drug therapy in RA.[29] Macrophages exacerbate the disease, so it is conceivable that an ineffective drug therapy would fail to cause a reduction in macrophage infiltration. This issue, if detected early, could guide clinicians to change the drug dose or therapy. Identification of these dynamics and adjustment of therapeutic interventions based on real-time therapy response early in the treatment process could, thereby, save time and increase patient outcomes.

Current theranostic NPs provide crucial biodistribution information. However, they have not been utilized to monitor therapeutic response. Therefore, the next step forward in the existing model of personalized medicine is personalizing the treatment while the therapy is ongoing. Figure 1.2 illustrates how theranostic NPs can help realize the goal of concurrent therapy and therapy monitoring.[31] Accumulation of theranostic at the target site can be quantified to define dosing regimen for successive doses. For example, increase the dose if the accumulation leads to sub-therapeutic drug concentration. The imaging aspect can also be used for image-guided therapy such as delivering light precisely to the diseased areas in photo-based therapies. Additionally, if the theranostic can detect spatio-temporal changes in inflammation during therapy (based on the changes in imaging information), effective clinical decision-making regarding the dose adjustments or switching to an alternate therapy can be made, early in the treatment strategy. Essentially, the imaging component of the theranostic is utilized to assess biodistribution as well as monitor the efficacy of the therapeutic intervention. These

proposed roles of theranostic could achieve personalized medicine by monitoring response to the therapy in individual patients and accordingly adjust doses and switch to alternate therapies.

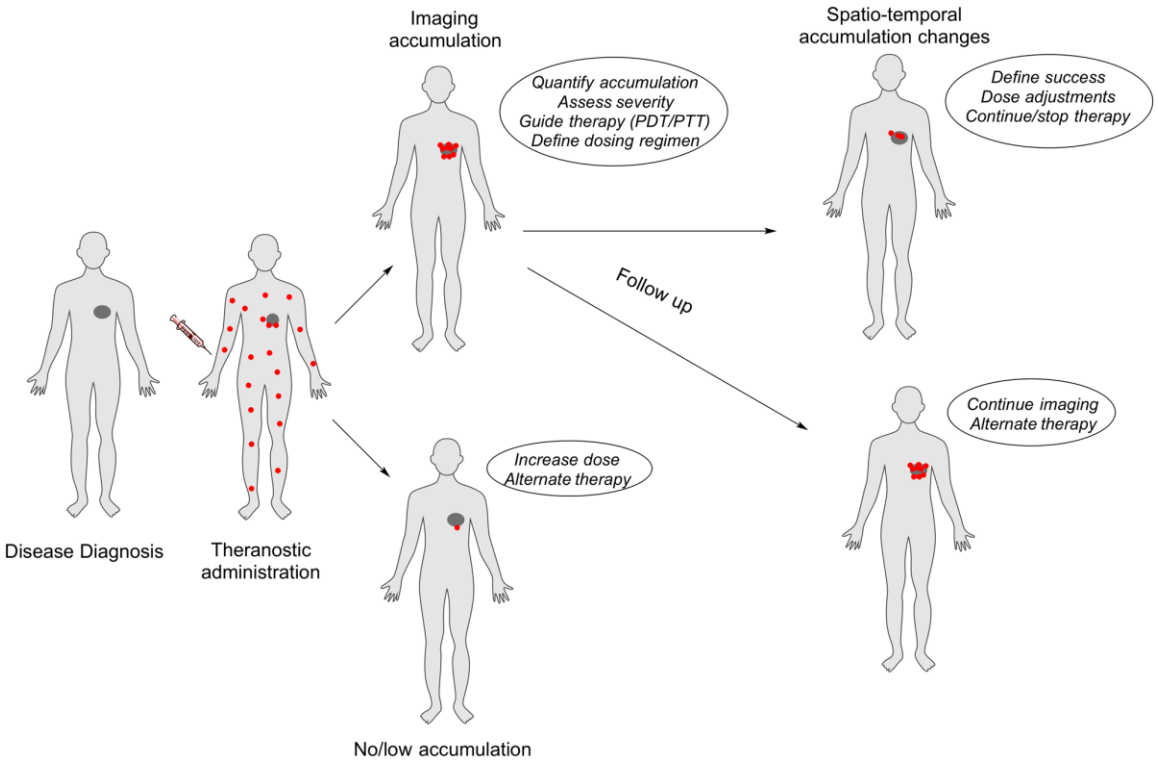

Figure 1.2. Schematic showing proposed role of theranostics in personalized treatment.

Text in the ellipse shows the clinical decision-making possibilities based on the diagnostic information obtained from theranostic functionalities. Inspired from Moore *et al*.[31]

In this dissertation, we achieved drug response monitoring using theranostics by harnessing the natural pathophysiological mechanisms of macrophages, namely their phagocytic potential and disease-homing properties. Macrophages are widely investigated for simultaneous imaging and therapy in inflammatory diseases using

theranostics.[2] These cells migrate to the injured site in response to chemokines and cytokines released during inflammation and participate in pro-inflammatory processes. Thus, theranostics can be delivered to these cells to suppress the pro-inflammatory activity and simultaneously image their infiltration. Delivering theranostics to macrophages is possible because they are naturally phagocytic and readily internalize NPs.[32] Current theranostics act by either depleting macrophages or reducing their inflammatory activity.[2] Due to the aggressive nature of macrophage depletion, which could lead to toxicities, theranostics inhibiting inflammatory mediators produced by macrophages is a safer and more effective approach.

One of the key enzymes expressed by inflammatory macrophages is cyclooxygenase-2 (COX-2). COX-2 is overly expressed in all the diseases with an inflammation component, where it contributes to disease pathogenesis and is a target for many clinically used non-steroidal anti-inflammatory drugs (NSAIDs).[33] Celecoxib, a selective COX-2 inhibitor has shown preclinical and clinical efficacy in cancer, RA, neurological disorders, and atherosclerosis[34-40] through its inhibitory effect on prostaglandin E_2 (PGE_2) production and macrophage infiltration. Large oral doses of celecoxib are associated with cardio-toxicity, which potentiates the use of alternate delivery routes.[41-46] Therefore, NP theranostics could reduce celecoxib-associated toxicity and facilitate drug delivery to macrophages for COX-2 inhibition, as well as monitor response by imaging macrophages and evaluating the dynamics of infiltration as a function of time and therapeutic delivery.

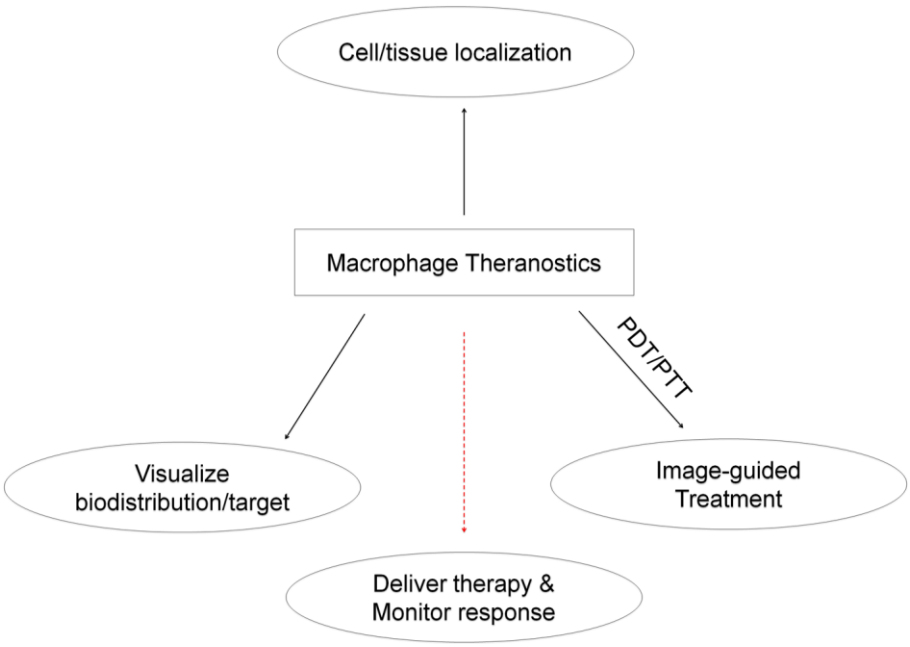

Figure 1.3. Current and future use of imaging functionality of macrophage theranostics.

Black arrows show the current areas where the imaging aspect of theranostics is used as reported in the literature. Red dotted line shows the possible future use.

As discussed previously, utilization of the imaging feature of macrophage theranostics was limited to *in vitro* characterization, *in vivo* biodistribution, and *ex vivo* histological analysis (Figure 1.3). We believe that simultaneous investigation of imaging and therapeutic aspects of disease treatment to monitor therapy will make the combinatorial approach more efficient for personalized medicine. To date, simultaneous therapeutic delivery and response monitoring using a single theranostic entity were not reported. We proposed that this could be achieved by exploiting the physiological and pathophysiological aspects i.e. phagocytic potential of macrophages, involvement in disease pathogenesis[47], migration to inflamed sites, and accumulation changes in response to the treatment.[29]

In summary, this dissertation addresses the current challenge of theranostics and demonstrates response monitoring by exploiting the therapeutic and diagnostic roles of macrophages. By design, this approach is generally applicable to different inflammatory diseases, where macrophages play pathological role and possess diagnostic significance. The work presented in this dissertation is believed to advance the field and fuel additional research by increasing the utilization of imaging and therapeutic functionalities.

1.2 Rationale, study hypothesis and aims

A careful investigation of current literature (chapters 1 and 2) and our own data (chapters 4, 5, and 6) shows the following crucial findings relevant to macrophage-targeted theranostics. 1) Macrophages are a key cell type involved in the pathogenesis of inflammatory diseases. 2) Macrophages and COX-2 are abundantly present in inflammatory diseases making them feasible targets for therapy and diagnosis. 3) Inhibition of myeloid COX-2 has shown efficacy in inflammation models. 4) Inhibition of COX-2 using celecoxib has shown to reduce inflammation by inhibiting PGE_2 and leukocyte recruitment. 5) Long term oral use of celecoxib is associated with cardiovascular and renal toxicity. 6) Macrophages can readily internalize NPs and migrate to the sites of inflammation. 7) Dual mode perfluorocarbon (PFC) nanoemulsions can provide unambiguous detection of macrophage infiltration in inflammatory diseases using fluorescence and ^{19}F magnetic resonance imaging (^{19}F MRI) and can facilitate *in vitro/ex vivo* characterization using fluorescent methods.

The combination of these findings prompted us to target macrophage COX-2 with a fluorescent PFC nanoemulsion incorporating celecoxib for simultaneous therapeutic and diagnostic effects. Newer reports are emerging where NPs were utilized

to inhibit or silence COX-2 in macrophages to treat underlying pathology. Chitosan/siRNA (small interfering ribonucleic acid) NPs were used to silence macrophage COX-2 in kidney injury.[48] Celecoxib NPs were investigated to target macrophage COX-2 in a breast cancer animal model as a possible chemotherapeutic and chemopreventive strategy.[49] Although theranostic aspects are not investigated, these studies are encouraging and further support our lead hypothesis identifying macrophage COX-2 as a generalizable anti-inflammatory intervention target.

By exploiting the natural phagocytic ability and disease-migration aspects of macrophages, we aimed to detect the inflammatory loci, deliver celecoxib to macrophages, and monitor temporal changes in infiltration in response to therapeutic delivery using fluorescent PFC nanoemulsions. This dissertation is based on the central hypothesis that ***celecoxib-loaded fluorescent PFC nanoemulsions produce anti-inflammatory effects while facilitating simultaneous imaging by optical fluorescence and ^{19}F magnetic resonance of activated macrophages in an adjuvant-induced murine inflammation model***. The following aims were proposed.

Aim 1: Preparation, characterization and optimization of PFC nanoemulsions encapsulating celecoxib and near-infrared fluorescent (NIRF) dye and demonstration of acceptable stability and toxicity profiles.

Aim 2: Characterization of PFC nanoemulsions in mouse macrophages for toxicity, uptake, and COX-2 inhibition.

Aim 3: *In vivo* assessment of celecoxib-loaded theranostic nanoemulsion for anti-inflammatory effect and imaging efficacy in an adjuvant-induced mouse inflammation model.

Through these study aims, PFC nanoemulsions were developed for macrophage imaging and assessment of infiltration changes. Efforts made to prepare a stable non-toxic nanoemulsion with optimized imaging potential are summarized in chapters 3, 4, 5, and 6. Chapter 3 deals with the synthesis and characterization of PFC-lipid conjugates, formulation development, characterization for colloidal attributes, toxicity and uptake evaluation in model mouse macrophages of a candidate conjugate (C8-PFTE). Due to slight toxic effect on cell viability and further development anticipated to be cost-ineffective, the focus shifted to a commercially available and clinically utilized PFC, perfluoropoly (ethylene glycol) ether (PFPE). The development and *in vitro* assessment as well as problems encountered with ^{19}F MR imaging aspects of PFPE nanoemulsion are described in chapters 4 and 5. Ultimately, the development of an improved formulation with higher PFPE content with desired stability and *in vitro* efficacy is demonstrated in chapter 6.

Chapter 7 describes the *in vivo* assessment of theranostic systems in adjuvant induced mouse paw edema and rat neuronal injury inflammatory models. In this chapter, combination of *in vivo* live animal imaging and *ex vivo* tissue analysis showed the specific accumulation of nanoemulsion in macrophages at the inflamed site. Furthermore, simultaneous therapy and monitoring changes in macrophage infiltration is demonstrated. Pain sensitivity reduction in the neuronal injury model further validated the approach of inhibiting COX-2 in macrophages for therapy and diagnostic imaging.

This dissertation demonstrates that targeting macrophage COX-2 has the potential to be a general approach applicable to inflammatory diseases, that provides

individualized treatment options based on the patient's response to the treatment, namely the extent of macrophage infiltration and associated temporal changes.

1.3 Role of macrophages in therapy and diagnosis of inflammation

Inflammation can be broadly defined as a host's response to infection, injury or metabolic imbalance, which acts to restore homeostasis.[4] It represents a highly complex network of cellular and sub-cellular components, which work in a regulated fashion to defend the host against deleterious stimuli.[3] In a typical inflammation setting, local endothelial and immune cells release inflammatory mediators, which increase blood flow and vascular permeability at the site. Leukocytes such as neutrophils and macrophages migrate to the site of injury based on released chemotactic factors (cytokines and chemokines) by a process known as diapedesis.[50] The inflammatory endothelium and local immune cells also upregulate cell adhesion molecules (CAMs) such as selectins, integrins, and cadherins, which further aid in the adhesion and transmigration of leukocytes.[50,51] Neutrophils are recruited first to the site of injury and they act to remove the injurious stimuli by phagocytosis and the release of inflammatory mediators. Neutrophils are present in the first few hours to days, while macrophages are recruited by further downstream signals to aid in resolution and repair.[51] Macrophages populate the inflammation sites to neutralize the injurious stimuli by modulation of adaptive immunity, tissue remodeling, and removal of pathogens, cell debris, and senescent cells.[52] This cascade is known as acute inflammation, which is self-limiting and results in the restoration of homeostasis (Figure 1.4). Failure to cease the injurious stimuli leads to persistent (chronic) inflammation resulting in tissue damage (Figure 1.4).

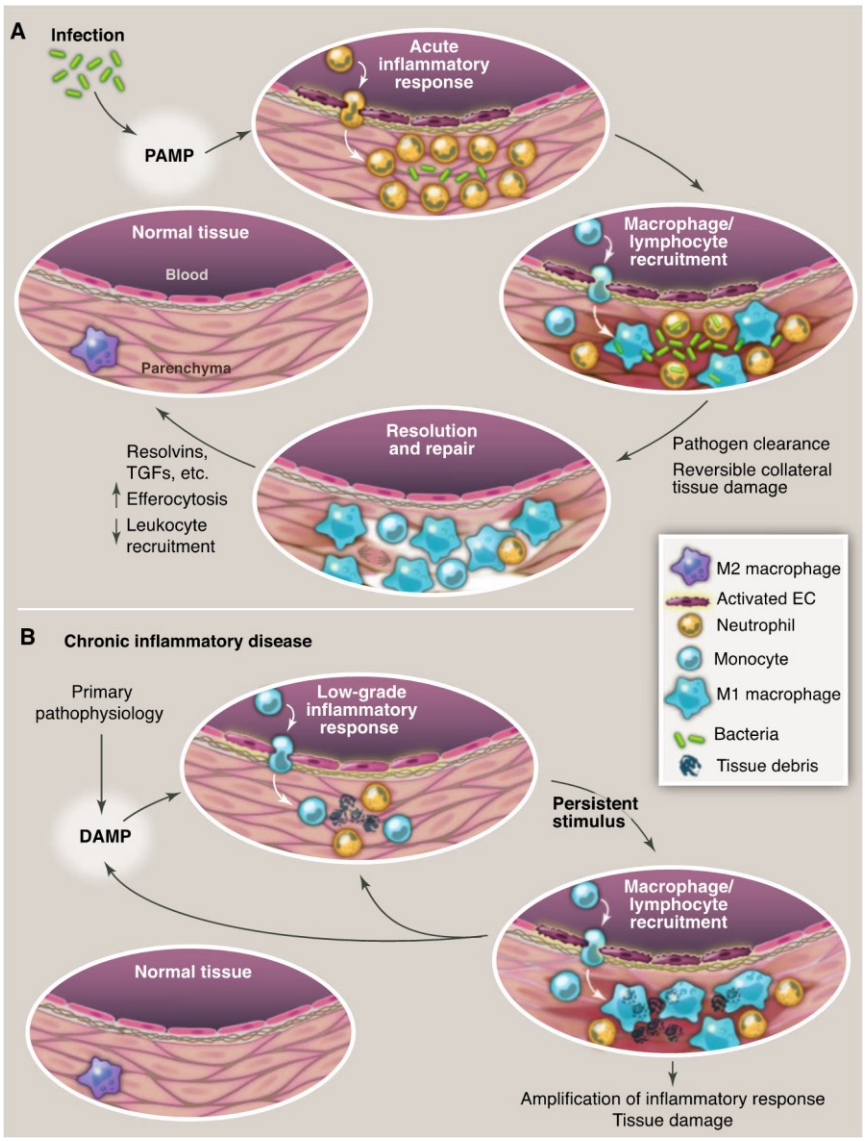

Figure 1.4. Schematic showing acute and chronic inflammatory events

A. Features of acute inflammation are summarized as presentation of pathogen-associated molecular patterns (PAMPs) to the recognition receptors, which illicit inflammatory response with macrophage recruitment and removal of pathogen. Reversible damage created during this process is resolved leading to restoration of homeostasis. **B.** Presentation of damage-associated molecular patterns (DAMPs) leads to initial response through cytokines and chemokines produced by immune cells, which cannot eradicate the stimulus. Persistent stimulus leads to amplification of signal by positively influencing the production of DAMPs leading to tissue damage and chronic inflammation. From: Tabas I, Glass CK 2013. Anti-inflammatory therapy in chronic disease: challenges and opportunities. Science 339(6116):166-172.[1] Reproduced with permission from AAAS.

Macrophages are a type of leukocyte belonging to the mononuclear phagocytic system, derived from progenitor cells of hematopoietic origin in bone marrow.[53] They are replenished on a regular basis from circulating blood monocytes.[53] Macrophages are constitutively present in all tissues, where they participate in tissue survival, regulation and modeling processes.[52] Their primary function is to clear apoptotic cells and cellular debris generated during tissue remodeling and necrosis. In addition to these homeostatic roles, macrophages are essential immune cells that participate in both innate and adaptive immunity.[47] During the chronic phase, macrophages are continuously recruited and release inflammatory mediators such as chemokines, cytokines, lipid mediators, proteases and reactive oxygen species (ROS).[47] These mediators cause detrimental effects to the host leading to initiation, exacerbation and progression of several infectious and non-infectious diseases.

1.3.1 Macrophages in inflammatory diseases – potential for therapy

There is increasing evidence that macrophages significantly contribute to the pathogenesis of many common chronic diseases. This section is primarily focused on pathologies involving non-infectious chronic inflammatory conditions. One example of these is RA, in which macrophages play a prominent role through their production of inflammatory mediators such as TNF-α, which can cause considerable inflammation and joint destruction.[54] Another example is Type 2 diabetes, in which accumulation of macrophages is associated with several complications such as neuropathy, nephropathy and atherosclerosis.[55] A third example is atherosclerosis, in which macrophages uptake low density lipoprotein and transform into lipid-laden cells called foam cells that contribute to the initiation and progression of atherosclerotic lesions.[56] Additionally,

proteases produced by macrophages degrade the extracellular matrix (ECM), which leads to plaque rupture and myocardial infarction (MI). In cancer, tumor-associated macrophages (TAMs) are involved in several tumorigenic activities leading to angiogenesis and metástasis.[57] Similarly, macrophages are involved in several stages of pathogenesis in neurological, autoimmune, cardiovascular and pulmonary diseases.[54,58,59]

In addition to the discussed pathogenic roles, macrophages also display protective functions in chronic inflammatory diseases. Depending on the pathological environment, they adapt to different phenotypes, which, either intensify or resolve the disease.[52] They are broadly classified as classically activated (M1) pro-inflammatory and alternatively activated anti-inflammatory (M2) phenotypes mirroring Th1 and Th2 states of T cells.[60] Due to the vast biochemical and physiological differences within M1 and M2, it was suggested that macrophages form part of a continuum and possess overlapping functions of different macrophage subsets. For the purpose of this discussion, only the two extreme states of macrophages, M1 and M2 are considered. The diverse roles of macrophages are attributed to these phenotypes. For example, TAMs exhibit M1 and M2 phenotypes depending on the local cytokine milieu. M2 macrophages are involved in the release of growth factors, angiogenesis and degradation of the ECM leading to metastasis, while M1 macrophages exhibit tumoricidal activity.[61] In atherosclerosis, macrophages participate in the initiation, progression and rupturing of atheroma.[62] In contrast, a subset of macrophages (M2) is involved in the resolution of the disease and tissue remodeling.[63] Likewise, macrophages play a diverse role in autoimmune,[54] pulmonary,[58] and neurological diseases.[59] Therefore, macrophages represent promising targets for the

treatment of inflammatory diseases. Section 1.5 reviews some of the targets expressed by macrophages that can be intercepted by anti-inflammatory therapies.

1.3.2 Imaging macrophages and disease diagnosis

Imaging tools are indispensible in advancing our understanding of diseases for improved drug design and also for disease detection, diagnosis and assessment of treatment effects. Prime reasons to utilize macrophages for disease diagnosis include: (1) their abundance in the inflammatory milieu (2) their migration to the diseased locales and (3) the correlation observed between macrophage number and disease severity. A recent review by Weissleder *et al.*[64] detailed the aspects of nanomaterials and imaging modalities for macrophage detection in inflammatory diseases in both preclinical and clinical settings. Magnetic resonance imaging (MRI) contrast agents, namely iron oxide nanoparticles (IONPs) and ultrasmall paramagnetic iron oxide (USPIO) NPs that are internalized by macrophages and infiltrate the inflamed site have been used clinically for non-invasive detection of atherosclerosis[65], MI[66], and type 1 diabetes.[67] Trivedi *et al.*[65] applied USPIO NPs (Sinerem®, Guerbet, now withdrawn) to detect atherosclerotic plaques using MRI, which could be a viable diagnostic method to identify patients with high-risk for plaque rupture. A macrophage-targeted PET tracer was investigated for its ability to detect early synovitis in arthritic patients.[68] The study identified that the accumulation of PET tracer is proportional to disease severity. Also, detection of PET tracer in the contralateral knee of the arthritic patients provided possibility of using this mode of macrophage imaging to detect subclinical synovitis. The effect of atorvastatin therapy was monitored by imaging macrophages using USPIO-enhanced MRI in the well-known ATHERMO (Atorvastatin Therapy: Effects on Reduction of Macrophage

Activity) study.[69] Significant changes in signal intensity compared to baseline were observed with treatment in the carotid plaque, indicating changes in macrophage accumulation. These studies strongly support the use of macrophages as biomarkers for disease detection, disease severity assessment, and treatment effectiveness. Imaging macrophages has the potential to be a generalized method for disease diagnosis and prognosis, thus driving the personalized medicine in inflammatory diseases.

1.4 Nanosystem design considerations for effective macrophage targeting

NPs have been utilized to deliver imaging and therapeutic agents to macrophages with or without targeting ligands,[70] because they are readily internalized by macrophages' natural phagocytic ability ("big eaters"). Although macrophages can readily internalize NPs, several attributes, namely size, shape, surface charge, concentration, targeting ligands, and surface functionalization with PEG influence the *in vivo* targeting efficiency and performance. One of the major limitations of current nanomedicine formulations is their non-specific uptake by macrophages of reticuloendothelial system (RES), which reduce both blood circulation time and target site accumulation. However, this aspect can be exploited for macrophage-targeted therapies.

Macrophages exhibit size-, concentration- and time-dependent uptake of NPs. Cell surface is negative and hence it has been proposed that positively charged NPs can bind to the cell surface and be internalized.[71] However, many reports suggest that this effect is true for non-phagocytic cells. It should be noted that positively charged NPs induce cytotoxicity, thus reducing biocompatibility. Contrary to the uptake behavior of non-phagocytic cells, phagocytic cells show preferential uptake of anionic NPs.[72] For liposomal formulation, highly charged anionic and cationic formulations show greater

uptake compared to the neutral ones.[32,73] Negatively charged liposomes display greater biocompatibility. One report claims that NP size is a stronger determinant of macrophage uptake than charge,[74] with 100 nm particles showing greater uptake than 40 nm. It is likely that larger particles can bind to multiple receptors triggering internalization through clustered receptors.

NPs in circulation possess different properties due to electrostatic interactions with serum components, protein adsorption and opsonization, which can mask their native surface functional groups and charge, giving them a different set of properties for uptake. The recognition of NPs for uptake is mediated by opsonin coating (e.g. IgG) in the blood stream and subsequent interaction with cell surface receptors (Fc) for uptake. The extent of coating and recognition depends on size, surface charge, and the presence of functional groups. Finally, surface presence of PEG is essential for NP stability in the aqueous medium and for increase in blood circulation time. However, PEG can reduce the opsonization process and hence the uptake potential.[75] Therefore, a critical balance needs to be established to obtain NPs displaying high stability and uptake in macrophages.

In addition to these passive targeting approaches, targeting ligands can be used to increase uptake. Macrophages express several receptors that have been targeted with ligands such as dextran, folic acid, mannose, hyaluronate, and tuftsin, antibodies against F4/80 and cluster of differentiation (CD) 169.[26,73,76,77] The disrupted vasculature in the inflammatory environment provides an additional opportunity to passively target nanosystems.[25,26,78] Monocytes and macrophages have an intrinsic disease-homing property, which can be utilized for delivering NPs to inflamed sites.[25,26] Through these

properties, macrophages have been used as Trojan horses to deliver drugs and imaging agents to the disease site.[26]

While a universal criterion for NP design is not feasible to propose based on the literature, some features can be considered for effective macrophage uptake. The size of the nanosystem is a critical factor identified in many studies, with >100 nm showing significant uptake. Charge effect on differential uptake of NPs is documented; it is conceivable to use neutral or anionic NPs to avoid biocompatibility problems generally associated with cationic NPs. The concentration of surface PEG should balance stability and uptake. Finally, targeting ligands can be utilized to increase cell uptake, but synthesis of these conjugates, cost, and large-scale production entail careful evaluation. Unlike cancer or endothelial cells, the use of targeting ligands has lesser effect on uptake in macrophages because macrophages possess intrinsic phagocytic ability. Active targeting strategies could be highly useful to preferentially target a specific macrophage phenotype.

1.5 Theranostics for macrophage detection and therapy – state of the art

Anti-inflammatory therapies targeting macrophages by specific ablation, inhibition of their infiltration and reduction of pro-inflammatory mediator release have been applied in RA, atherosclerosis, vascular injury and cancer. However, variable efficacy results across the patient population were observed.[14,15,79,80] In some instances, significant depletion of macrophages has been associated with immunosuppression, infection[81] and reduced wound healing.[82] This combination of therapeutic and harmful effects can be attributed to the different activated states of macrophages in disease environments. To delineate the protective and detrimental effects of targeting macrophages, there is a need to bring therapy and diagnosis together. In this regard,

theranostics could provide essential information about the delivery of drug carriers to macrophages as well as their biodistribution, treatment efficacy and toxicity profile in real-time, leading to better therapeutic intervention. Table 1.1 shows a summary of the theranostics reported in the literature, different targets, targeting ligands utilized and comments showing the highlights of the study. A schematic of multifunctional theranostics for macrophages is shown in Figure 1.5.

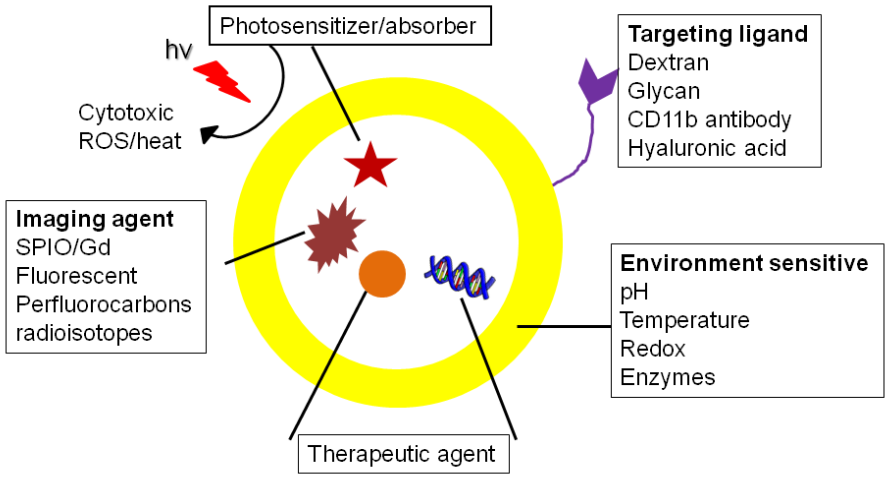

Figure 1.5. Schematic showing the multifunctional theranostic systems utilized for imaging and therapy of macrophages. Originally published elsewhere.[2]

1.5.1 Theranostics for macrophage ablation

Photo and chemotherapy based approaches are utilized to reduce macrophage numbers at the diseased site. Reduction in these cells deprives the pathological environment of macrophage-mediated pro-inflammatory mechanisms, and thus reduces inflammation. Selective macrophage ablation was the major strategy used in experimental studies to investigate their role in pathogenesis of several diseases.

Macrophage depletion has been applied in the treatment of atherosclerosis,[83] restenosis,[84] RA,[85] and cancer[86] in preclinical and clinical subjects.

Photodynamic therapy (PDT) and Photothermal therapy (PTT) are treatment modalities that use a combination of light and a photoactive agent to induce cell death. PDT uses photosensitizers that produce cytotoxic oxygen species upon illumination.[87] PTT utilizes photoabsorbers such as organic dyes to generate localized hyperthermia upon illumination by visible to near-infrared (NIR) light.[88] Hyperthermia can induce cell death by protein denaturation and disruption of the cytoskeleton. In PDT and PTT, NIR-active (650-900 nm) material is preferred to enable treatment of deep tissues (up to a few centimeters) and also to reduce tissue scattering effects, which allows for reliable imaging. Since photosensitizer/photoabsorber accumulation and photo-irradiation are required for cell death, these are selective techniques. PDT and PTT agents can be referred to as theranostics due to their inherent fluorescence/absorbance and their ability to induce cell death. Of note, light based therapies are already applied clinically to treat cancer, skin conditions and other surface accessible pathologies.[87]

Several NPs incorporating photosensitizers for disease imaging and macrophage ablation have been reported as shown in Table 1.1. Some of these theranostics were designed to increase macrophage uptake through targeting ligands such as hyaluronic acid and dextran. Theranostics have been investigated to detect and deplete macrophages in arthritic joints[89] and atherosclerotic plaques.[90,91] Imaging the theranostic facilitated the detection of arthritic joints, the assessment of residence time and the directing of light.[89] To confer additional selectivity, a stimuli-responsive theranostic was also reported, which utilized protease activation to selectively deplete cathepsin-B (Cat B) producing

macrophages.[92] Cathepsin is a protease enzyme involved in matrix degradation, which can cause plaque rupture.

For PTT, several nanomaterials such as gold nanorods (GNRs), nanoshells and carbon nanotubes have been studied as NIR absorbing materials.[93-95] These materials have optical properties that can be used for *in vitro* and *in vivo* imaging. As outlined in Table 1.1, targeted and non-targeted NPs have been investigated for photothermal ablation of macrophages. For example, dextranated IONPs with surface gold coating were used for thermal ablation of atherosclerotic macrophages.[95] GNRs coated with dextran or a macrophage targeting monoclonal antibody (CD11b) were tested *in vitro* for their cytotoxic potential.[94,96]

Limited light penetration makes photo-based therapies impractical for inflammatory conditions in deeper tissues where surgical or invasive endoscopic intervention is required, as performed in some of the studies in Table 1.1. In these conditions, target-specific accumulation of cytotoxic chemotherapeutic drugs could be an alternative. Several cytotoxic drugs such as clodronate, glucocorticoids, doxorubicin and methotrexate are utilized for this purpose.[97-99] Systemic release of a cytotoxic drug can reduce the global macrophage population, thereby affecting homeostasis and making the host prone to infections. In this regard, theranostics could be employed to target cytotoxic drugs to inflamed tissue through EPR, while the imaging functionality could help visualize biodistribution. For example, the effect of prednisolone phosphate encapsulated in MRI-fluorescence active liposomes was studied on TAMs.[98] Fluorescence was used for histological analysis and microscopy, while contrast enhanced MRI with gadolinium (Gd) liposomes was used to evaluate drug delivery to the tumor site and intra-tumoral

theranostic distribution in a mouse melanoma model. Imaging has assisted in the quantification of theranostic reaching the tumor site, which was found to be 5% in TAMs. However, a 90% reduction in systemic leukocyte count was observed. This reduction, as opposed to TAM depletion, could be the reason for therapeutic efficacy. While systemic reduction could reduce the tumor-infiltrating monocytes, a high drop in their count could make the host susceptible to infections. This study highlighted the importance of imaging functionality in the theranostic, which facilitated in the interpretation of mechanism of anticancer effect caused by these liposomes.

Macrophage ablation therapies are inherently aggressive; therefore, selectivity is very crucial to reduce immunosuppression and infections. Although light-mediated theranostics are selective, they have been shown to cause significant tissue damage and induce inflammatory reactions, which could lead to recurrence of the disease.[100] Additional challenges included focused irradiation of target tissues, release of cellular products post cell death, toxicity due to long term accumulation of photosensitizers/photoabsorbers, light penetration depth in clinical subjects and dissipation of heat by blood flow. It is important to note that in certain diseases, a subset of macrophages show beneficial effects (e.g. M2 macrophages in atherosclerosis), and their depletion could hamper wound healing. Chemotherapeutic ablation of macrophages is useful in the treatment of deep-tissue pathologies that are inaccessible by PDT and PTT. Conferring the theranostic with tissue selectivity by targeting ligands, stimuli sensitivity, or external activation is vital in order to confine the activity to the target tissue. Although these aggressive approaches are valuable in life-threatening diseases such as cancer and less invasive alternatives need to be explored.

1.5.2 Theranostics utilizing non-ablation approaches

Reducing the pathogenic activity of macrophages could be promising since this approach would avoid detrimental effects caused by macrophage ablation and the released toxic products. Macrophages produce a plethora of pro-inflammatory mediators that damage the host tissue and these can be targeted by theranostics.

Harel-Adar *et al.*[101] reported the utility of phosphatidylserine-presenting iron oxide loaded liposomes to modulate macrophage phenotype in MI. PS is expressed on apoptotic cells, which are recognized by macrophages and cleared. Apoptotic cells inhibit the production of pro-inflammatory cytokines from macrophages concomitant with the secretion of anti-inflammatory cytokines. The presence of iron oxide enabled visualization of theranostic accumulation at the infarct site after femoral vein injection in a rat model of acute MI. Following uptake of PS-liposomes by macrophages, an increase in anti-inflammatory markers and a reduction in pro-inflammatory markers were observed both *in vitro* and *in vivo* showing the shift of macrophage phenotypes from M1 to M2. *In vivo*, theranostic-treated rats showed effective wound healing. Such theranostics could also be effective in other diseases. For example, celecoxib theranostic could be applied in cancer because celecoxib has shown to change the TAM phenotype from pro-tumor (M2) to tumoricidal M1-like.[102] Specific receptors are expressed by macrophages displaying different phenotype, which could be used for selective targeting.[103,104]

Table 1.1. Table summarizing macrophage-targeted theranostics reported in the literature

Target	Theranostic	Ligand	Disease model	Comments
Synovial macrophages [89a]	Nanogels incorporating photosensitizer	Hyaluronic acid	Arthritic mouse	Imaging to visualize joint retention time, invasive local injection
Plaque macrophages [90,91a]	Cross-linked IONPs incorporating photosensitizer	Dextran	Atherosclerotic mouse	Imaging to visualize plaque macrophages and guide therapy, PDT after surgical exposure of carotid artery
Cat B-producing macrophages [92a]	Protease activated photodynamic agent	None	Atherosclerotic mouse	Imaging to visualize uptake and therapy response, selective for CatB-producing macrophages, multiple i.v. administration
Plaque macrophages [95a]	Surface gold coated IONPs	Dextran	Atherosclerotic rabbit model	Imaging to visualize uptake in macrophages in histological samples
Macrophages *in vitro* [96a]	GNRs	CD11b antibody	-	Similar cell death between naked and targeted GNRs
Macrophages *in vitro* [94a]	GNRs	Dextran	-	Increased cell death with targeted compared to naked GNRs
Plaque macrophages [93a]	Single walled carbon nanotubes	-	Atherosclerosis mouse	Imaging to visualize accumulation in ligated carotid arteries, *ex vivo* PTT
TAMs [98a]	Prednisolone phosphate encapsulating Gd-fluorescent liposomes	-	Melanoma mouse	Dual mode imaging, fluorescence for histology and MRI to assess intratumoral distribution and therapy effect (measuring tumor size by MRI)
In vitro macrophages [99b]	Coumarin-6 incorporating SPIO-PLGA NPs with cytotoxic methotrexate and clodronate	F4/F80 antibody	-	Fluorescence imaging to assess macrophage uptake *in vitro*
Infarct macrophages [101b]	Phosphatidyl serine-liposomes	-	Acute MI rat model	MRI used to visualize infarct accumulation of liposomes, *in vivo* studies showed phenotype change (M1 to M2)

MCP-1/CCR2 inflammatory monocytes/macrophages [105b]	Fluorescently-tagged siRNA-loaded theranostic lipid NP	-	MI, atherosclerosis, diabetes and cancer	Fluorescence imaging for biodistribution, target site accumulation and histology
TNF-α [106b]	Fluorescently-tagged microparticles incorporating Map4k4 siRNA	1,3-β-glucan	LPS-injected mouse	Fluorescence imaging to assess tissue and cellular uptake, oral delivery to reduce systemic TNF-α, high dosing frequency
TNF-α [107b]	Fluorescent Supramolecular self-assembled NPs	Mannose, chitosan, cysteamin, polypeptide	LPS-induced mouse hepatic injury	Multivalent targeting, fluorescence imaging for biodistribution, single oral dose lead to 80% reduction in systemic TNF-α
TNF-α from synovial macrophages [108b]	Anti-TNF-α siRNA-loaded fluorescent liposomes (wraposomes)	-	Arthritis mouse model	Fluorescence imaging for biodistribution, accumulation in 70% of synovial macrophages
Hydrogen peroxide [109b]	Chemiluminescent antiox-idant Pluronic® F127 micelles incorporating hydroxyl benzyl alcohol (HBA) and a fluorescent dye	-	LPS-induced inflammation (s.c.) mouse model	Fluorescent imaging was stimuli-sensitive (hydrogen peroxide)
Myeloid-related protein-8/14 [110b]	anti-Mrp antibody coupled with Gd NP	PS and ω-carboxynon anoyl-cholesteryl ester	Atherosclerotic mouse model	Plaque distribution by MRI

[a] Macrophage ablation; [b]Non-ablation approach

PLGA - poly(lactic-co-glycolic acid); i.v. - intravenous; LPS – lipopolysaccharide; MCP-1 - monocyte chemoattractant protein-1

Pro-inflammatory mediators produced by macrophages have been targeted for simultaneous therapeutic delivery and imaging. Monocyte chemoattractant protein-1 (MCP-1) is a chemokine upregulated in inflammatory monocytes/macrophages, which is involved in their movement to the disease site. Leuschner *et al.* developed a fluorescently-tagged siRNA (small interfering RNA)-loaded theranostic lipid NP for CCR2 silencing activity in inflammatory monocytes.[105] A detailed study outlining the utility of this delivery vehicle in MI, atherosclerosis, diabetes and cancer showed compelling results. Fluorescence imaging was used to visualize NP/siRNA biodistribution, which were predominantly present in splenic, bone marrow and blood inflammatory monocytes. In addition to MCP-1, CAMs can also be targeted to reduce macrophage infiltration.

Dysregulated production of TNF-α, a potent pro-inflammatory cytokine produced by M1 macrophages, has been implicated in cancer, RA, IBD, and Alzheimer's disease (AD).[111,112] Theranostics facilitated the targeted delivery of TNF-α inhibitors, such as siRNA, to inflammatory macrophages and increased their oral absorption.[106,107] These theranostics were surface functionalized with multivalent targeting capabilities (Table 1.1) for increased uptake. Komano *et al.* reported the use of anti-TNF-α siRNA-loaded liposomes called wraposomes that targeted synovial macrophages in a mouse model of arthritis.[108] Despite the absence of a targeting moiety, 70% of synovial macrophages were shown to uptake the theranostic. In these studies, imaging was utilized to confirm uptake in macrophages and to assess biodistribution.

Excessive production of ROS can cause oxidative stress in diseases. Activated macrophages and neutrophils are the major source of ROS in the inflammatory

environment. Cho *et al.* showed *in vitro* and *in vivo* the anti-inflammatory activity of stimuli-responsive chemiluminescent antioxidant micelles that incorporated the antioxidant, hydroxyl benzyl alcohol and a fluorescent dye.[109] The presence of ROS (H_2O_2) resulted in a POCL (peroxylate chemiluminescence) reaction that lead to the transfer of energy to the nearby dye, causing the dye to fluoresce. The stimuli-sensitive fluorescence of this theranostic was verified in an inflammation model. It could enable detection of the ROS-active inflamed site as well as assessment of therapeutic effect because reduction in ROS will lead to reduced fluorescence.

Mrp-8/14 is a member of the S100-family of Ca^{2+}-modulated proteins. It participates in vascular inflammation, macrophage recruitment, and pro-inflammatory cytokine release. Mrp-8/14 is detected in the cytoplasm of neutrophils and macrophages. Maiseyeu *et al.* targeted Mrp-8/14 in a mouse atherosclerotic model using a multivalent theranostic containing PS, ω-carboxynonanoyl-cholesteryl ester and an anti-Mrp antibody coupled with Gd-NP (aMrp-NP).[110] The ω-carboxynonanoyl-cholesteryl ester (expressed on foam cells) and PS were utilized for uptake by macrophages, whereas the anti-Mrp antibody was used as an anchor for retention in atherosclerotic plaques. *In vitro* studies in BMDMs of the atherosclerotic mouse showed neutralization of Mrp 8/14 pro-inflammatory effects with aMrp-NP, potentially caused by antigen-antibody interactions. *In vivo* MRI studies in the murine atherosclerotic model confirmed the presence of aMrp-NP around the plaque.

In addition to the above-discussed targets, macrophages express many enzymatic, protein and lipid based targets for therapeutic intervention. Compared to aggressive macrophage depletion, these approaches are non-destructive and the likelihood of benign

tissue damage is minimal, since no cytotoxic products are released. These studies demonstrate the feasibility of targeting macrophages for simultaneous imaging and therapy using a variety of theranostic systems.

1.5.3 Conclusions, Limitations and Future Perspective

As detailed in this chapter, macrophage-targeted theranostics have shown promising results in preclinical models for simultaneous imaging and therapy. A number of molecular targets in macrophages that are indicated in several diseases were investigated. Based on these studies, it can be concluded that the theranostics targeting of macrophages holds great promise for diagnosis and treatment of the inflammatory diseases, which could lead to effective disease management.

However, limitations in current technology pertaining to the choice of imaging and therapeutic functionalities, and the utility of imaging aspect still need to be addressed. For example, the majority of the presented theranostics utilized optical imaging, which is limited by light penetration. Optical imaging can be reserved for surface pathologies, histological analysis and preclinical evaluation. To obtain unlimited tissue penetration in clinical subjects, theranostics that incorporate paramagnetic MRI contrast agents can be used, but the inherent tissue background limits unambiguous detection of macrophages. An alternative method is ^{19}F MRI, which detects fluorine (^{19}F) from externally introduced PFCs. This imaging technique holds great potential due to near-zero background leading to quantitative detection. ^{19}F MRI aspects are discussed in chapter 2, section 2.4.3.

Current anti-inflammatory therapies are majorly concentrated in targeting inflammatory mediators such as TNF-α, prostaglandins (COX-2) and inhibition of

macrophage migration. In this regard, biologics such as siRNA and monoclonal antibodies have shown potent anti-inflammatory properties; however, these biologics are usually associated with severe toxicities. While theranostics could limit these toxicities by site-specific targeting, challenges associated with large-scale production of biologics[113] could add to the existing limitations of theranostics for clinical translation. Alternately, small molecule anti-inflammatory drugs with well-characterized efficacy, toxicity and safety profiles could be applied for theranostic research. Amongst these drugs, NSAIDs have shown efficacy across inflammatory disease models. NSAIDs are one of the commonly used anti-inflammatory drugs targeted against COX enzymes. The role of COX-2 in inflammatory diseases is discussed in chapter 2.

Finally, as discussed earlier, therapy and imaging the response to the therapy have been investigated separately. A simultaneous approach to monitor the therapy could be very useful in the identification of the subgroup of patients that respond effectively to the treatment (i.e. to the theranostic under investigation). To achieve this goal, our efforts focused on the development of a macrophage COX-2 inhibiting theranostic. Chapter 2 details background information and the synthesis of rationale for the developed theranostic.

Parts of chapter 1 were originally published in the review by Patel and Janjic.[2]

2 Rationale for Perfluorocarbon nanoemulsions as a platform to deliver celecoxib for COX-2 inhibition in macrophages

2.1 COX-2 in inflammatory diseases

Cyclooxygenase (COX) enzymes, COX-1 and COX-2 are involved in several homeostatic functions. COX enzymes catalyze the conversion of arachidonic acid (AA) into biologically active lipids called prostaglandins (PGs), namely PGG_2 followed by PGH_2.[114] AA is released from the plasma membranes in the presence of phospholipase A_2 (Figure 2.1). PGH_2 serves as a substrate for the formation of further downstream products such as PGI_2, PGD_2, PGE_2, $PGF_{2\alpha}$, and thromboxane A_2 (TXA_2), in the presence of respective synthases. COX-1 is constitutively present and involved in 'housekeeping' functions such as the maintenance of gastric mucosa and renal blood flow.[115] COX-2 is induced in response to injury or inflammatory stimuli.[114,115] The increased production of PGs is responsible for pain, increased vascular permeability, edema and immune cell infiltration observed during inflammation.[116] Immune cell infiltration has been associated with the effect of PGE_2 on the upregulation of CAMs[117] and MCP-1, which are involved in leukocyte recruitment. MCP-1, for instance, is induced by activated PGE_2/EP4 signaling.[118]

COX-2 plays an important role in the pathogenesis of inflammatory diseases, where it is over-expressed. In fact, the development of COX-2 specific PET and fluorescence imaging agents for cancer and inflammation detection signify the ubiquitous presence of COX-2 in inflammatory diseases.[119,120] For example, in osteoarthritis and RA, the synovial cavity is infiltrated with cells expressing COX-2, which is responsible

for pain. NSAIDs targeting COX-2 reduce pain and inflammation in arthritic patients. Evidence of reduced inflammatory cell infiltrate and inflammation in the synovium was also reported in a rat model of arthritis with selective COX-2 inhibition.[121] In cancer, COX-2 expression has been correlated with poor prognosis, increased angiogenesis and metastasis. COX-2 silencing has shown delayed tumor formation and reduced metastasis in preclinical models.[122] COX-2-mediated release of PGE_2 is involved in the suppression of cancer cell apoptosis, increase in proliferation and angiogenesis.[36] In support of these properties, long-term use of selective COX-2 inhibitors has shown beneficial anticancer effects in several clinical trials.[123,124] COX-2 is also widely implicated in cardiovascular diseases such as atherosclerosis,[125] where it is involved in macrophage recruitment and plaque rupture through MCP-1 and matrix metalloproteinases (MMPs). COX-2 expressing cells are present around the amyloid-plaques in AD,[126] and selective COX-2 inhibitors have shown protection against AD. COX-2 is also shown to be involved in the pathogenesis of Parkinson's disease, where it can contribute to neurodegeneration by oxidative stress.[127]

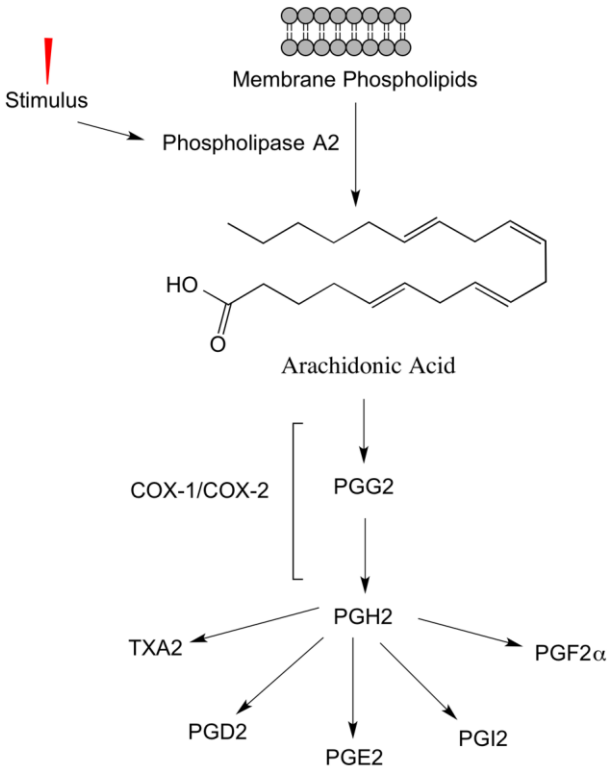

Figure 2.1. Formation of prostanoids from arachidonic acid.

Phospholipase A2 converts membrane phospholipids to AA in response to stimuli, which can be converted to different prostanoids under the action of COX-1/COX-2 and related synthases.

2.1.1 COX-2 in monocytes and macrophages as a therapeutic target

Based on the studies presented in section 1.3.1 and section 2.1, COX-2 and macrophages have been implicated separately and together in many inflammatory diseases. Activated macrophages/monocytes such as TAMs in cancer and foam cells in atherosclerosis are one of the key cells expressing COX-2 in the inflammatory milieu. Therefore, we proposed that inhibition of macrophage COX-2 could be an effective strategy to reduce inflammation.[128] Consistent with this hypothesis, recent reports indicate that targeting macrophage PGE_2 can be applied to reduce cancer and atherosclerosis. COX-2 is overexpressed in foam cells and its selective inhibition has

reduced early atherogenesis. PGE_2 produced by COX-2 expressing macrophages has been implicated in the release and activation of MMPs, which play an important role in plaque stability and macrophage infiltration in atherosclerosis.[125] A COX-dependent pathway was indicated for monocyte chemotaxis in atherosclerosis.[129] Consequently, selective COX-2 inhibition by celecoxib has exhibited reduction in MCP-1 and macrophage infiltration.[40] Chen *et al.*[130] recently reported that the deletion of myeloid cell mPGES-1, which catalyzes the synthesis of PGE_2, reduces atherogenesis in mice. Likewise, deletion of COX-2 in myeloid cells contributed to reduced mammary tumor growth through increased cytotoxic T-cell function.[131] In AD, COX-2 expressing macrophages were shown to infiltrate the brain and damage the blood brain barrier,[126] indicating a potential therapeutic effect by targeting these cells. Evidence from the literature supports that macrophage COX-2 inhibition could find widespread applicability in inflammatory diseases.

2.2 Pharmacology of COX-2 inhibitor, celecoxib

Celecoxib (Figure 2.2) is one of the widely used NSAID for selective COX-2 inhibition. Celecoxib exhibits anti-inflammatory, analgesic and antipyretic activities. The IC_{50} of celecoxib is 40 nM and it displays 375-fold higher selectivity for COX-2 over COX-1 based on human recombinant enzyme assays.[33] Unlike aspirin, celecoxib binds reversibly to the COX-2 enzyme pocket. The binding pocket of the COX-2 enzyme differs from COX-1 at one relevant position of 523. At this position, COX-2 has a valine while COX-1 has an isoleucine. This difference causes celecoxib bind strongly to COX-2 and weakly to COX-1.[34]

Celecoxib is a BCS (Biopharmaceutics classification system) class II drug with a high membrane permeability (Log P = 3.64) and a low aqueous solubility of 7 μg/mL.[132] It has low (22-40%) oral bioavailability in dogs[133] (to our knowledge absolute bioavailability in humans has not been reported). It is highly protein bound (90%) and it is also rapidly eliminated from the plasma ($t_{1/2}$ = 11.2 h).[33,46,134] It is metabolized primarily by cytochrome P450 enzyme, CYP2C9. Following hepatic metabolism, celecoxib is eliminated in urine and feces.[34] Celecoxib is prescribed to reduce pain and inflammation in arthritis, juvenile RA, ankylosing spondylitis, and menstrual pain. It is also prescribed to treat colon polyps. It is dosed perorally in tablets and capsules.

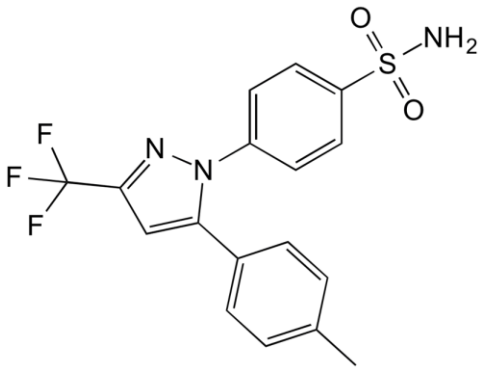

Celecoxib
Molar mass: 381.37 g/mol

Figure 2.2. The chemical structure of celecoxib.

The therapeutic effects of celecoxib span a wide spectrum of inflammatory diseases. Selective COX-2 inhibition with celecoxib has shown reduced atherosclerotic lesions in the mouse model, possibly by reducing inflammatory cell recruitment due to its inhibitory effect on the expression of CAMs.[35] Reduced MCP-1 and macrophage infiltration was also observed with celecoxib treatment in a rabbit model of

atherosclerosis.[40] It has been reported to suppress and delay tumor growth in preclinical models.[46,135] Epidemiological studies have provided evidence of reduced risk of colon, breast, lung and prostate cancers with regular use of celecoxib.[136] In cancer, it acts as a multifunctional drug that simultaneously induces COX-2 independent apoptosis, inhibits PGE_2 mediated anti-apoptotic proteins and inhibits angiogenesis.[36] Recently, celecoxib has also been shown to alter the phenotype of macrophages from protumor (M2) to antitumor (M1) subtype via COX-2 inhibition.[102] It has been shown to reduce vascular endothelial growth factor expression and vascular leakage, which are important contributors to the pathogenesis of diabetic retinopathy.[41] Celecoxib showed protection against dopamine neuron loss in a preclinical model of Parkinson's disease[39], indicating its applicability in neurodegenerative diseases.

2.3 Celecoxib toxicity and alternate formulations

Selective COX-2 inhibitors reduce the risk of gastrointestinal side effects, which are associated with non-specific COX inhibitors. However, long-term use of specific COX-2 inhibitors is associated with cardiovascular and renal toxicity, which led to the withdrawal of Rofecoxib and Valdecoxib in 2004 and 2005 respectively. Selective COX-2 inhibition reduces prostacyclin production by vascular endothelium, with no inhibitory effect on TXA_2 production. This selective reduction in protective prostacyclin predispose patients to vascular injury and cardiac events such as MI.[137] Celecoxib is generally well tolerated, but in clinical cancer studies, high oral doses (200 – 400 mg, twice daily) were administered for several months leading to cardiovascular side effects, which may be severe.[123] To overcome side effects and increase target site accumulation, which could reduce the required dose, alternate formulations of celecoxib have been investigated.

Microparticle and NP formulations of celecoxib have been attempted for specific delivery of celecoxib to the target tissue. Celecoxib has been incorporated in albumin microspheres,[45] PLGA NPs,[138] chitosan NPs,[46] high density lipoprotein NPs,[49] liposomes,[139] and immunoliposomes[140] for intravenous (i.v.) applications in RA and cancer. Nanoemulsions, microemulsions and gels have been investigated for transdermal delivery of celecoxib.[44,141] To reduce toxicity associated with oral administration, Soliman *et al.*[44] reported microemulsion gels and tested the anti-inflammatory effect of celecoxib via transdermal route in carrageenan-induced paw edema model. Using radiolabeled celecoxib and microspheres, Thakkar *et al*.[45] showed that microspheres produced 2.5 fold greater accumulation in arthritic joints compared to control after i.v. administration. The solution formulation of celecoxib revealed no difference between control and arthritic knees. This study demonstrates the advantage of using colloidal formulation to target inflamed sites for greater celecoxib accumulation. Likewise, Venkatesan *et al.*[46] used chitosan NPs to deliver celecoxib to colon cancer tissue, which showed tumor inhibitory effects. To reduce side effects and increase local levels of celecoxib, Kompella and group[42] formulated celecoxib into microparticles, which showed sustained release and reduced inflammation indicators in a diabetic retinopathy model utilizing an ocular route of delivery. Based on the studies, it can be concluded that alternate formulations and delivery routes have great potential to reduce limitations of oral celecoxib delivery, while increasing efficacy and safety.

2.4 Perfluorocarbon nanoemulsions

2.4.1 Perfluorocarbons in biomedical applications

PFCs are the hydrocarbons in which all or most of the hydrogens are replaced with fluorine. Fluorine, being the most electronegative atom with low polarizability. renders PFCs with strong intramolecular bonds and very weak intermolecular interactions.[142] Large numbers of low polarizable fluorine atoms and very weak van der Waals forces render unique physicochemical properties to PFCs such as low cohesivity, surface tension, viscosity, friction, aqueous solubility and diffusion rate, and high spreading, fluidity, compressibility, thermal and chemical resistance, biological inertness, high density, "superhydrophobicity" and lipophobicity.[142,143] The low polorizability of PFCs make them possess gas-like intermolecular bonds, thus leading to efficient gas-dissolving capability. The large van der Waals radius of fluorine compared to hydrogen (1.47 Å vs. 1.20 Å) makes fluorocarbon chains bulkier as compared to hydrocarbons. The bulkiness of the fluorine and low polarizability results in both enhanced hydrophobicity and lipophobicity. Due to the highly stable C-F bond, PFCs tend to show high chemical and thermal resistance, as well as biological inertness.[142]

Since PFCs are non-toxic and biologically inert, they have been investigated for more than 40 years in a variety of biomedical applications.[143] Figure 2.3 shows some of the PFCs widely investigated for biomedical applications. One of the earliest applications utilized the oxygen carrying capacity of PFCs for organ preservation, wound healing, liquid ventilation, and as artificial blood substitution. They have also been employed as contrast agents for CT, sonography and MR imaging.[144] The oxygen dissolving capacity was also exploited to sense partial oxygen pressure in order to image tumor

hypoxia.[145,146] The biological inertness and the light refraction properties of PFC polymers have also been applied in ophthalmology to prepare contact lenses and implantable cornea lenses.[147] PFC polymers were also used in reconstructive surgeries as vascular grafts and other devices.[143] Recently, there has been a renewed interest in the application of PFCs for ^{19}F MRI of externally injected formulations, which has been useful in tracking immune-therapeutic cells as well as in imaging macrophages/monocytes in a variety of diseases.[148] One of the emerging applications of PFCs is to combine their ultrasound echogenicity with the light absorbing potential of NIR dyes to obtain hybrid photo-acoustic images.[149]

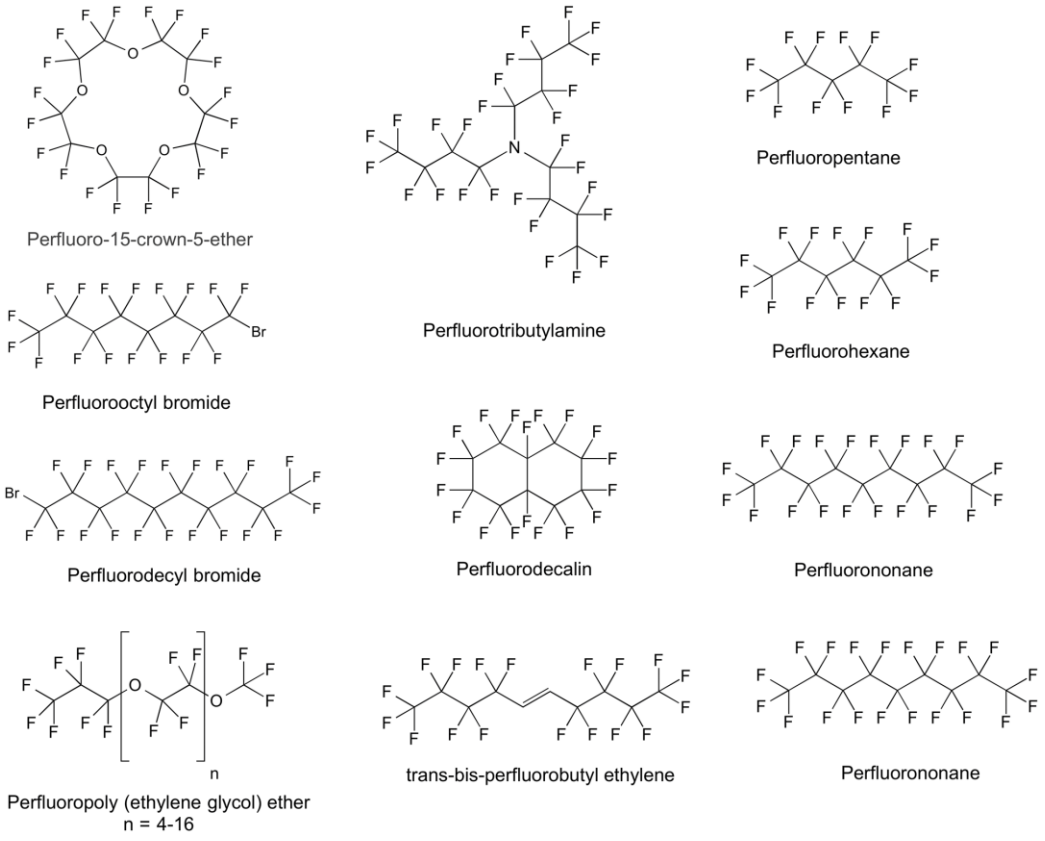

Figure 2.3. Chemical structures of PFCs utilized in biomedical applications. Applications of these PFCs is described elsewhere.[148,150-152]

2.4.2 Perfluorocarbons and challenges

Neat PFCs have been administered orally for image contrast purposes or directly to tumor tissues for oxygen sensing.[144] However, many applications necessitate access to blood circulation through i.v. route. Oral administration shows only a miniscule amount of PFCs in the systemic circulation. Neat PFCs cannot be injected because they are hydrophobic and lipophobic and hence can lead to vascular embolism. They do not interact with cell membranes and do not enter cells. Therefore, PFCs have been emulsified with surfactants to obtain biocompatible submicron-sized emulsions (i.e. nanoemulsions), which are typical formulations for *in vivo* applications. Chapter 3 provides more details about PFC formulations.

Although PFCs are biocompatible, there are several limitations when using them for clinical applications. Due to their hydrophobic and lipophobic nature, PFCs do not interact with biological material, and there are no known PFC-metabolizing enzymes,[152] rendering them biologically inert. However, many PFCs tend to accumulate in the tissues for a long time. They are eliminated in feces if administered orally. In i.v. applications, their body residence time can range from a few hours to months depending on their molecular weight, chemical structure, and vapor pressure. They are usually eliminated through lungs and hence high vapor pressure PFCs such as perfluorohexane (Figure 2.3) are exhaled faster. PFC emulsions accumulate in RES organs such as the liver and spleen, and they are cleared based on their vapor pressure. PFCs with lipophilic character, such as perfluorooctyl bromide (PFOB), are cleared relatively faster (biological $t_{1/2}$ = 12 days) when compared to fully fluorinated structures such as perfluoro-15-crown-5-ether (PFCE, Figure 2.3) whose biological half-life is greater than 250 days.[150] As a result, biomedical

applications that demand the injection of large amounts of PFCs are usually limited to preclinical research because high dose requirement makes obtaining regulatory approval a challenge.

2.4.3 Fluorescent/^{19}F MRI nanoemulsions as tools for drug delivery and macrophage imaging

PFC nanoemulsions have been increasingly used to image macrophages using ^{19}F MRI. NIRF modified PFC nanoemulsions to facilitate *in vitro* and *in vivo* imaging and confer multimodality have also been investigated. In this section, imaging modalities are described, followed by nanoemulsion application for macrophage imaging and drug delivery.

2.4.3.1 ^{19}F magnetic resonance imaging

MRI is a commonly used non-invasive clinical diagnostic tool applied in detection, staging, image guided surgery, and assessment of therapy responses in many diseases. MRI can detect nuclei containing an odd number of protons or neutrons, which exhibit spin. Charged nuclei with this spin produce a magnetic moment.[153] In the presence of a strong external magnetic field (1.5 to 11 Tesla), these magnetically susceptible nuclei such as ^{1}H align with the field and precess with a frequency called Larmor frequency. The combined effect of these precessing nuclei contributes to the net magnetization. Radio frequency pulses matching the Larmor frequency are then used to tilt the nuclei away from the direction of the external magnetic field. Once the pulse is removed, the nuclei release energy in the form of radio frequency signal and return to their native alignment with the magnetic field, which is detected to construct an image.

Based on the tissue environment, the density and relaxation properties of ^{1}H nuclei vary leading to contrast.

MRI can evidently delineate soft tissues and can be used for repetitive imaging sessions. It has high spatial resolution (~100 μm) and unlimited tissue penetration.[151] MRI has low sensitivity (10^{-3} to 10^{-9} M) and requires a long acquisition time.[22] Signal to noise ratio (SNR) in MRI can be increased by targeted contrast agents (SPIO or Gd), which function by altering the relaxation time of the surrounding protons, thereby producing contrast. Although contrast can enhance the local signal, the inherent inhomogeneities of tissues limit the unambiguous detection of a pathological condition.[151]

Alternatively, ^{19}F MRI can be used to circumvent the mentioned limitations of ^{1}H MRI. ^{19}F MRI detects organic fluorine, which is introduced exogenously into the body. Similar to ^{1}H, the fluorine (^{19}F) nucleus has a half spin, comparable MRI sensitivity (83%) and resonance (differs by 6%) to ^{1}H.[154] Therefore, ^{1}H MRI machines can detect ^{19}F nuclei by tuning to an appropriate frequency. ^{19}F MRI is not contrast imaging because there is virtually no imageable endogenous fluorine present in the body, except in the bones and teeth, where it is immobilized and cannot be detected by general MRI methods.[155] Due to this near zero background, ^{19}F MRI is a highly quantitative method. ^{1}H MRI can be registered during the same session to obtain anatomical context for the ^{19}F signal. Similar to ^{1}H MRI, ^{19}F MRI has low detection sensitivity, which necessitates the introduction of highly fluorinated PFCs into the body in biocompatible formulations such as NPs, liposomes and nanoemulsions. Unlike ^{1}H contrast agents, imaging prior to PFC administration is not required. Clinical use of ^{19}F MRI is still in its infancy. However,

recently its use has been documented in cancer patients for imaging injected therapeutic dendritic cells (DCs).[156]

2.4.3.2 Optical near-infrared fluorescence imaging

Optical fluorescence imaging is a widely employed tool for cellular, sub-cellular, and whole animal imaging in preclinical research, due to its low cost and high detection sensitivity (picomolar to femtomolar).[22] Fluorescence is the emission of light of a longer wavelength by molecules (fluorophores) absorbing a shorter wavelength of light. When fluorophores absorb photons, they are transitioned to an excited state. In this excited state, the molecule loses energy to its environment, finally returning to the ground state.[157] Because energy is dissipated in the excited state, the emitted light is seen at a longer wavelength, which forms the basis for fluorescence detection methods. The difference between the maxima of these excited and emitted light wavelengths is called the stokes shift.[157] Wavelengths in the visible to NIR region are used for fluorescence imaging.[158] Typically, an externally introduced fluorophore is used for fluorescence imaging. Light scattering and tissue attenuation limits the use of fluorophores active in the visible light region for deep tissue *in vivo* imaging. Absorption of tissue components, namely hemoglobin, water and lipids, are low in the NIR region (650-900 nm). Therefore, fluorophores active in the NIR region can reduce tissue absorption and increase penetration depth up to few centimeters.[158] Fluorescence imaging is regularly used in preclinical settings to visualize macrophages and the bioaccumulation of NPs.[64] Many organic and inorganic fluorescent dyes are used for this purpose such as cyanine derivatives (indocyanine green) and quantum dots.[159] Fluorescence imaging is clinically

used for surface tissue imaging (breast), intravital microscopy, and real-time image guided surgery.

Since no imaging modality provides all of the features for an optimal image construction, multiple imaging agents are integrated onto a single platform. Multimodal NPs with complementary imaging agents could offer high sensitivity detection, anatomical localization, and data validation from different imaging modalities. NIRF imaging is a promising technique due to low NIR absorbance by living tissues, high detection sensitivity, and minimal autofluorescence, but it is limited by fluorescence quenching, photobleaching, and tissue penetration. ^{19}F MRI has unlimited tissue penetration and it is a quantitative method, but it requires relatively large amounts of ^{19}F nuclei (μM to mM) at the target site.[155] By combining NIRF and ^{19}F MRI agents, sensitivity, specificity, and high tissue penetration can be obtained.[160] Aspects of multimodal imaging applied to drug delivery and macrophage imaging is discussed in the following section.

2.4.3.3 PFC nanoemulsions for drug delivery and imaging

^{19}F MRI has been widely investigated in the last decade for mostly cell tracking, and inflammation imaging through macrophage detection. Excellent reviews have been published in the area of *in vivo* cell tracking using ^{19}F MRI.[151,152,161] Briefly, cells of interest such as DCs and T-cells can be labeled *ex vivo* using PFC nanoemulsions and injected into the subject. The fate of these cells in the intact animal can be studied using ^{19}F MRI. Cell tracking has been applied to investigate the dynamic accumulation and clearance of T-cells from lymph nodes in a murine model.[162] It has been used to visualize

DC migration,[163] as well as to investigate the disease homing aspects of diabetogenic T-cells in a diabetes model.[164]

A more recent application of PFC nanoemulsions is *in situ* labeling of macrophages and imaging their accumulation to detect the inflammation loci. Successful *in vivo* macrophage visualization using ^{19}F MRI has been reported in a variety of chronic inflammatory models such as cancer,[165] RA,[166] IBD,[167] pulmonary inflammation,[168] and transplantation models.[169] Balducci *et al.*[166] utilized this approach to quantify inflammation and assess treatment effect in a rat model of RA. Excellent correlation was observed between clinical score of arthritis and the number of ^{19}F atoms detected in the arthritic joints. Furthermore, the effect of standard corticosteroid treatment showed a reduction in ^{19}F content indicating reduced inflammation. ^{19}F MRI has been used in other inflammation models (e.g. IBD and graft rejection), where the macrophage burden is reduced with therapeutic intervention concomitant with reduced ^{19}F content.[167,169] Recently multimodal fluorescent PFC nanoemulsions were investigated, where fluorescent dye enabled characterization by commonly employed fluorescent methods.[170] Balducci, and Wen *et al.*[171] reported a NIRF fluorescent PFC nanoemulsion to detect tumor-associated inflammation by ^{19}F MRI and NIRF. A strong correlation between these two imaging signals was observed in different organs. The presence of fluorescent dye facilitated the assessment of nanoemulsion accumulation in specific cell type using flow cytometry and histology.

The use of PFC nanoemulsions in drug delivery is slowly emerging. In these applications, PFCs were utilized to facilitate imaging by ^{19}F MRI, ultrasound, and photoacoustic methods.[172-174] An additional use was to trigger drug release by ultrasound.

Wickline and Lanza published several studies utilizing PFOB NPs incorporating fumagilin, melittin and other drugs for contact-mediated drug delivery in many disease models, which is reviewed elsewhere.[175,176] In these studies, ^{19}F MRI was used to detect the inflamed site and assess NP distribution to confirm drug deposition at the target site. Using an integrin-targeted PFC nanoemulsion, Fang *et al.*[177] developed acoustically active PFC nanoemulsions incorporating camptothecin and investigated *in vitro* anticancer effect. PFC was used to trigger drug release with ultrasound. To date, PFC nanoemulsions were never utilized to target macrophages in inflammation for simultaneous drug delivery and imaging.

3 Nanoemulsion development of a lipophilic perfluorocarbon conjugate as a ^{19}F MRI tracer for macrophage imaging

3.1 Introduction

As discussed in chapter 2, current PFC nanoemulsions face several challenges regarding their long half-life, imaging artifacts due to multiple peaks, and formulation challenges due to their immiscibility with common pharmaceutical excipients. These challenges prompted us to synthesize a new class of lipophilic PFC conjugates. The formulation of these conjugates was soon encountered with instability, specifically Ostwald ripening (OR). In this chapter, the efforts made to resolve this instability leading to a stable formulation will be discussed. *In vitro* assessment for stability, toxicity in model macrophages and uptake to establish ^{19}F MR properties is also presented. A theoretical background on nanoemulsions, their preparation methods, the mechanism of OR and the methods to form stable emulsions is provided. Part of the work presented in this chapter was originally published elsewhere.[178]

3.1.1 Nanoemulsions

An emulsion is a mixture containing immiscible phases, where one liquid is dispersed as droplets (dispersed phase) in another liquid (continuous phase). The dispersed phase is stabilized using surfactants in the continuous phase. A surfactant is a molecule containing amphiphilic parts in its structure that adsorbs at the interface of oil and water to reduce the interfacial tension and stabilize the droplets against coalescence by repulsive steric or electrostatic forces.[179] Emulsions can be oil-in-water (o/w) and water-in-oil (w/o), where water and oil are the continuous phases respectively. Emulsion

formation is not a spontaneous process and requires energy input. An exception to this is microemulsions, which are formed in the presence of large amount of surfactants and they are thermodynamically stable. The total free energy of emulsion formation (ΔG) is given by:[179]

$$\Delta G = \gamma \Delta A - T\Delta S \qquad \text{Equation 3.1}$$

where, ΔA is the change in interfacial area, γ is interfacial tension, T is temperature, and ΔS is change in entropy of the system.

Based on Equation 3.1, as smaller emulsion droplets are formed, new interfacial area is created, thereby increasing the free energy of the system. Surfactants are utilized to reduce the interfacial tension and the free energy.

Nanoemulsions are kinetically stabilized metastable systems with the droplet size below 100 nm. Although microemulsions can exist in this droplet size, they are not classified as nanoemulsions due to the fundamental difference in the mechanism of formation. In order to break an emulsion droplet into sub-micron sized droplets, enormous energy is required to overcome the Laplace pressure (Π) of the droplet, which is given by:

$$\Pi = 2\gamma/r \qquad \text{Equation 3.2}$$

where, r is the radius of the droplet. Smaller droplets have higher Laplace pressure and hence higher energy is required to break these droplets. Surfactants can reduce the Laplace pressure by reducing interfacial tension, making the droplet breakdown process easier. Following the breakdown, surfactants adsorb to the newly formed interface and stabilize the emulsions.

3.1.2 Nanoemulsion preparation using ultra sonication and microfluidization

The formation of nanoemulsions requires enormous energy in order to overcome the Laplace pressure (Equation 3.2) and break the larger oil droplets into nanometer size. Nanoemulsions can be prepared by low-energy and high-energy methods.[180,181] Low-energy methods generally utilize changes in composition (phase inversion), rate and sequence of ingredient addition, and environmental factors such as temperature (phase inversion temperature) to form nanoemulsions. Method of preparing self-nanoemulsifying drug delivery systems (SNEDDS) is widely utilized for pharmaceutical formulations, which can be categorized as low-energy method. However, these systems require a large amount of surfactants (20-50%), which could lead to undesirable side effects when administered. Also, these methods are limited by long-term stability and large-scale production.[180]

High-energy methods utilize high shear such as homogenization, microfluidization and ultrasonication, to break the droplets and form nanoemulsions. High-energy emulsification methods such as sonication and microfluidization are widely used at laboratory and industrial scale. In fact, these two processing methods are commonly employed to prepare PFC nanoemulsions. In ultrasonication methods, acoustic waves are generated, which disperse droplets of dispersed phase in continuous phase. An ultrasound-driven mechanical vibrator produces sound waves at frequencies greater than 20 KHz and high power causing shear and cavitation required for size reduction.[181-183] Ultrasonication equipment is readily available and it is an efficient method for generation of nanoemulsions at small scale. The inhomogeneous sound fields require constant recirculation/agitation of the mixture to achieve uniform size and low polydipsersity.

Microfluidization utilizes microfluidic technology, which was patented in 1985.[184] An air- or nitrogen-driven intensifier pump pushes the crude emulsion through an interaction chamber containing 75 μm channels in Y or Z shape. The fluid is forced through these microchannels as two process streams that collide at an impingement area.[181] This process creates high shear required to produce nanosized droplets. Microfluidization is a highly reproducible method and produces droplets with narrow size distribution.

3.1.3 Ostwald ripening and instability of perfluorocarbon nanoemulsions

Emulsions are thermodynamically unstable and hence emulsion breakdown is a spontaneous process to reduce free energy (Equation 3.1). Emulsions can destabilize by several mechanisms such as coalescence, flocculation, sedimentation, and creaming, which leads to phase separation.[185,186] In nanoemulsions, however, Ostwald ripening (OR) is observed as a major destabilizing mechanism. This degradation occurs due to the difference in chemical potential between large and small droplets in the internal phase.[185] Based on the Kelvin equation, small droplets display high local solubility. As a result, large droplets grow as the dispersed phase molecules from smaller droplets dissolve and diffuse in the continuous phase, finally leading to phase separation.[185] Because the size of the droplets in nanoemulsions is very small, the driving force for OR is greater. Several reports have emerged theorizing OR and solutions to reduce the same in emulsions. The theory proposed by Lifshitz, Slyzov and Wagner (LSW)[187,188] for solid dispersions has also been applied to emulsions, where the OR rate (ω) is given by:

$$\omega = \frac{dr^3}{dt} = \frac{8}{9}\left[\frac{C_\infty \gamma V_m D}{\rho RT}\right] \qquad \text{Equation 3.3}$$

where, D is the diffusion coefficient of the dispersed phase molecules in the dispersion medium, C_∞ is the saturation solubility of the dispersed phase in the continuous phase, C is the concentration of dispersed phase, γ is the interfacial tension between the two phases, and ρ is the density of the dispersed phase, V_m is the volume of dispersed phase, r is the radius of the emulsion droplets. R and T are the ideal gas constant and temperature respectively.

According to LSW theory, the OR rate can be decreased by reducing interfacial tension using surfactants, solubility of the oil phase by employing low aqueous solubility oils, and diffusivity of the dissolved oil by increasing the continuous phase viscosity. One of the widely utilized method involves use of a second oil phase with lower aqueous solubility then the disperse phase at the same time showing miscibility with the dispersed phase.[185] This second oil phase partitions between droplets and expected to be more associated with smaller droplets, thus reducing the solubility and the chemical potential difference between droplets leading to reduced OR.

The growth in droplet size of PFC nanoemulsions under storage was a key challenge to apply them as artificial blood substitutes during 1980s and 1990s. Kabalnov *et al.* published theoretical and experimental reports[189,190] suggesting that similar to hydrocarbon emulsions, PFC nanoemulsions also undergo OR, despite PFCs displaying low aqueous solubility. For example, one of the earliest PFC emulsions prepared with polyethylene oxide (PEO) and polypropylene oxide (PPO) block copolymers (F68) showed considerable increase in size under storage.[189,190] It has been observed that fluorocarbon emulsion stability depends on the nature of fluorocarbon, with long chain and highly fluorinated PFCs showing lower ripening rates, presumably due to the reduced

solubility in the aqueous phase.[189] It has also been shown that adding a second PFC with lower aqueous solubility can reduce the ripening rate similar to hydrocarbon emulsions.[190] It should be noted that the biological half-life of these PFCs are proportional to their molecular weights and structure, and hence the choice of PFCs depend on their potential interactions with biological systems. The use of fluorinated surfactants that solubilize in fluorous and aqueous phases is also proposed as another alternative to reduce OR by reducing interfacial tension between the phases, which reduces the driving force for diffusion. However, high toxicities associated with fluorinated surfactants, as well as their interference with ^{19}F nuclear magnetic resonance (NMR) peaks resulting in ^{19}F MRI artifacts, made the use of this method less practical. In contrast to F68-stabilized emulsions, phospholipid-based surfactants render good stability to PFC emulsions. The adsorbed phospholipid layer does not allow many non-electrolyte molecules to diffuse,[190] which could be the reason for high stability of PFC formulations prepared with this system. Nevertheless, phospholipid-based surfactants are limited, in addition to the cost, by chemical degradation (lipid oxidation) observed under storage.[191] PFC nanoemulsions were generally formed with either lipid-based surfactants such as phosphatidyl choline or block copolymer-based surfactants such as poloxamers.

3.1.4 Rationale

The motivation for developing new PFC conjugates is the problems associated with the current formulations in terms of stability as well as imaging efficiency. Lipophilic PFCs can overcome these problems by enhancing interactions with hydrocarbon surfactants and thus leading to stable formulations. PFCs displaying lipophilic character such as PFOB (Figure 2.3) are highly investigated because it has a

low half-life (12 days) in the body and well-characterized elimination pathways, making it more favorable candidate for clinical applications. Similarly, lipophilic-fluorophilic constructs could also present with higher elimination. For ^{19}F MRI applications, however, PFOB may not be best due to multiple peaks that could likely produce ^{19}F MRI artifacts. Optimal PFC nanoemulsions for ^{19}F MRI should mainly satisfy several design criteria[152]: 1) stability and long shelf life; 2) a simple ^{19}F NMR spectrum, ideally showing a single, narrow resonance in order to maximize sensitivity and prevent chemical shift imaging artifacts; 3) resistance to sedimentation (due to large density difference between PFC and aqueous phase) during storage; and 4) small molecular weight and lipophilic PFCs for faster excretion.

Herein, we report chemical modifications with formulation strategies of structurally simple, small molecular weight (<500 g/mole) perfluorocarbon-hydrocarbon (PFC-HC) conjugates to obtain stable and biocompatible nanoemulsion for ^{19}F MRI. We attempted two distinct approaches to overcome OR while optimal ^{19}F MRI reagent design criteria (1-4) remain satisfied. In the first approach, the effect of hydrocarbon chain length variation on the stability of PFC-HC nanoemulsion is investigated. The second strategy evaluated the effect of adding a hydrocarbon on the inhibition of OR.

3.2 Materials and methods

3.2.1 Materials

All reagents and solvents used in synthetic experiments were purchased from Sigma-Aldrich, Acros, TCI or Spectrum Chemicals (unless stated) and used without further purification. Pluronic® P105 was obtained from BASF Corporation. Pluronic® P123 and Cremophor-EL® (BASF) were obtained from Sigma Aldrich. Pluronic® F127

was purchased from Spectrum Chemicals. Pluronic® L121 is a gift from Dr. Eric T. Ahrens of Carnegie Mellon University. Olive oil used in nanoemulsion formulation was a generous gift from Croda International Plc. Acetone and chloroform were obtained from Fisher Scientific and Spectrum respectively. Trypan blue solution (0.4%) was obtained from Sigma-Aldrich. CellTiter-Glo® Luminescent Cell Viability Assay was purchased from Promega Corporation (WI, USA). Mouse macrophage cell line (RAW 264.7) was purchased from American Type Culture Collection (ATCC) (Rockville, MD, USA) and cultured according to the instructions. Dulbecco's phosphate buffered saline (DPBS) was purchased from Mediatech, Inc. (VA, USA). Dulbecco's modified eagle medium (DMEM; GIBCO-BRL, Rockville, MD, USA) for cell culture experiments was supplemented with 10% fetal bovine serum (FBS) or fetal clone III, Penicillin/Streptomycin (1%), L-Glutamine (1%), sodium pyruvate (1%), HEPES (2.5%), and 45% D(+) glucose (1%). Trypsin EDTA, 1X was obtained from Mediatech, Inc. (VA, USA). All cells were maintained in 37 °C incubator with 5% carbon dioxide (CO_2).

3.2.2 Synthesis of C8/C12/C14 PFTEs

Triphenylphosphine (Ph_3P, 11.11 g, 42.37 mmol) was added to a solution of 1-octanol (C8, 5.25 g, 40.35 mmol) in anhydrous ether, and the mixture stirred at room temperature (RT) for 15 minutes until the powder completely dissolved. The reaction mixture was then placed on an ice bath and diisopropylazodicarboxylate (DIAD) (8.71 mL, 44.38 mmol) was added dropwise. The addition was performed under argon atmosphere. During the addition, the solution changed color to pale yellow and a yellow precipitate was formed. After the addition was complete, the reaction mixture was stirred for an additional 30 minutes on the ice bath and then perfluoro-*tert*-butanol (1, 10.00 g,

42.37 mmol) was added in one portion, and the resulting mixture was stirred for 1.5 h at room temperature (RT). The crude reaction mixture was filtered over a short SiO_2 column to remove the triphenylphosphine oxide precipitate. The filtrate was concentrated, re-dissolved in a small amount of ether and loaded on a SiO_2 column. The product was eluted with a perfluorohexanes/ether (1:1 v/v) mixture and concentrated *in vacuo*. Removal of the unreacted perfluoro-*tert*-butanol under vacuum yielded C8 analog of perfluoro-*tert*-butyl ether (PFTE) as a clear colorless oil (8.36 g, 59.5%). C12, C14 and C18 analogs were synthesized following the same procedure using dodecanol, tetradecanol, and octadecanol as the starting materials respectively.

3.2.3 Nanoemulsion preparation using probe sonication and microfluidization

3.2.3.1 Nanoemulsions with Cremophor® EL and Pluronic® P105

Cremophor® EL/P105 surfactant mixture

A solution containing mixed surfactants was prepared as follows. 4 g of Pluronic® P105 (P105) was dissolved in 100 mL water by stirring slowly at RT for the final concentration of 4% w/v (weight/volume). 6 g of Cremophor® EL (CrEL) was dissolved in 100 mL water by stirring at RT for the final concentration of 6% w/v. The two solutions were mixed at RT in 3:2 v/v (volume/volume) ratio in a round bottom flask, placed in a water bath preheated to 45 °C, and heated while slowly rotating for 20 minutes on a rotary evaporator. The solution was then chilled on ice for 15 minutes, and stored in the refrigerator until use. The final concentration of this mixed micelle solution was 5% w/v, where 2% w/v was P105 and 3% w/v was CrEL.

Nanoemulsion preparation

Nanoemulsions were prepared using sonication at 0.5 mL scale. PFTE nanoemulsion contained 10% w/v PFTE (C8/C12/C14) and 0.5% w/v of CrEL and P105 in 3:2 ratios. Briefly, 50 mg of C8/C12/C14-PFTE and 50 μL of mixed micelle solution were vortexed and later hydrated by appropriate amount of water. A white dispersion was formed which was transferred to a 1.5 mL eppendorf tube for sonication. Probe sonication using Sonic Dismembrator (Fisher scientific, model 100) was used to prepare nanoemulsions. 1.5 mL eppendorf tube containing the sample was chilled on ice for 15 min before sonication. The dial reading was set at 3 which produce an output power of ~15 W during sonication. The sonication probe was inserted half-way inside the eppendorf tube to avoid any air entrapment. Pulses (5 sec) were manually applied with 5 sec interval between each pulse for 2 min. Tubes were placed on ice during sonication to avoid increase in temperature.

3.2.3.2 Nanoemulsions with single and mixed Pluronic® surfactants

Probe sonication

Nanoemulsions were prepared at 1 mL scale with Sonic Dismembrator (Fisher scientific, model 100). Stock solutions of surfactants either in de-ionized water (Pluronic® F127 and P105) or chloroform (Pluronic® P123 (P123) and L121) were prepared. Olive oil stock solution was prepared in acetone. Stock solutions of hydrophobic phases were mixed in a test tube to obtain the required final concentration of each ingredient. In C8-PFTE containing nanoemulsions, C8-PFTE was added directly to the mixture. The mixture was vortexed and blowing the air formed thin film. The samples

were stored in a desiccator under vacuum for 1.5 h to ensure complete removal of organic solvents. To the thin film, surfactant in water (where applicable) was added and vortexed vigorously. To this mixture, de-ionized water was added and vortexed for 1 min before transferring to a 1.5 mL eppendorf tube. Sonication was performed as described above.

Microfluidization

Stock solutions of P105 (5% w/v) in de-ionized water and P123 (10% w/v) in chloroform were prepared. Nanoemulsions were prepared at a 25 mL scale. Olive oil (1.25 g) and 4.5 mL of P123 (0.45 g) solution was transferred to a 250 mL round bottom flask. This mixture was subjected to solvent removal under reduced pressure (474 bar) at 38 °C and 100 rpm for 2 h to form a thin film and later placed in a desiccator for 2-3 h under vacuum. C8-PFTE (1.25 g) was added to this mixture under stirring, followed by 6 mL (0.3 g of P105) of aqueous P105 solution. The mixture was stirred for 15 min and de-ionized water was added in appropriate amount. The mixture was transferred to a pre-cooled microfluidizer (M110S, Microfluidics) and processed under recirculation for 30 pulses at an operating pressure of 6 bar (~18-20000 psi pressure in the interaction chamber). The nanoemulsion was sterilized using sterile 0.22 μm cellulose filter (Millex®-GS, 33 mm). Samples (1.5 mL) of the nanoemulsion were taken and stored at 4, 25 and 37 °C to assess their stability. The bulk of the nanoemulsion was stored at 4 °C and droplet size was monitored at different time points for all the samples. This nanoemulsion was designated as M2. For control nanoemulsion (M1) without C8-PFTE, 2.5 g of olive oil was used and the same procedure as above was followed.

3.2.4 Characterization for colloidal attributes, and cytotoxicity and uptake in RAW 264.7 cells

Droplet size and zeta potential measurements of nanoemulsions

The size distribution of the nanoemulsion droplets in aqueous medium was determined by dynamic light scattering (DLS) using Zetasizer Nano (Malvern Instruments, UK). DLS obtains hydrodynamic diameter (D_h) from the diffusion coefficient of the particles under Brownian motion using Stokes-Einstein equation.[192]

$$D_h = \frac{kT}{3\pi\eta D} \qquad \text{Equation 3.4}$$

where, k is Boltzmann's constant, T is absolute temperature, η is viscosity of the dispersion medium, and D is diffusion coefficient of the particle.

Diffusion coefficient is obtained by fitting the time autocorrelation data of the scattered light intensity with algorithms such as cumulants analysis. The two parameters obtained from the cumulants analysis and Equation 3.4 are mean diameter and an estimate of the width of the size distribution called polydispersity index (PDI).[192,193] PDI is a dimensionless number whose values range from 0 to 1. PDI is equal to the square of the ratio of standard deviation (width of size distribution) to mean diameter.[194]

Measurements were taken after diluting the nanoemulsion in water and equilibrating at RT for at least 20 minutes prior to each measurement. For nanoemulsions prepared with olive oil alone, 1:200 v/v dilution ratio was used and C8-PFTE containing nanoemulsions were diluted at 1:40 v/v ratio. Measurements were performed at 20 ºC and an angle of 173º (to incident light) to avoid multiple scattering. The stability of the nanoemulsions was assessed by measuring hydrodynamic diameter (Z average) and PDI

at different time points (days). Zeta potential was measured using specialized zeta cells (Malvern) with electrodes at same dilution used for size measurement. Following the same procedure, droplet size measurements were also carried out for M2 nanoemulsion dispersed (1:40 v/v) in di-water, serum-free cell culture medium (DMEM), and 10% v/v FBS-containing medium. These samples were incubated at 5% CO_2 and 37 °C and monitored for 3 days.

In vitro cytotoxicity

In vitro cytotoxicity and labeling was performed in mouse macrophages (RAW 264.7, ATCC). For cytotoxicity, cells were plated at 10,000 per well in 96 well plate. After overnight incubation at 37 °C and 5% CO_2, cells were exposed to nanoemulsion (M1 or M2) dispersed in culture medium. A wide range of concentrations (0.375-12 mg/mL C8-PFTE or olive oil) was used. For M1 nanoemulsion, theoretical olive oil concentration was used. Following 24 h of exposure, 50 μL of CellTiter-Glo® analyte was added to each well and shaken for 20 min at RT. 100 μL of the cell lysate was transferred to a white opaque plate and luminescence recorded on Perkin Elmer Victor 2 Microplate Reader.

Cell uptake with nanoemulsion M2

For cell labeling, cells were plated at 0.8 million per well in 6 well plates and left undisturbed overnight. After 24 h, cells were exposed to different doses of C8-PFTE in nanoemulsion M2 (8, 4, 2, 1, 0.5 and 0 mg/mL). Each well contained 2 mL of medium with or without nanoemulsion M2 and labeling was performed in duplicates. The

attached cells were washed with DPBS (2x) and medium (1x). To collect the labeled cells, 0.5 mL of TrypleE was added to each well, incubated for 2 min and cells collected after repeated washing with medium. Collected cells were centrifuged at 1100 rpm for 5 min (Centrifuge 5804R, VWR) and the supernatant was aspirated. The obtained cell pellet was re-dispersed in 3 mL medium. Only unexposed cells were counted. Briefly, an equal volume of cell suspension and 0.4% Trypan blue solution was mixed and cells counted using neubauer hemocytometer. To quantify the number of cells in nanoemulsion M2 exposed cells, CellTiter-Glo® cell viability assay was used. Based on the cell counts, a standard curve was constructed using serial dilutions of unexposed cells and recorded luminescence from the CellTiter-Glo® assay. Briefly, 100 µL of cell suspension and 50 µL of the analyte were added to an opaque 96 well plate and shaken at RT for 20 min. By using the obtained regression equation, cell numbers were predicted for nanoemulsion-exposed samples. The cell suspensions were centrifuged at 2000 rpm for 10 min and supernatant aspirated. To the obtained cell pellet, 180 µL of de-ionized water and 200 µL of 0.02% v/v aqueous trifluoroacetic acid (TFA) solution was added and transferred to 5 mm NMR tube for ^{19}F NMR analysis.

^{19}F NMR of nanoemulsion M2 and labeled cells

^{19}F NMR of the nanoemulsion and above prepared cell suspension was recorded on Bruker Instruments (Bruker Instruments, 300 MHz). 200 µL of nanoemulsion was diluted with 200 µL of 0.2% v/v aqueous TFA. Amount of C8-PFTE in the emulsion and ^{19}F per cell was quantified based on the following equations using TFA as the reference (peak at -76.0 ppm).[170]

$$\text{Amount of PFTE per mL} = \frac{5\left(\frac{\text{Fne}}{\text{Fr}}\right)\text{Nr}}{N_A * \frac{^{19}\text{F}}{\text{molecule}}} \qquad \text{Equation 3.5}$$

$$^{19}\text{F per cell} = \frac{\left(\frac{\text{Fne}}{\text{Fr}}\right)}{\text{Cell number}} * \text{Nr} \qquad \text{Equation 3.6}$$

Fne is the integrated PFC peak value around -71.5 ppm; Fr is the integrated reference peak value under -76 ppm; Nr is the number of fluorine atoms in TFA used for analysis; N_A is Avogadro number (6.023×10^{23}); Mwt is the molecular weight of PFC. ^{19}F/molecule are the number of fluorine atoms (nine) in PFTE structure. The multiplication factor used is five (200 µL of nanoemulsion was used in NMR tube) to obtain the amount per mL nanoemulsion. The equations are adapted from earlier ^{19}F content calculations reported in the literature.[164,170]

3.3 Results and discussion

Currently used PFCs either possess high body residence time or multi-peak ^{19}F NMR spectrum leading to imaging artifacts and a reduction in the ^{19}F MRI sensitivity. PFOB has low body residence time and the newer imaging methods addressed the problems associated with imaging artifacts to some extent.[150] However, it has been shown that PFOB only shows 37% of PFCE intensity in inflammation models.[150] This reduced sensitivity, in turn, requires high dose administration of PFOB, thus increasing body burden. The number of ^{19}F nuclei used for imaging is significantly lower (three ^{19}F atoms per molecule) compared to the total number of fluorines (17 ^{19}F atoms) in PFOB. Therefore, we set out to synthesize lipophilic analogs of a previously reported PFC

conjugate and address formulation challenges pertaining to OR-dependent instability and evaluation of methods to reduce the same.

Analogs of PFTE were synthesized in one step using an earlier reported Mitsunobu protocol[195] with some modifications (Figure 3.1A). The addition of aliphatic hydrocarbon tails increased lipophilicity of the constructs, which facilitated PFC interaction with hydrocarbon surfactants. Further, the overall density of the PFC construct is substantially lower (1.18 g/mL). The construct shows only one peak at -71.4 ppm from the perfluoro-*tert*-butyl group, equivalent to nine ^{19}F atoms (Figure 3.1B). In preliminary studies by Janjic *et al.*[196], C8-PFTE emulsified with non-ionic surfactants in water efficiently labeled mouse DCs and the cells injected into mouse leg were imaged by ^{19}F MRI. However, this nanoemulsion was not stable upon prolonged storage and its preparation was not scalable.

Our C8-PFTE nanoemulsion formed with CrEL and P105 also showed an increase in droplet diameter with time (Figure 3.2A). A plot of droplet volume (r^3) vs. time revealed a linear increase in size with time (Figure 3.2B) indicating an OR-like phenomenon. Several reports have shown that OR rates decrease with increase in carbon number in both hydrogenated and fluorinated alkanes.[185,190] Therefore, PFTE with increased chain length (C12 and C14) were synthesized and formulated employing the same surfactant system. Increased chain length showed some stabilization in the droplet size, but size fluctuations were observed during DLS analysis (Figure 3.2C). Chain length was further increased to C18, which produced a waxy solid, not amenable for incorporation in the nanoemulsion. The synthetic yields also reduced with increasing

chain length. Therefore, alternate strategies were employed to reduce OR in the nanoemulsion.

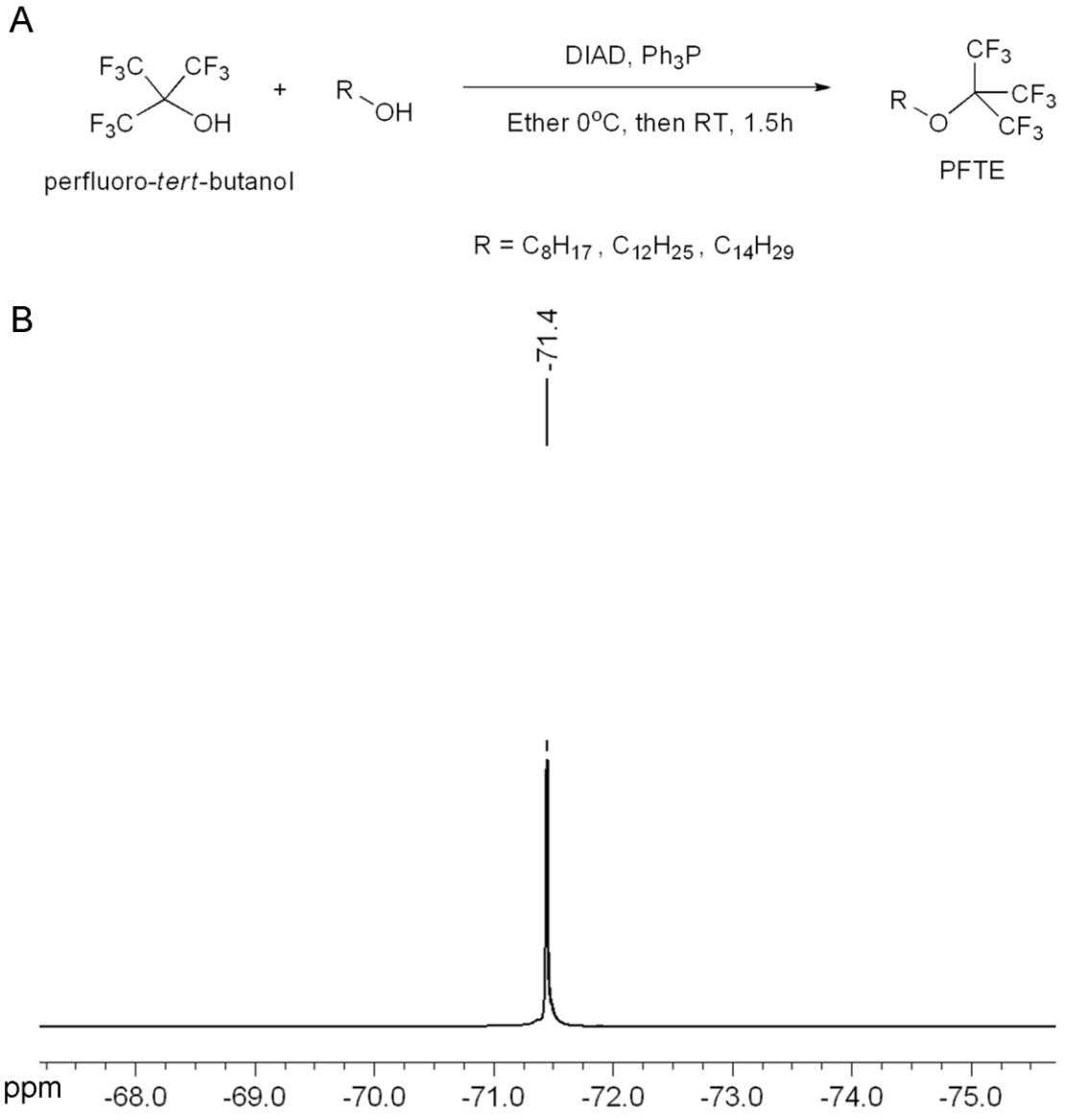

Figure 3.1. Synthesis and representative ^{19}F NMR of PFTE analogs.

A. Synthetic scheme of PFTE formation. **B.** ^{19}F NMR of C8 analog of PFTE showing single peak.[178]

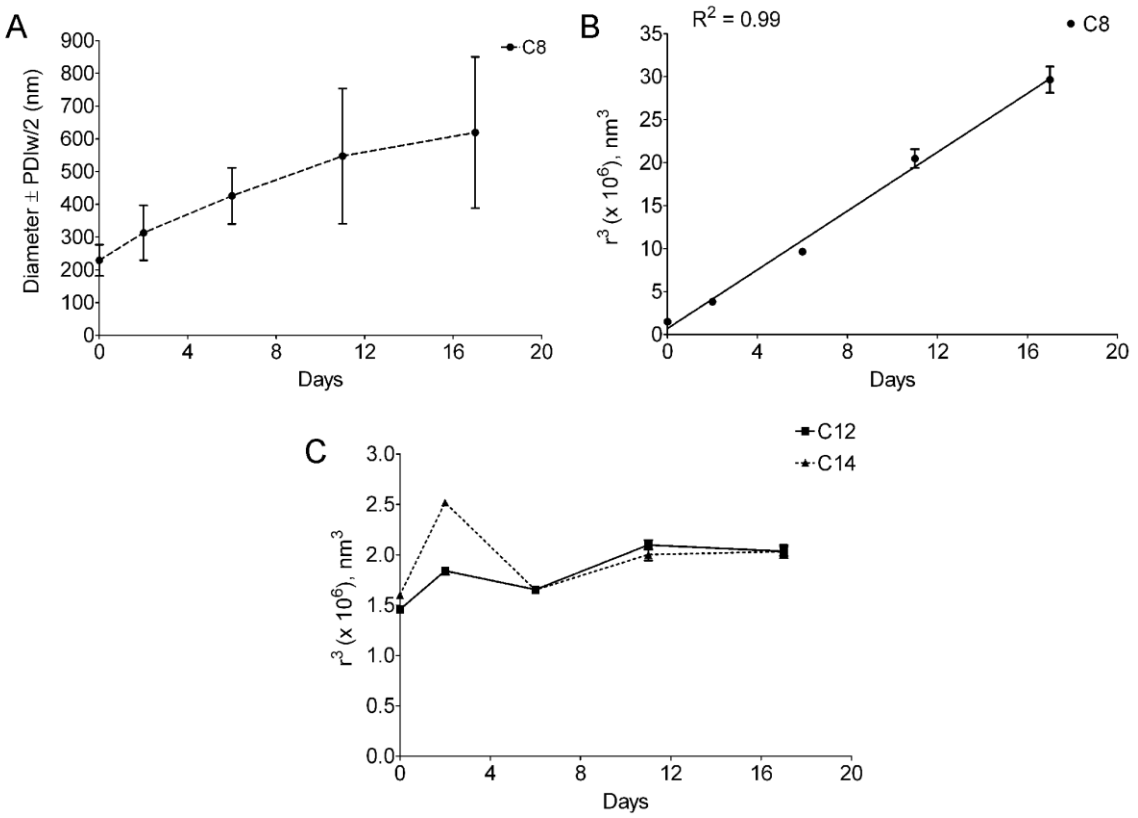

Figure 3.2. Instability of CrEL/P105/PFTE nanoemulsions based on droplet size changes with time.

A. Increase of droplet diameter with days for C8-PFTE nanoemulsion (n=2). **B.** Data from panel A plotted as cube of radius (r^3) vs. days showing a linear increase in volume with time. **C.** Cube of radius (r^3) vs. days plot of C12- and C14-PFTE nanoemulsions (n=2) showing fluctuation in size at the initial time points.

3.3.1 Formulation development of C8-PFTE

To stabilize the nanoemulsion prepared with C8-PFTE against OR, a large molecular weight hydrophobic molecule (ripening inhibitor) miscible with the dispersed phase, but practically insoluble in the continuous phase was utilized. It is well established that nanoemulsions can be stabilized against OR using a low diffusive hydrophobic component in the dispersed phase.[197] Lipophilic C8-PFTE is readily miscible with olive oil, thus avoiding the use of large molecular weight PFCs, which might produce

interfering signals for ^{19}F MRI. Here, the hydrocarbon oil and C8-PFTE are mixed in a 1:1 ratio forming a mixed internal phase, which is stabilized by surfactants in water. With higher hydrocarbon oil content, there is an opportunity to incorporate additional imaging agents (e.g. fluorescent dyes) or lipophilic drugs in the formulation.

Selection and optimization of surfactants

To obtain a stable nanoemulsion, systematic selection of surfactants and optimization of their concentration was followed. Biocompatible phospholipids are widely employed to provide stable nanoemulsions. However, phospholipids are expensive and can undergo oxidation/peroxidation reactions upon prolonged storage.[191] Alternatively, non-ionic block copolymers of PEO and PPO (Poloxamers/Pluronics®) can be used for PFC nanoemulsion stabilization.[152,170,196] Non-ionic block copolymers are inexpensive, biocompatible and generally regarded as safe.[198]

The first phase of formulation development included selection of surfactants and their amount(s) that form nanoemulsions of desired characteristics. Olive oil alone was used as the dispersed phase because it is inexpensive compared to C8-PFTE. Also, olive oil is part of the proposed final formulation, where it was intended to act as an OR inhibitor. Olive oil is widely used in topical, oral and injectable pharmaceutical formulations.[199] Nanoemulsions were prepared at small scale (1 mL) using probe sonication. Surfactants were screened either alone or in combination with another surfactant. Optimized formulations were selected based on droplet diameter (< 200 nm), PDI (< 0.2) and visual observation for formulation homogeneity. Table 3.1 summarizes characterization of test formulations (S1-S6) prepared with olive oil. The dispersed phase

concentration was maintained at 10% w/v while surfactants were screened at 1, 3 and 5% w/v (Table 3.1). A 1:1 w/w ratio between surfactants was used for the dual surfactant systems. Figure 3.3 shows nanoemulsion size dependence on surfactant concentration. Droplet size and PDI were dependent on surfactant concentration, but not on the type or combination of surfactants. Both 3 and 5% w/v showed droplet diameter and PDI less than 200 nm and 0.2 respectively for formulations S1, S2, S5 and S6, whereas 1% w/v produced nanoemulsions with size and PDI larger than 200 nm and 0.2 respectively. The observed increase in size at low surfactant amount can be attributed to the relatively low amount of surfactant available to stabilize the increased interfacial area during droplet formation. Based on this result, it can be concluded that 3% w/v is the lowest surfactant concentration meeting desired criteria. Formulation S3 containing L121 and P105 showed phase separation, while formulation S4 formed a gel during thin film leading to further processing problems. Table 3.1 shows droplet size (diameter), half width of polydispersity index (PDIw/2) and PDI of all formulations prepared at 3% w/v surfactant concentration. Though P105 showed optimum stability, P123/P105 (S6) was selected due to its low hydrophilic-lipophilic balance (HLB) value of 12.25. Average HLB values of P123 and P105 were taken as 9.5 and 15 respectively.[200]

Optimization of relative amount of Pluronic® P123 and P105

Having selected P123/P105 surfactant combination, the relative ratio of P123 and P105 was optimized based on droplet size (< 200 nm), PDI (< 0.2), and size changes with time. For this set of experiments, a 1:1 combination of olive oil and C8-PFTE was employed as the dispersed phase. C8-PFTE was introduced into the nanoemulsion by

equal weight replacement of olive oil. The total dispersed phase concentration was maintained at 10% w/v. The concentration of surfactant system was held constant at 3% w/v. The relative ratios of P123 and P105 were changed as shown in Table 3.2.

Table 3.1. Summary of formulations prepared with 10% w/v olive oil and 3% w/v surfactant system. Where two surfactants are used, they were at 1:1 w/w ratio.

Formulation	Surfactant 1 Pluronic®	Surfactant 2 Pluronic®	Droplet size ± PDIw/2 (nm)	PDI	Visual Observation
S1	F127	P123	180.0±29.5	0.11	a, b
S2	F127	P105	173.0±25.4	0.08	b
S3	L121	P105	-	-	c
S4	P123	-	-	-	a
S5	P105	-	173.4±33.7	0.15	Homogenous
S6	P105	P123	172.0±35.9	0.17	Homogenous

[a] Gel formation during thin film leading to surfactant loss during transfer
[b] Thick texture based on visual observation
[c] Phase separation

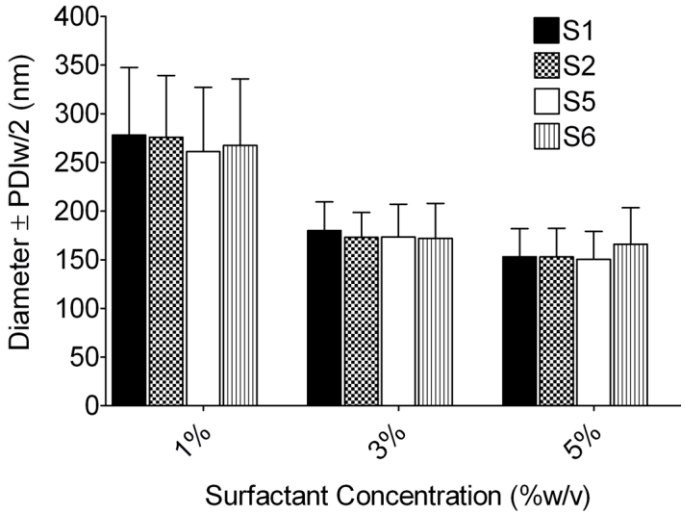

Figure 3.3. Droplet diameter changes with surfactant amount for olive oil nanoemulsions.

Nanoemulsions were prepared with probe sonication. Data for nanoemulsions S1, S2, S5 is an average of duplicate experiments. Data from S6 represents one experiment. Error bars represent PDIw/2.[178]

Table 3.2. Summary of nanoemulsions prepared with C8-PFTE/olive oil (1:1) and Pluronic® P123 and P105 as surfactants (3% w/v).

Formulation	P123:P105	HLB	Droplet diameter ±PDIw/2 (nm)	PDI	Zeta Potential ±SD (mV)	Stability
S7	1:1	12.25	148.8 ± 27.3	0.13	-8.8 ± 1.9	Stable
S8	3:2	11.70	152.0 ± 26.8	0.12	-9.0 ± 2.0	Stable
S9	2:3	12.80	159.0 ± 33.7	0.19	-11.0 ± 3.4	Stable

Nanoemulsions (S7-S9) formulated using probe sonication showed droplet size and PDI less than 200 nm and 0.2 respectively. All the formulations showed stability for at least 12 days as assessed by DLS (Figure 3.4A). PDIw/2 was used as standard deviation in order to follow the changes in size distribution with time. Zeta potential values were in the range of -8 to -11 mV (Table 3.2). Formulation S8 was selected because the surfactant ratio corresponds to a HLB value of 11.7, which is lowest among the tested combinations. Due to the presence of hydrophobic dispersed phase, a lower HLB value was preferred. Replacement of a portion of olive oil with C8-PFTE has not affected the stability of the nanoemulsion. Also, by comparing formulations S6 (Table 3.1) and S7 (Table 3.2), the average droplet diameter was reduced by 20 nm after replacing olive oil with C8-PFTE. This reduction in size can be attributed to the low molecular weight and high density of C8-PFTE compared to olive oil. To validate the use of olive oil as ripening inhibitor using this surfactant system, C8-PFTE alone nanoemulsion with P123/P105 at the above selected ratio and amount was prepared. A time-dependent increase in droplet diameter was seen (Figure 3.4B) further validating the use of olive oil to stabilize the nanoemulsion.

Preparation and characterization of microfluidized nanoemulsions

In the screening phase, all nanoemulsions were prepared using probe sonication. To prepare S8 nanoemulsion on a scale necessary for further cell studies, processing was changed from sonication to microfluidization. It was observed that microfluidization formed nanoemulsions with smaller size and PDI compared to sonication. The thin film formation step was modified for microfluidized C8-PFTE nanoemulsion compared to sonicated samples (S7-S9). During thin film formation on rotary evaporator, we observed that C8-PFTE evaporates at temperature (38 °C) and pressure (474 bar) utilized for removal of chloroform. Therefore, C8-PFTE was added after thin film formation of olive oil and Pluronic® P123. This new formulation is designated as M2. Control nanoemulsion with olive oil alone was also prepared using microfluidization and designated as M1. Nanoemulsions M1 and M2 were characterized for droplet size, PDI and zeta potential using DLS.

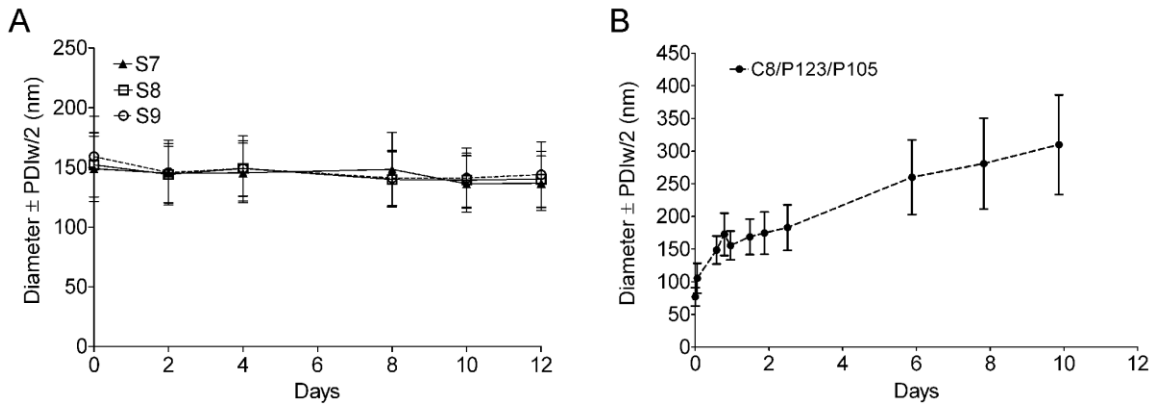

Figure 3.4. Effect of olive oil on C8-PFTE nanoemulsion stability.

A. Nanoemulsion diameter changes with time for combined C8-PFTE and olive oil containing nanoemulsions (n=2) and **B.** Nanoemulsion containing C8-PFTE, but not olive oil (n=1).[178]

Droplet size distribution showed a single peak (Figure 3.5A) indicating the absence of significant portion of large and small droplets. The average droplet size and PDI were around 180 and 0.2 for nanoemulsion M1 while nanoemulsion M2 showed a reduced droplet size and PDI around 130 nm and 0.15 respectively (Figure 3.5A-C). This reduced droplet size of nanoemulsion M2 is consistent with the sonicated nanoemulsions. Zeta potential values for nanoemulsions M1 and M2 were negative, -5 to -7 mV. For stable colloidal preparations, large zeta potential values (> ±30 mV) are preferred to ensure repulsion between the droplets.[201] However, Pluronics can provide stabilization via steric hindrance rather than charge repulsion. Storage stability was evaluated at 4, 25 and 37 °C by analyzing nanoemulsion samples at regular time intervals using DLS. Both formulations were shown to be stable for 160 days at all temperatures tested (Figure 3.5B-C).

Physical stability of nanoemulsions in cell culture relevant conditions was also evaluated. Droplet size and PDI were characterized for nanoemulsion M2 dispersed in water, serum-free medium, and 10% v/v fetal bovine serum (FBS)-containing medium. In all the media tested, nanoemulsion M2 showed high physical stability for at least 72 h stored at 37 °C and 5% CO_2 (Figure 3.5D). A small increase in size (~10 nm) was noted for serum-free and serum-containing medium. Quantification by ^{19}F NMR of nanoemulsion M2 showed a high C8-PFTE loading (48.4±0.92 mg/mL) in the nanoemulsion, which is 96% compared to theoretical concentration (50.4 mg/mL).

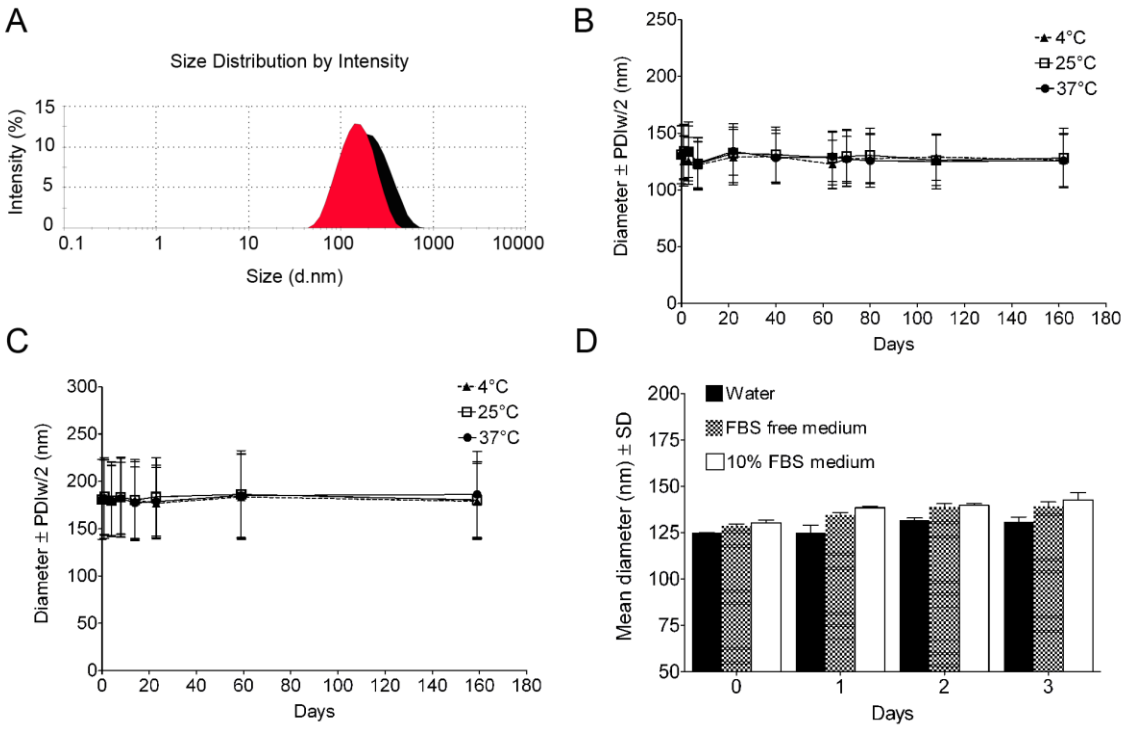

Figure 3.5. Physical characterization of microfluidized olive oil (M1) and C8-PFTE/olive oil (M2) nanoemulsions using DLS.

A. Representative size distribution of M1 (black) and M2 (red) nanoemulsions. **B.** Long term storage stability of M2 and **C.** M1 nanoemulsions at 4, 25 and 37 °C assessed by droplet size measurements. **D.** M2 nanoemulsion diameter changes in different media (n=3). The error bars in panels B and C represent PDIw/2.[178]

In vitro stability results demonstrate that lipophilic PFC can interact effectively with excipients and form stable formulations. Because the obtained droplet size is larger than 100 nm with low PDI and a slight negative charge, these nanoemulsions meet the design criteria discussed in section 1.4 and could be internalized by macrophages.

3.3.2 *In vitro* cell culture studies

To demonstrate the biocompatibility and potential biomedical use of C8-PFTE nanoemulsions, *in vitro* cell culture studies were performed in a model phagocytic cell line, mouse macrophages (RAW 264.7). These cells are commonly utilized for *in vitro*

toxicity and uptake studies due to their phagocytic properties. Similar to primary monocytes and macrophages, these cells can be activated *in vitro* to pro- and anti-inflammatory states using LPS and interleukin-4 and 13 (IL-4 and 13) respectively.[202,203] Nanoemulsion M2 was exposed to macrophages for 24 h at different doses of C8-PFTE (0.375-12 mg/mL). A dose-dependent reduction in cell viability was observed (Figure 3.6A). Cell viability showed a plateau from 3-12 mg/mL concentration with 80% viable cells. Bonetto *et al.*[204] observed a similar level of cell viability for a PFC nanoemulsion and the authors stated that this is acceptable toxicity for *ex vivo* cell labeling used in cell tracking studies. Cell viability of nanoemulsion M1 (control) was assessed at the same total oil concentration as that of nanoemulsion M2. It showed about 20% increase in cell viability (Figure 3.6B).

Macrophages were labeled with nanoemulsion M2 at different concentrations of C8-PFTE for 24 h. Unexposed macrophages were counted and serial dilutions were prepared. Obtained luminescence values (CellTiter-Glo®) for serial dilutions were used to get a regression equation (R^2 = 0.998). Using this equation, cell numbers were predicted for cells exposed to nanoemulsion M2. Labeled macrophages were subjected to ^{19}F NMR analysis to quantify the loading efficiency. As shown in Figure 3.6C, peak shape was unaltered in cells showing that C8-PFTE is metabolically stable. A dose-dependent uptake of nanoemulsion M2 in macrophages was observed (Figure 3.6D). At the highest C8-PFTE concentration tested (8 mg/mL), cell loading was around 7 x 10^{11} ^{19}F per cell, which is comparable to cell loading reported earlier (10^{12} ^{19}F/cell).[151,170] It should be noted that the current nanoemulsion had only 5% w/v PFC compared to other reports, which utilized a higher PFC content (~10-40 % w/v) in the

nanoemulsion.[169,170,196] Nanoemulsion with increased amount of C8-PFTE could further increase ^{19}F per cell.

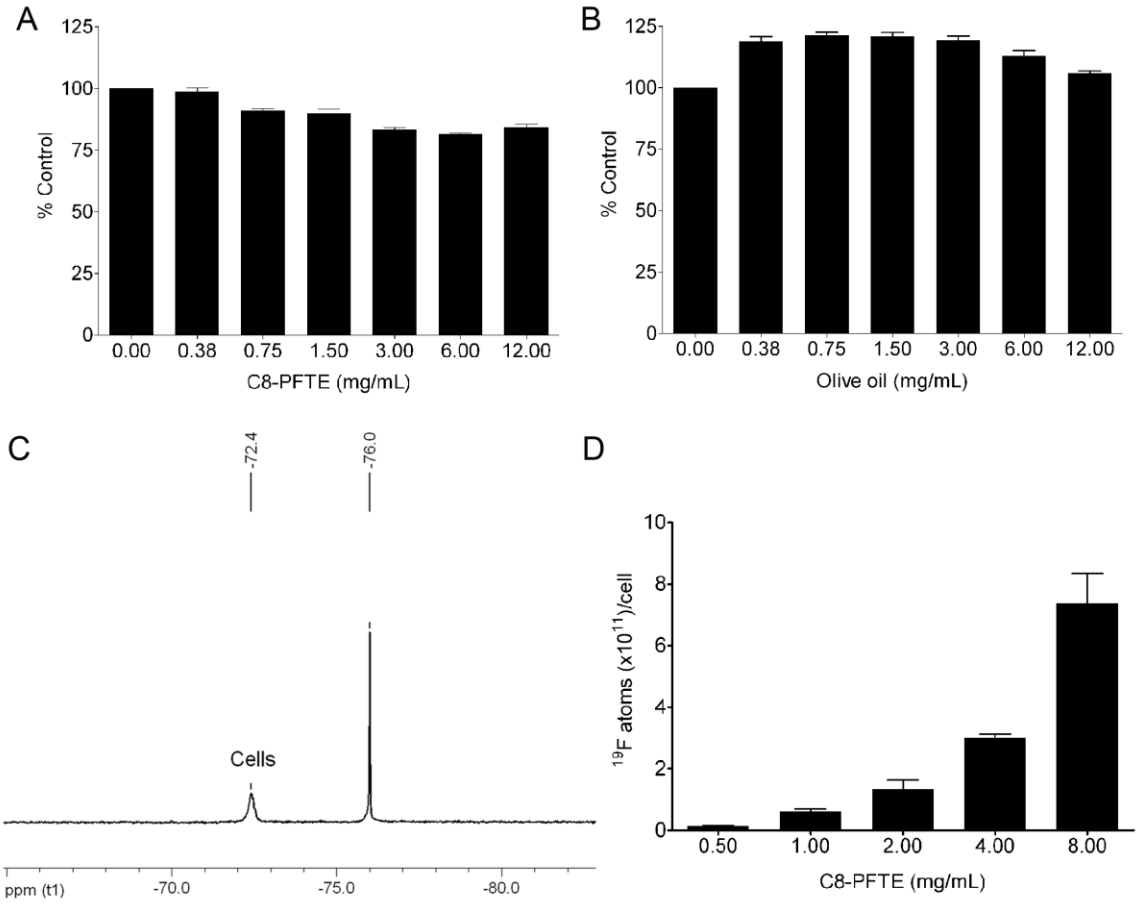

Figure 3.6. *In vitro* characterization of olive oil (M1) and C8-PFTE/olive oil (M2) nanoemulsions in mouse macrophages.

A. Macrophage viability (n=4) post 24 h exposure to dilutions of M2 and **B.** M1 nanoemulsions. Data is represented as percent of control (0 mg/mL C8-PFTE or olive oil). **C.** ^{19}F NMR of nanoemulsion M2-labeled macrophages; the resonance peak at -76.0 ppm is TFA reference. **D.** Dose-dependent uptake of nanoemulsion M2 in macrophages (n=2). In panels A and D, data is represented as mean ± SD.[178]

3.4 Conclusions, limitations and alternatives

In conclusion, the work presented in this chapter identifies a new class of PFC-HC conjugates for biomedical applications. Lipophilicity, a large number of magnetically equivalent ^{19}F nuclei for imaging and low density are the hallmarks of this class of PFCs. Addition of less soluble olive oil to C8-PFTE produced nanoemulsions resistant to OR compared to nanoemulsion prepared with C8-PFTE. A combination of lipophilicity and low density imparted high stability to the PFTE nanoemulsions under storage and incubation with cell culture media. Dose-dependent uptake in macrophages showing ^{19}F MR signature supports the nanoemulsion suitability for imaging.

Although, a stable formulation of C8-PFTE nanoemulsion was developed, a few limitations were encountered during the course of formulation characterization to use this emulsion as a theranostic system. At high doses, C8-PFTE showed up to 20% reduction in cell viability, which necessitates further investigation for future *in vivo* applications involving direct injection and *in situ* labeling of macrophages. We also noted that celecoxib precipitated under storage in the nanoemulsions leading to its instability. This result is expected as celecoxib shows very low solubility in olive oil. Hence, an alternative or additional hydrocarbon solubilizer needs to be incorporated in the formulation. Because large-scale synthesis of C8-PFTE that is required for further optimization and drug incorporation studies is an expensive endeavor, our focus shifted to commercially available PFCs (chapters 4, 5 and 6). Nevertheless, the reported nanoemulsion can find applications in multi-spectral ^{19}F MRI due to its single ^{19}F resonance peak, which is easily distinguishable from the widely used PFCs such as PFPE and PFCE. C8-PFTE can be utilized in combination with these PFC nanoemulsions to

detect two cell populations and their interactions *in vivo*, which could be applied in cell therapy and understanding cell-cell interactions in a pathophysiological setting. This way complicated MRI pulse sequences to separate ^{19}F signal from each of these compounds are not required. It can also be utilized as a ^{19}F MRI tracer to monitor cell infiltration changes in response to drug delivery by a distinct PFC nanoemulsion incorporating drug. In this case, the availability of distinct peaks can be utilized separately to assess therapeutic effect and visualize theranostic accumulation.

4 Development of fluorescent celecoxib-loaded PFPE nanoemulsions for drug delivery and imaging in macrophages

4.1 Introduction

Due to the limitations associated with C8-PFTE formulation, we investigated linear perfluoropolyether, PFPE (Figure 2.3). PFPE is represented by the formula $CF_3O(CF_2CF_2O)_nCF_3$, where n = 4-16, with the average molecular weight of 1380 g/mol. PFPE shows a single main peak around -91.5 ppm[205] in the ^{19}F NMR spectrum corresponding to the monomer repeats CF_2CF_2O. The total number of magnetically equivalent fluorines around -91.5 ppm is 40. A small peak around -59 ppm from CF_3 end groups in the PFPE spectrum is spectrally separated and hence its presence does not affect the image analysis.[163] PFPE was previously used for *in vivo* ^{19}F MRI tracking of *ex vivo* labeled immune cells (T cells and DCs),[163,170,204] *in vivo* cytometry,[162] and it is also evaluated in cancer patients to track injected immunotherapeutic DCs.[156]

PFPE is an ideal PFC to be applied for *in vivo* ^{19}F MRI studies due to its non-toxic nature as well as the presence of large number of ^{19}F to increase imaging sensitivity.[156] Due to high biological inertness, PFPE elimination is slow and relies on the RES followed by expiration through lungs.[152] This is the general clearance profile for most PFCs used in biomedical applications.[151,152,190] Of note, *in vivo* assessment in our studies (chapter 7) are conducted only up to 3 days and hence our study end points are not affected by PFPE retention at the inflamed site. For studies involving chronic inflammation models and utilizing multi-dose administration of PFPE nanoemulsions, further characterization *in vivo* is necessary.

Our goal was to prepare a theranostic system with acceptable storage stability and following capabilities: 1) incorporates a selective COX-2 inhibitor; 2) can be imaged by two complementary molecular imaging techniques - NIRF and ^{19}F MR; 3) Non-toxic; 4) can be internalized by macrophages in culture; and 5) produce therapeutic effect.

Since pure PFCs are lipophobic, they cannot incorporate lipophilic drugs.[143] Previous reports showed the incorporation of therapeutic moieties in the surfactant layer surrounding PFC core of a nanoemulsion droplet.[172,173] Premature leaking or burst release of the drug *in vivo* or during storage is a potential problem with this approach because the surfactant layer resides at the oil/water interface. Since the surfactant amount used in kinetically stabilized nanoemulsions is minimal (<5% w/w), amount of drug that can be incorporated will be very low. An alternate approach is to use solubilizers in the formulation. For example, coconut oil was used to solubilize lipophilic drug, camptothecin, in a PFC emulsion.[177]

Celecoxib solubility in several natural and synthetic oils has been reported in the literature.[44] Oils such as safflower, olive and corn were reported to have less than 5 mg/mL solubility. Caprylic/capric triglycerides such as Capmul and Miglyol 810/812 N showed up to 10 mg/mL solubility. Our target concentration of celecoxib in the oil phase is 5 mg/mL, which corresponds to a theoretical concentration of 524 μM (0.2 mg/mL) in the nanoemulsion. This concentration was selected based on the literature reported i.v. dose for anticancer studies of celecoxib NPs. Venkatesan *et al.*[46] showed anticancer effect in a mouse xenograft model after administering 100 μg/kg dose of celecoxib-chitosan NPs for three times making the cumulative dose 300 μg/kg Majority of the studies utilized multiple doses of celecoxib formulations. We intended to use a single i.v.

administration in the dose range of 100-200 μL of nanoemulsion per mouse, which corresponds to 800-1600 μg/kg of celecoxib. Although our selected dose is higher than the mentioned cancer study, the cumulative exposure to celecoxib compared to multiple oral doses of celecoxib is significantly less with our formulation. It should be noted that in one of the inflammatory models, rat neuropathic pain, significantly lower dose of celecoxib (~180 μg/kg) in a PFC nanoemulsion showed pharmacological effects (chapter 7). In our preliminary attempts, nanoemulsions prepared with Capmul® showed toxicity in mouse macrophages. Hence, we used Miglyol 810N (or 812N), as a solubilizer for celecoxib. Miglyol 810 N, a medium-chain triglyceride of GRAS (generally regarded as safe) category, is widely used in parenteral nutrition emulsions.[206]

An additional imaging modality was made possible by incorporating lipophilic NIR dye for NIRF imaging. NIRF imaging can be fast, economical and quantitative for preclinical studies. Combination of PFCs with optical imaging provides exceptional advantage over using MRI alone as discussed before. NIRF overcomes potential issues in biodistribution studies that use ^{19}F detection alone *in vivo*, such as lack of access to a high field magnet, sensitivity and cost. The work presented in this chapter was originally published elsewhere.[128]

4.2 Materials and methods

4.2.1 Materials

Celecoxib was purchased from LC Laboratories® (Woburn, MA, USA). Miglyol 810N was generously donated by Sasol (NJ, USA). PFPE (produced by Exfluor Research Corp., Roundrock, TX, USA) was generously provided by Celsense Inc. (Pittsburgh, PA, USA) and used without further purification. CellVue® NIR815 (786 nm/814 nm) and

CellVue® Burgundy (683 nm/707 nm) Fluorescent Cell Linker Kit was purchased from Molecular Targeting Technologies, Inc. (MTTI) (West Chester, PA, USA). Purified mouse anti-mouse CD45.1 monoclonal antibody conjugated to FITC (fluorescein isothiocyanate) used for cell labeling was obtained from BD Pharmingen™. Antifade ProLong® Gold (Invitrogen) was used as the mounting medium. Lysotracker® Green DND-26 and Hoechst 33342 were obtained from Invitrogen. Bacterial lipopolysaccharide (LPS) was obtained from Sigma Aldrich. PGE_2 enzyme-linked immunosorbent assay (ELISA) kit was obtained from Cayman Chemical Company (Ann Arbor, MI, USA). For all other reagents and cell culture conditions, see section 3.2.1.

4.2.2 Preparation and characterization of PFPE nanoemulsions

Preparation

PFPE nanoemulsions were prepared using a mixture of nonionic surfactants, P105 and CrEL. A premade aqueous solution of mixed surfactants was used (section 3.2.3.1). PFPE formulations were prepared to a final volume of 25 mL and the amount of ingredients is shown in Table 4.1. Celecoxib (5 mg) was first dissolved in 0.95 g of Miglyol 810N by overnight stirring while 6 µL of NIRF dye stock solution (1 mM in ethanol) was added before blending with PFPE. PFPE oil (1.81 g) was transferred to a 500 mL round bottomed flask containing celecoxib, NIRF dye and Miglyol 810N and stirred at 1200 rpm, RT for 15 min. To this 11.5 mL (0.575 g of mixed surfactant) of mixed surfactant solution was added and stirred at 1200 rpm for additional 15 min. To this mixture, 11.5 mL of deionized water was added and stirred under ice-cold conditions for 5 min at 1200 rpm. The coarse emulsion was processed (Microfluidics M110S) for 30

pulses under recirculation mode (inlet air pressure ~6 bar) and temperature was noted. Sterile-filtered nanoemulsion samples (1.5 mL) were stored at 4 °C, 25 and 37 °C to assess the stability. The bulk of the nanoemulsion was stored at 4 °C until use. Nanoemulsion without celecoxib and NIRF dye was prepared in the same way to serve as the control. Table 4.1 shows components of all the nanoemulsions (**A**, **B** and **C**) formulated. Nanoemulsions were characterized by DLS measurements, ^{19}F NMR and NIRF imaging.

Table 4.1. Table showing components of PFPE nanoemulsions A, B, and C.

Nanoemulsion Component	**A** mg/mL	**B** mg/mL	**C**[a] mg/mL
Celecoxib	0	0.2	0.2
PFPE	72	72	72
Miglyol 810N	38	38	38
Cremophor® EL	13.8	13.8	13.8
Pluronic® P105	9.2	9.2	9.2
NIRF Dye	µM	µM	µM
Cellvue® NIR815	0	0.24	0
Cellvue® Burgundy	0	0	0.24

[a]Nanoemulsion **C** is used for confocal microscopy of labeled macrophages

Droplet size and zeta potential measurements by DLS

The size and zeta potential distribution of the nanoemulsion droplets in aqueous medium was determined by DLS at 1:40 v/v as mentioned in section 3.2.4. The stability of nanoemulsions incubated (37 ºC, 5% CO_2) in cell culture medium (DMEM with 10% FBS) for 24 h was tested under same conditions.

^{19}F NMR measurements of nanoemulsions

^{19}F NMR was recorded (Bruker, 470 MHz) on nanoemulsions (and dilutions in water) with 0.02% v/v TFA in water solution mixed in 1:1 v/v ratio (200 μL each). ^{19}F NMR peak around -91.5 ppm corresponding to 40 fluorine nuclei was integrated with TFA (set at -76.0 ppm) as reference. Amount of PFPE per mL nanoemulsion was quantified based on the number of ^{19}F under PFPE peak at -91.5 ppm as shown in Equation 3.5.

NIRF imaging of nanoemulsions

NIRF images of the above prepared NMR samples were recorded on an flat bed imaging system (Odyssey® Infrared Imaging System, LI-COR Biosciences, NE, USA). Nanoemulsion **B** loaded with celecoxib and NIRF dye was imaged. The NMR tubes with nanoemulsions were aligned and carefully taped to a paper, placed in the sample compartment and imaged. Images at 785 nm excitation wavelength and emission above 810 nm were collected. Imaging parameters include an intensity setting of 2 and 2.5 mm focus offset. NIRF signal was quantified from the obtained images using the instrument software (Odyssey® Imager v.3). Nanoemulsion **A** was used to correct for the fluorescence background. Images were quantified by drawing region of interest (ROI) around the total area corresponding to the nanoemulsion (with aqueous TFA) in the NMR tube was carefully selected for quantification after setting the nanoemulsion **A** fluorescence as background in the instrument software. Fluorescence is obtained as relative fluorescence units (RFU).

HPLC Method and Validation

A previously reported high performance liquid chromatography (HPLC) method was adapted[43] and required validation parameters such as linearity, accuracy, inter-day precision, limit of detection (LOD) and limit of quantitation (LOQ) were evaluated for celecoxib (Table 4.2) according to ICH Q2 (R1) guidelines.[207] The HPLC method consisted of a Waters Alliance (Waters Corporation, Milford, MA, USA) equipped with a Waters 2690 separation module and Waters 996 Photodiode Array detector. Data was acquired and analyzed by the Empower™ 2 Pro software. Analysis was performed using C18 column (Hypersil Gold C18 150mm X 4.6mm, 5µm pore size) and 75:25 methanol:water as mobile phase with the flow rate of 1 mL/min at ambient temperature. The detection wavelength was 252 nm.

Linearity and Range: The calibration curves were constructed with 6 concentrations ranging from 5 to 0.15 µg/ml. The linearity was evaluated by linear regression analysis using peak areas of celecoxib solutions.

Accuracy and Precision: Accuracy and precision of the assay method was evaluated for both intra-day and inter-day variations at three different concentrations (3.75, 1 and 0.31 µg/mL), different from calibration curve for three days. Accuracy and precision were expressed in terms of percent mean recovery and percent relative standard deviation (% RSD) respectively. Intermediate precision, which refers to inter-assay variations was measured across three days.

Limit of Detection and Quantitation: LOD and LOQ were determined based on the standard deviation (SD) of the response (σ) and slope (S) of the calibration curve obtained from multiple calibration curves. LOD is calculated by 3.3σ/S and LOQ by

$10\sigma/S$, where σ is the SD of the intercept of the calibration curves and S is the mean of slope of the calibration curves.

Drug content in nanoemulsion

The above-mentioned method was used to assess celecoxib content in nanoemulsions. Celecoxib was extracted from nanoemulsion using methanol. This method was slightly modified from the previously published method, which utilized methanol/water (75/25) for celecoxib extraction.[43] Nanoemulsion **B** (250 µL) was dispersed in 10 mL methanol and vigorously vortexed. The mixture was centrifuged at 4000 rpm (Centrifuge 5804 R, 15 amp version) for 10 min. PFPE was separated as a clear oil at the bottom of the tube. Supernatant was collected and analyzed for celecoxib. Analysis was carried out in triplicates. All the formulation ingredients were analyzed separately for possible interference using same chromatographic conditions. The obtained data is reported as percent drug loaded in the nanoemulsion compared to the theoretical concentration.

Cell viability

Cell viability was assessed as outlined in section 3.2.4 with modifications using CellTiter-Glo® luminescence assay. Briefly, mouse macrophages (RAW 264.7) were plated in 96 well plate at 10,000 cells/well. After overnight incubation at 37 °C and 5% CO_2, culture medium was removed and adhered cells were exposed to nanoemulsions **A** and **B** (prediluted in complete medium) at different PFPE concentrations and incubated overnight. 50 µL of the medium was carefully removed and 25 µL of CellTiter-Glo®

analyte was added to each well. The plate was shaken for 20 min at RT to induce cell lysis. 60 µL of the cell lysate was transferred to a white opaque 96 well plate and luminescence was recorded.

Cell uptake

To assess the *in vitro* behavior of the nanoemulsions, cell labeling studies were conducted on mouse macrophages. Cells were cultured in 6 well plates at 0.3 million per well for 48 h. After aspirating the medium, cultured cells were washed with medium and DPBS. Cells were exposed to nanoemulsion **B** (prediluted in medium) with concentration of PFPE ranging from 0.09 to 1.4 mg/mL. 2 mL of nanoemulsion **B** containing medium was added to each well. Cells were incubated for 24 h at 37 °C and 5% CO_2. Cells from all samples were counted using neubauer hemocytometer. ^{19}F NMR sample was prepared as outlined in section 3.2.4.

^{19}F NMR measurements of labeled cells

NMR tubes with the labeled cell lysate (~400 µL) prepared as described above were subjected to ^{19}F NMR analysis to quantify the total fluorine content in the cells. The number of ^{19}F per cell was calculated using Equation 3.6 (section 3.2.4).

NIRF measurements of labeled cells

NMR tubes containing labeled cells, TFA and water were directly imaged on the flat bed imaging system. Briefly, the NMR tubes were aligned and carefully taped to a paper, placed in the sample compartment and imaged. Images at 785 nm excitation

wavelength and emission above 810 nm were collected. Imaging parameters include an intensity setting of 8 and 2.5 mm focus offset. Images were quantified by drawing ROI around the sample to obtain integrated fluorescence intensity. Cells that are not exposed to the nanoemulsion were used for background correction.

Fluorescence microscopy

Images of nanoemulsion labeled mouse macrophages were captured using confocal microscopy (Leica TCS SP2 spectral confocal microscope, Leica Microsystems) to assess the intracellular distribution of the nanoemulsion. Macrophages were cultured for 24 h on glass cover slips (Fisherfinest, 22x22-1) placed in a 6-well plate at a concentration of 10^5 cells per well. Cultured macrophages were exposed to nanoemulsion **C** (21 μL nanoemulsion/mL medium; 2 mL total) for 24 h. After removing 1 mL medium, cells were fixed in 1 mL of 4% paraformaldehyde for 30 min. The medium in the cultured confocal plates (with glass cover slips) was carefully removed and washed with DPBS / 1% FBS. A stock solution of FITC dye conjugated mouse antimouse CD45.1 antibody (CD45-FITC) in DPBS / 1% FBS was prepared at 1 μg/mL concentration. Cells in each well were exposed to 1 mL of the stock solution and left undisturbed at RT. After 15 min, dye solution was removed and washed with DPBS / 1% FBS twice. Each cover slip was transferred to a microscopy slide with antifade mounting medium (ProLong® Gold, Invitrogen). Images were captured on a spectral analyzer confocal microscope by Dr. John A. Pollock. For visualizing FITC, excitation was achieved with the blue Ar laser 488 nm and emission window of 500 nm to 590 nm. Visualizing the Cellvue® Burgundy dye was achieved with the red HeNe 633 nm laser

excitation and emission window of 640 nm to 850 nm. Emission windows were selected in order to avoid spectral overlap between FITC and Cellvue® Burgundy detection. A transmission DIC image was acquired simultaneous to each confocal scan.

To further investigate the presence of droplets in the specific intracellular compartments, lysosomal labeling was performed. Macrophages were seeded on glass bottom confocal plates (P35G-1.0-14-C, MatTek Corporation) for 24 h at a concentration of 0.25 x 10^6 cells per well. Cultured macrophages were exposed to nanoemulsion **C** for 24 h. After aspirating the medium and repeated washings with DPBS, cells were exposed to Lysotracker® Green DND-26 (150 nM). After 1 h incubation, cells were washed and fixed in 4% paraformaldehyde for 30 min. Fixed cells were washed with DPBS / 1% FBS and exposed to Hoechst dye (1 μg/mL) dissolved in DPBS / 1% FBS for 5 min. Cells were washed and stored in DPBS at 4 ºC until imaged. Imaging was performed on Spinning Disk Confocal microscope (Andor Revolution XD) with 60x oil immersion objective (NA 1.49). The emission filters were 447/60 nm band pass filter in the 405 channel (Hoescht 33342), 794/160 nm band pass filter in the 640 channel (Cellvue® Burgundy), and 525-50/600-45/690 nm triple band pass filter in the 488 channel (Lysotracker® Green DND-26).

PGE_2 assay

To investigate the *in vitro* therapeutic efficacy of the drug carrier, effect of nanoemulsions on PGE_2 production by macrophages was assessed. Cells were plated in 6 well plates at 0.3 million cells/well and incubated overnight. Cells were exposed to nanoemulsion **B** at 1.4 mg/mL PFPE concentration (9.28 μM celecoxib), dimethyl

sulfoxide (DMSO), and free drug dissolved in DMSO (9.28 μM). Fresh medium was added to unexposed cells. After overnight incubation, all wells were washed (2x) with medium and DPBS. Bacterial toxin, LPS, at 1 μg/mL diluted in medium (2 mL total) was added to each well with cells (exposed and unexposed) and incubated. Unexposed cells treated with LPS were designated as control and unexposed cells without LPS activation were designated as untreated. After 4 h incubation, supernatant was collected and analyzed using commercially available PGE_2 ELISA kit. Samples were analyzed at two different dilutions (1:5 and 1:10) and two replicates of each dilution were used. Assessment of PGE_2 production in the supernatant and data analysis was performed according to the manufacturer instructions. In a separate experiment, macrophages were exposed to either of the nanoemulsions **A** and **B** at 1.4 mg/mL PFPE concentration. LPS treatment was performed post cell labeling with nanoemulsions **A** or **B** for 3 h. Fresh medium was added to unexposed cells (untreated). PGE_2 production was quantified in the supernatant using PGE_2 ELISA kit. Mean and standard error of mean (SEM) were obtained for each treatment.

Statistical analysis

One-way analysis of variance (ANOVA) with Tukey's multiple comparison test was conducted to evaluate statistical significance between treatments for PGE_2 assay using GraphPad Prism version 4. Statistical significance was defined at $p < 0.05$.

4.3 Results and Discussion

A novel COX-2 inhibiting PFC theranostic nanoemulsion with dual imaging capabilities (NIRF and ^{19}F MR) was prepared to label macrophages upon exposure and

inhibit their COX-2 activity. Each component in this design has a unique role in achieving theranostic potential of the final nanoemulsion. The PFPE nanoemulsion contains three key components: (a) the anti-inflammatory drug celecoxib (b) an NIRF dye for fluorescence imaging and (c) PFPE to quantitatively image deep tissues using ^{19}F MRI. The design included a combination of two imaging agents for future utilization of a wide array of techniques such as fluorescence microscopy and imaging, flow cytometry, ^{19}F NMR and MRI to characterize the formulation and achieve complementary information about *in vitro* and *in vivo* performance. Commercially available lipophilic dyes fluorescing in the NIR region, CellVue® NIR815 (excitation maximum (Ex) =786 nm, emission max (Em) = 814 nm) or Burgundy (Ex = 683 nm, Em = 707 nm), were selected.

A proposed nanoemulsion droplet structure schematic is shown in Figure 4.1. The schematic shows PFPE core of the droplet surrounded by HC oil corona and stabilized by surfactants (outermost layer) in the aqueous medium. It is known that PFCs show greater hydrophobicity than lipophobicity, which suggests they would have lower affinity for mixing with water than oils.[142,143] Furthermore, in fluorous phase chemistry literature, it was demonstrated that fluorocarbons can form a distinct liquid phase when mixed with water and organic solvents.[208] Based on these chemical properties of PFCs, PFPE was hypothesized to be in the core of the droplet (Figure 4.1). Recent study by Zarzar *et al.*[209] showed that emulsions containing mixtures of pure PFC (perfluorohexane) and a non-fluorinated HC (hexane) in aqueous medium displayed droplet structure dependent on the type of surfactant utilized. Similar to our proposed droplet structure (Figure 4.1), this study demonstrated that perfluorohexane forms core of the emulsion droplet, while

hexane forms the corona, when hydrocarbon surfactant, sodium dodecyl sulfate, was used. As a result of the preferentially reduced interfacial tension between hydrocarbon and aqueous surfactant solution, the authors conclude that perfluorohexane resides in the core of the droplet.[209] Furthermore, the reported interfacial tensions of fully fluorinated PFCs with aqueous surfactant solutions are higher (~17-20 mN/m)[190] compared to interfacial tension between PFC and HC oil (7 mN/m).[210] Based on the superhydrophobicity of PFCs and low interfacial tensions with HC oil, fully fluorinated PFPE is expected to preferentially segregate in the core of the droplet to avoid less favorable interaction with aqueous environment.

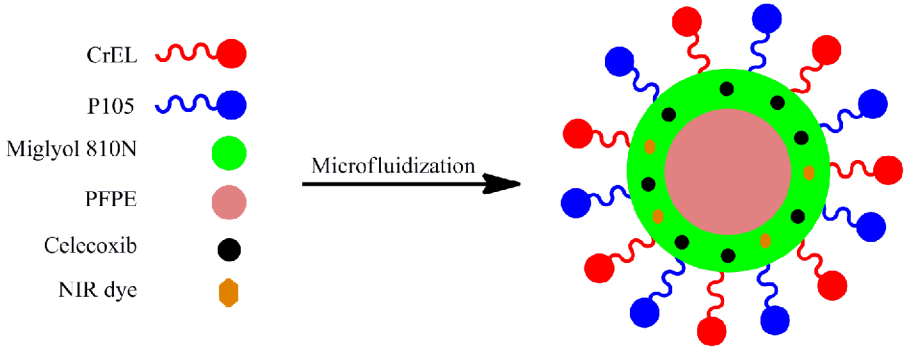

Figure 4.1. Proposed schematic of PFPE nanoemulsion droplet structure.[128]

The challenging task of stabilizing immiscible hydrocarbon oil (Miglyol 810N) and PFPE was achieved by using a combination of CrEL and P105 under high shear. CrEL is a polyethoxylated lipid produced by reacting castor oil and ethylene oxide in 1:35 molar.[211] It is used in pharmaceutical preparations as solubilizer for hydrophobic drugs and emulsifying agent.[211] It is important to rationalize the use of CrEL in this formulation, because of the studies showing associated toxicity. CrEL is associated with hypersensitivity reactions, hyperlipidemia, abnormal lipoprotein patterns, aggregation of

erythrocytes and peripheral neuropathy, which were observed with paclitaxel formulation, Taxol.[211] The amount of CrEL in Taxol is as high as 26 mL per administration, with each mL of formulation containing 527 mg of CrEL.[211,212] Paclitaxel formulations with reduced amount of CrEL showed significantly decreased allergic reactions suggesting that CrEL related toxicity is dose dependent.[213,214] The formulation reported in this work used only 13.8 mg of CrEL per mL emulsion, which is significantly lower (~ 38 fold less compared to Taxol). Based on these calculations and prior reports,[213,214] we expect that allergic reactions are unlikely with the PFPE formulations reported here.

Nanoemulsion preparation and characterization

Nanoemulsions with and without drug/dye (**B**, **C** and **A** respectively) are shown in Table 4.1. Nanoemulsion **A** acts as a drug and dye free control for nanoemulsion **B**; nanoemulsion **C** (containing Cellvue® Burgundy) was formulated to obtain confocal images of labeled cells due to the unavailability of confocal excitation laser for Cellvue® NIR815. During processing, use of organic solvents and thin film emulsification method was avoided as residual solvents in the final formulation could lead to cell toxicity in test cultures. DLS measurements showed an average initial droplet size and PDI less than 150 nm and < 0.15 respectively for nanoemulsions **A**, **B** and **C**, similar to C8-PFTE formulation reported in chapter 3. A representative size distribution graph in Figure 4.2A shows monomodal size distribution. Small droplet size helps end-process sterilization by filtration[214], which is needed for future *in vivo* experiments. Shelf life was determined by following the droplet size and PDI upon storage at 4, 25 and 37 °C (Figure 4.2B). The

inclusion of drug and dye in the nanoemulsion had no appreciable effect on droplet size changes over time upon storage at 4 °C (Figure 4.2). Nanoemulsions **A** and **B** displayed good stability at 4 °C, with mean droplet size and PDI below 160 nm and 0.15 respectively. However, samples stored at 25 and 37 °C showed temperature-dependent increase in size (Figure 4.2C-D). Increase in storage temperature increases the rate of oil diffusion from the droplets and rate of droplet collisions, which increases the droplet size. Therefore, the nanoemulsions are recommended to be stored at 4 °C. Nanoemulsions **A** and **B**, sterically stabilized by nonionic surfactants, showed a moderate zeta potential value around -17±6 mV.

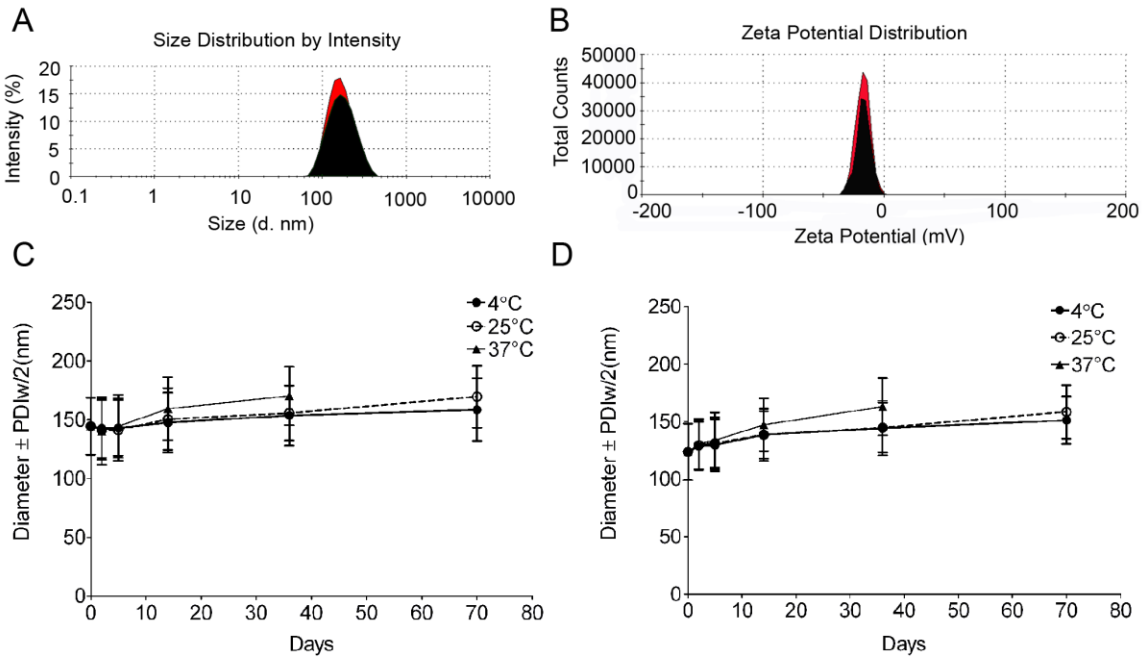

Figure 4.2. Characterization of nanoemulsions A and B using DLS.

A. Representative size and **B.** zeta potential distribution of nanoemulsions **A** (black) and **B** (red). **C.** Droplet size changes with days for nanoemulsion **A** and **D.** Nanoemulsion **B**. Error bars represent PDIw/2.[128]

Reverse phase HPLC was utilized to evaluate drug loading in nanoemulsion **B**. All the formulation ingredients were individually run for any possible interference with the celecoxib peak. Excipients did not show UV absorbance around 252 nm. A representative chromatogram of the nanoemulsion sample is shown in Figure 4.3. Predicted celecoxib concentration based on calibration model was found to be 139.3±8.7 µg/mL nanoemulsion. The validation data is shown in Table 4.2.

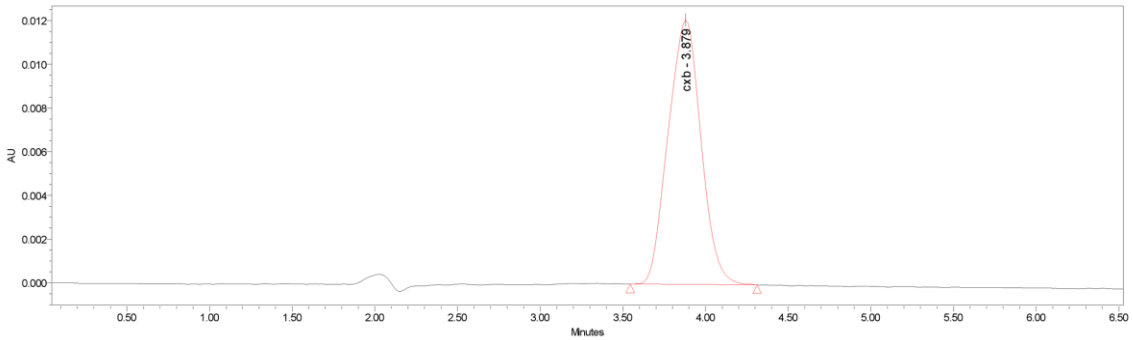

Figure 4.3. Representative chromatogram of celecoxib from extracted nanoemulsion sample.

Table 4.2. Compilation of assessed HPLC method parameters.

	Parameters	**Result**	**Criteria**
Linearity (0.15-5 µg/mL)	R^2 of regression analysis (peak area vs. concentration)	> 0.999	> 0.99
LOD	Calibration curves	45.7 ng/mL	
LOQ	Calibration curves	138.5 ng/mL	
Accuracy at 3 levels (n=3/level)	Recovery	100.2-101.1%	95-105%
Intermediate precision (inter-day)	Overall %RSD	3.8%	<5%

Nanoemulsions were further characterized by ^{19}F NMR and NIRF imaging. A representative ^{19}F NMR peak and NIRF image of nanoemulsion **B** is shown in Figure 4.4A. A linear relationship was obtained for fluorine nuclei and NIRF signal for the dilution series (Figure 4.4B). Based on this result, we believe that the NIRF imaging can be used to assess the concentration-uptake relationship in cells without the need for ^{19}F NMR. For absolute quantification, ^{19}F NMR is preferred due to the absence of background. In summary, DLS results confirm the formation of nanoemulsion with stable droplet size. ^{19}F NMR and NIRF imaging clearly showed the incorporation of PFPE and NIRF dye in the nanoemulsion. HPLC analysis quantified the drug content in nanoemulsion **B**.

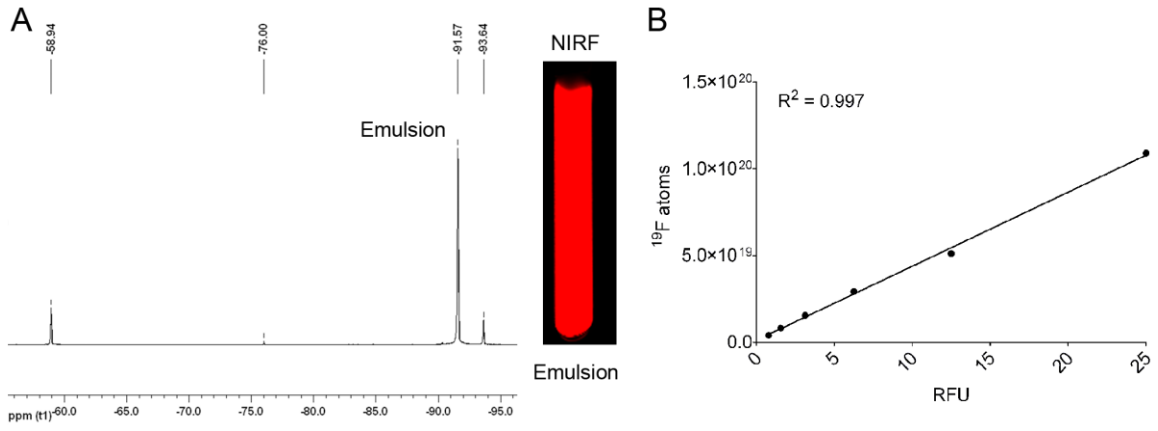

Figure 4.4. Characterization of nanoemulsion B for imaging functionalities.

A. Representative ^{19}F NMR spectrum and NIRF image of diluted nanoemulsion. **B.** Linear relationship between ^{19}F atoms and RFU quantified in serial dilutions of nanoemulsion in TFA containing media.[128]

In vitro toxicity and uptake studies in macrophages

Before performing *in vitro* biological tests, colloidal stability of nanoemulsions in cell culture medium was evaluated by monitoring changes in droplet size. No considerable change in droplet size and PDI was noted under cell culture relevant conditions (Table 4.3). This is crucial as any structural changes in the nanodroplets during incubation with cells could give misleading results on the nanodroplet cellular uptake and toxicity profile, which would further render the nanoemulsions unsuitable for *in vivo* testing. As shown in Figure 4.5, no considerable effect on cell viability was detected after 24 h exposure to nanoemulsions. Cell viability was between 92-104% of the control group (untreated cells).

Table 4.3. Average droplet diameter and PDI of nanoemulsions A and B before and after incubation in media.

Media incubation	Nanoemulsion **A**		Nanoemulsion **B**	
	Average diameter (nm)	PDI	Average diameter (nm)	PDI
Before	144.6	0.11	123.8	0.15
After	140.6	0.13	128.7	0.14

Utilizing ^{19}F NMR and NIRF imaging, cellular uptake of nanoemulsion **B** was characterized. Representative ^{19}F NMR and NIRF image of labeled cells is shown in Figure 4.6A. PFPE line shape and peak position at -91.5 ppm was unchanged upon uptake in cells when compared with PFPE in nanoemulsion **B** (Figure 4.4A). This result suggests the chemical stability of PFPE in cells, which is crucial for their use as an imaging tracer. Both ^{19}F NMR and NIRF measurements of labeled cells showed a concentration-dependent increase in uptake of the nanoemulsion (Figure 4.6B).[215] Since

macrophages can internalize colloidal formulations through receptor-mediated endocytosis, concentration-dependent saturation of uptake is expected. To facilitate comparison between ^{19}F NMR and NIRF, uptake vs. concentration data was fitted with a one-site binding saturation model. This model is appropriate for NP uptake occurring through receptors as the receptors get saturated at high concentration of nanoemulsion, thus leading to saturation of uptake. The amount of nanoemulsion internalized is proportional to the amount bound to the receptor. It should be noted that NP uptake is triggered due to the binding of several receptors leading to receptor clustering and endocytosis. To apply a one-site binding model, a set of receptors bound by NP can be assumed as a single receptor. According to the one-site binding saturation model, the amount of internalized nanoemulsion (Y) is given by:

$$Y = \frac{Y_{max} * X}{K_m + X} \qquad \text{Equation 4.1}$$

where, Y is uptake (^{19}F or RFU normalized to cell number), Y_{max} is the maximum uptake, X is the concentration of PFPE, K_m is the concentration of PFPE required to obtain half-maximum uptake ($Y_{max/2}$).

The uptake-concentration relationship obtained with ^{19}F NMR and NIRF methods showed good fitting to this model ($R^2 > 0.98$) as shown in Figure 4.6C-D. The x-axis of these graphs is shown as amount of PFPE, which is proportional to the amount of emulsion. K_m obtained from this model was very similar for ^{19}F NMR and NIRF data (2.6 vs. 2.7 mg/mL PFPE) as shown in Figure 4.6C-D. This result indicates that NIRF and ^{19}F NMR can be used interchangeably to assess uptake, thus supporting the use of complementary imaging methods for data validation. Interestingly, good correlation was obtained without chemically conjugating PFPE and fluorescent dye as reported earlier.[170]

Based on these results, it can be postulated that the nanoemulsion was not destabilized before entering the cell in the labeling medium. Any instability of nanoemulsion would lead to poor or no correlation between ^{19}F NMR and NIRF signals due to the differences in uptake of imaging agents. A strong correlation between the two imaging agents is a requisite to utilize the nanoemulsion for *in vitro* and *in vivo* dual mode imaging studies.

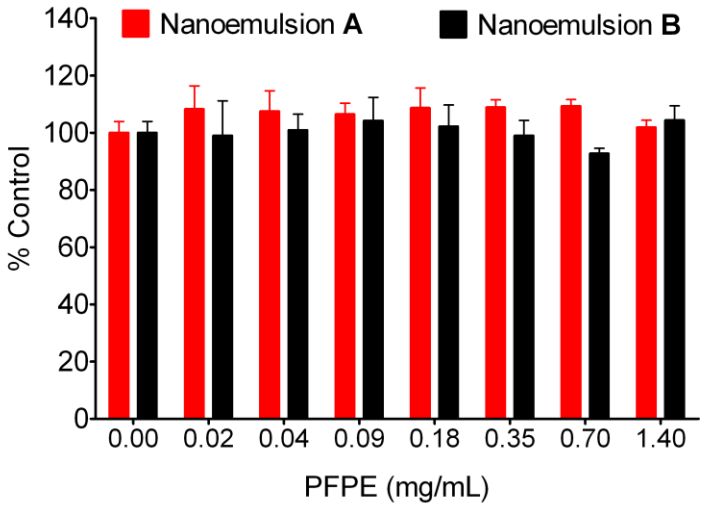

Figure 4.5. Macrophage cell viability post 24-hour exposure to nanoemulsions A and B.

Each data point represent mean of at least three replicates and the error bars are SD of the mean. Values are reported as percent control (0 mg/mL PFPE).[128]

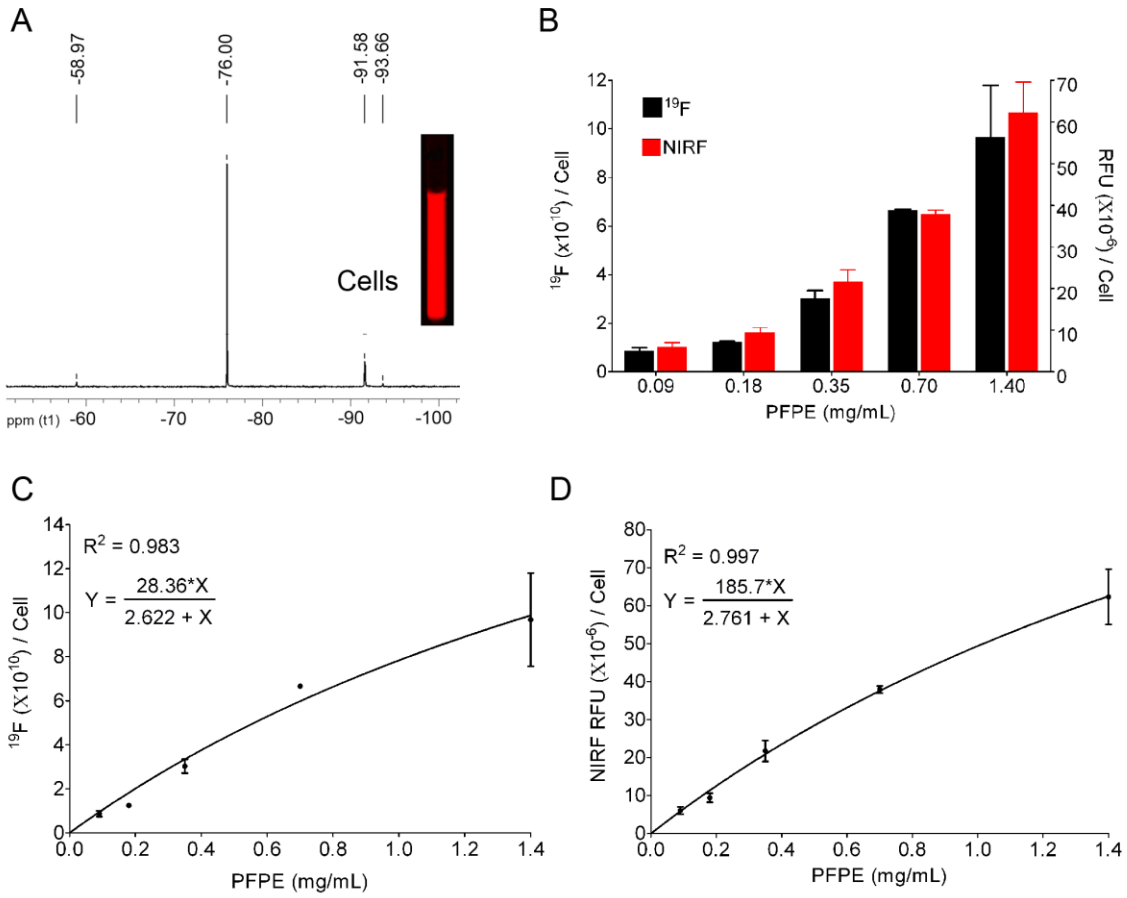

Figure 4.6. Characterization of cellular uptake of nanoemulsion B.

A. Representative ^{19}F NMR of cells labeled with nanoemulsion **B**. TFA reference peak is set at −76.0 ppm. NIRF image of cells labeled with nanoemulsion **B** in NMR tube. **B.** Dose-dependent increase in cell uptake demonstrated by ^{19}F NMR and NIRF (n=2). **C** and **D.** Cellular uptake from panel B fitted to a one-site binding saturation model.[128]

Presented nanoemulsions have lower amount (7.2% w/v) of PFPE than earlier reported cell tracking formulations.[169] However, we found that at a very low PFPE concentration of only 1.4 mg/mL, significant cell uptake (1.0 x 10^{11} fluorine atoms per cell) is achieved. With this labeling efficiency, approximately 7.5 x 10^5 cells per voxel are required to obtain *in vivo* ^{19}F MR images at 11.7 T.[151,163] These findings suggest that this formulation platform could be utilized for cell tracking of *ex vivo* labeled cells. The

utility of this nanoemulsion to detect *in situ* labeled macrophages would require further investigation because the detection sensitivity also depends on the severity of inflammation, extent of macrophage infiltration and injection volume (discussed in chapter 5).

Although ^{19}F NMR and NIRF imaging of the nanoemulsion labeled cells showed dose-dependent cell labeling, conclusions about membrane-adsorbed versus internalized nanodroplets cannot be made from this data alone. Therefore, fluorescence confocal microscopy was performed on macrophages exposed to nanoemulsion. To more closely match the excitation and emission capabilities of the confocal microscope system, an alternate drug loaded nanoemulsion (nanoemulsion **C**, Table 4.1) was prepared with Cellvue® Burgundy dye (683 nm / 707 nm). Cells exposed to nanoemulsion **C** were stained with anti-CD45.1 antibody conjugated with FITC dye (CD45-FITC) to visualize cell membrane. CD45 is a protein tyrosine phosphatase, receptor type C cell membrane associated protein. The nanoemulsion uptake was visualized by Cellvue® Burgundy dye.

Figure 4.7 clearly shows the presence of the CD45 protein (green) and the Cellvue® Burgundy labeled nanodroplets (red) in the cytoplasm. As a control, cells not exposed to nanoemulsion were labeled with CD45-FITC. No evidence of NIRF signal was observed in the control group. The presence of nanoemulsion as distinct entities, which is also evident in the transmitted DIC view of the cells (Figure 4.8A), indicates their presence in endosome-like compartments. Simultaneous presence of CD45 protein and nanoemulsion droplets (green and red fluorescent signals) further supports the speculation that nanodroplets are present in the endocytic compartments. CD45 internalization has been previously reported.[216] Three-dimensional view of the cell

revealed that the nanodroplets are within the cytoplasm, specifically in the maximum projection cross-sectional view of the cell (Figure 4.8B). In a separate experiment, presence of nanoemulsion droplets in the intracellular compartments was assessed by labeling acidic endosomal/lysosomal compartments with Lysotracker® Green. It appears that nanoemulsion droplets are distributed in the entire volume of the cytoplasm and no preferential accumulation in the lysosomes was observed after 24 h (Figure 4.8C).

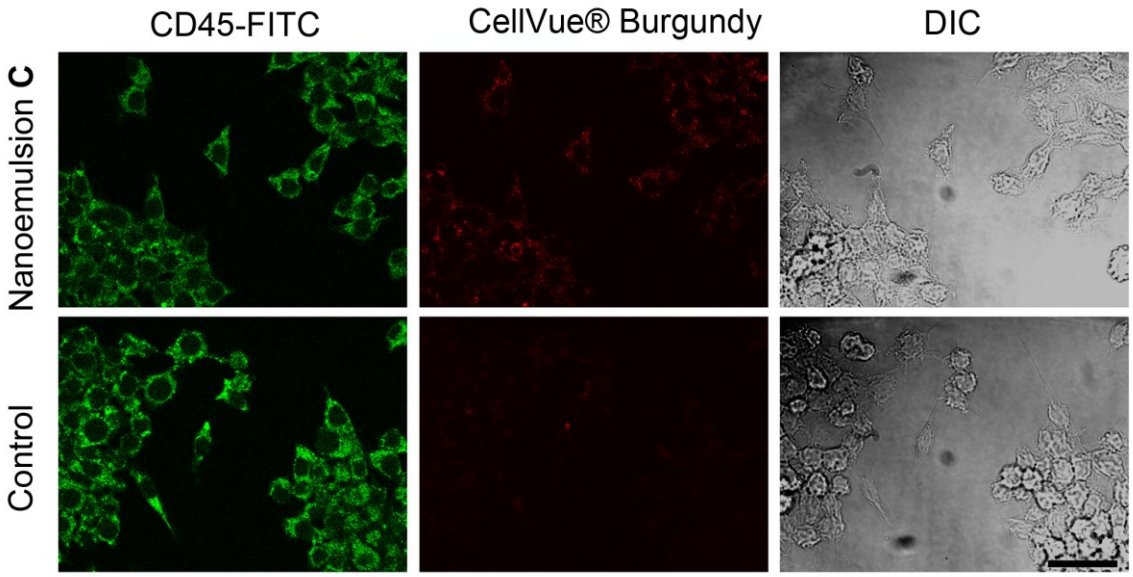

Figure 4.7. Confocal microscopy of macrophages exposed to nanoemulsion C.

A. Cells labeled with anti-CD45 (FITC) green and incorporated nanoemulsion **C** containing celecoxib and Cellvue® Burgundy dye represented as red. Cells not exposed to the nanoemulsion **C** exhibit CD45 labeling with FITC (green) but no red signal. Transmitted light DIC image acquired simultaneously shows field of view (Bar = 30 μm). Image by Dr. John A. Pollock, 2013.[128]

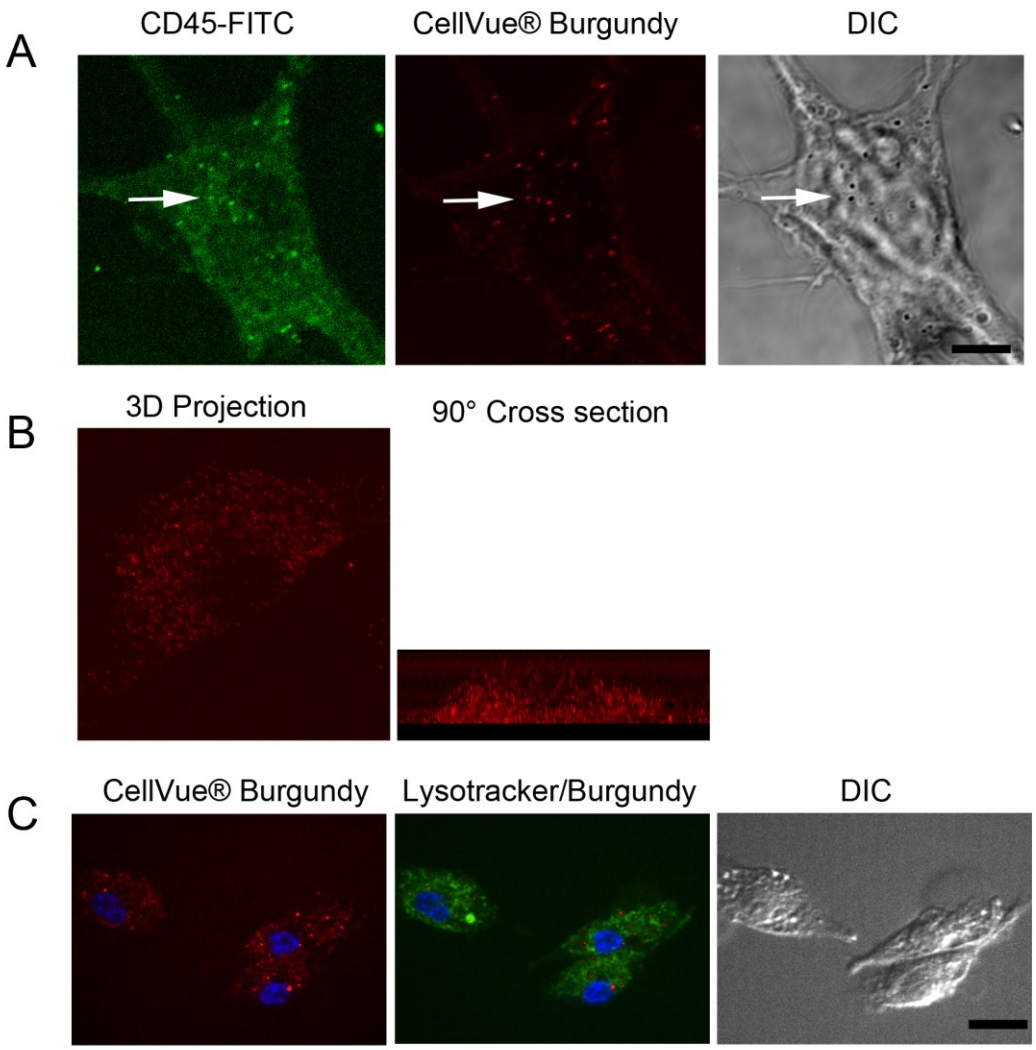

Figure 4.8. Confocal microscopy to assess intracellular localization of nanoemulsion C.

A. Cells labeled with CD45-FITC (green) and incorporated nanoemulsion **C** containing Cellvue® Burgundy dye exhibit broad expression of CD45 as well as concentrated fluorescent signal coincident with Cellvue® Burgundy, indicating internalization of CD45 protein and nanoemulsion **C**. The transmitted light DIC view of the cell reveals the black refractive droplets, coincident with the red and green fluorescent signals (Bar = 5 μm). **B.** A single cell imaged in serial section and rendered by maximum-projection to represent all of the Cellvue® Burgundy labeled droplets viewed from above and 90° cross-section, to reveal that the droplets are distributed throughout the cell cytoplasm. **C.** Cells showing concentrated red fluorescence from nanoemulsion **C**, not clearly localized with acidic compartment label, Lysotracker® Green DND-26. Nucleus labeled with Hoechst dye is shown in blue (Bar = 5 μm). Panels A and B images by Dr. John A. Pollock, 2013.[128]

COX-2 inhibition in macrophages

The potential anti-inflammatory effect of celecoxib-loaded nanoemulsion **B** on the production of PGE_2 by LPS activated macrophages was studied (Figure 4.9A). LPS activated cells showed significant increase ($p < 0.001$) in PGE_2 as compared to untreated. A statistically significant difference ($p < 0.001$) between nanoemulsion **B** and LPS treated control was observed. Cells labeled with nanoemulsion **B** produced, on average, 50.6±8.2 pg of PGE_2 per mL as compared to 504.5±41.2 pg/mL by LPS activated control. Exposing LPS activated macrophages to DMSO (vehicle for free drug) has not shown any effect on PGE_2 production compared to control. Although, PGE_2 reduction by nanoemulsion **B** is not statistically different from free drug, nanoemulsion mediated celecoxib delivery may be advantageous in reducing systemic exposure to the drug and related side effects. Additionally, dual mode imaging capabilities allow for non-invasive imaging of nanoemulsion biodistribution. In a separate experiment, effect of nanoemulsions **A** and **B** on PGE_2 production was studied (Figure 4.9B). Nanoemulsion **B** showed significant reduction in PGE_2 production compared to nanoemulsion **A** and control (Figure 4.9B). Nanoemulsion **A** has not shown any significant contribution to changes in PGE_2 levels proving that the drug free vehicle is inert towards PGE_2 production. These results clearly demonstrate that the presented theranostic PFPE nanoemulsion is internalized by macrophages and act to inhibit COX-2 through celecoxib delivery.

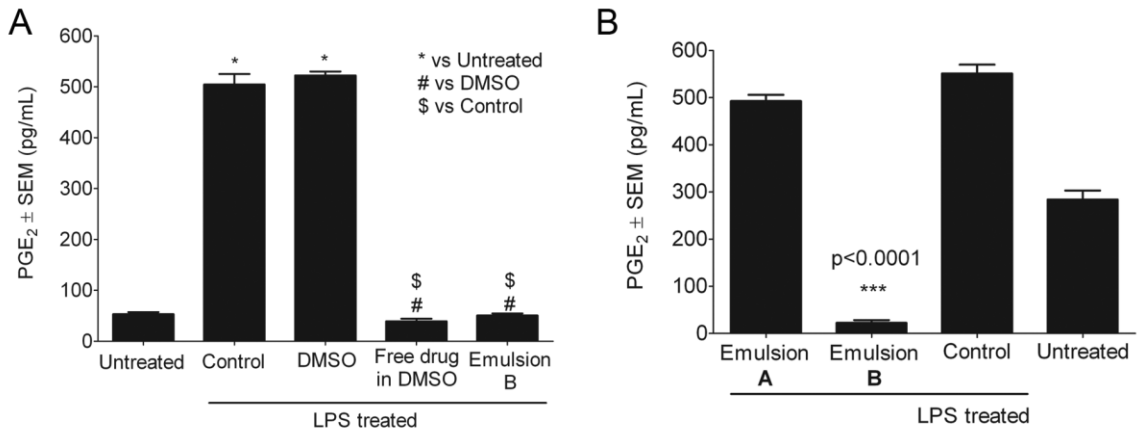

Figure 4.9. Effect of nanoemulsion-mediated celecoxib delivery on PGE_2 production by LPS activated macrophages.

A. PGE_2 produced by LPS-activated macrophages exposed to nanoemulsion **B**, free drug dissolved in DMSO and DMSO. Cells not exposed to LPS were designated as untreated. * # $ represent statistical significance comparisons ($p < 0.001$) between treatments. **B.** Separate experiment comparing nanoemulsion **A** and **B**. Each data point represents the mean ± SEM of at least four independent measurements.[128]

4.4 Conclusion

In this chapter, a novel celecoxib carrying nanoemulsion formulation equipped with dual mode imaging capabilities is prepared and characterized. The prepared nanoemulsions showed good stability for 70 days. Correlation of dose-dependent cellular uptake between NIRF and ^{19}F NMR signals showed the complementary nature of dual mode imaging functionality. ^{19}F NMR, NIRF imaging and confocal fluorescence microscopy evidently demonstrated the uptake of nanoemulsion droplets by macrophages. Nanoemulsion delivery of celecoxib is established in macrophages by their inhibitory effect on PGE_2 production. Before *in vivo* studies ensued, a modified nanoemulsion incorporating additional fluorescent dye was prepared, which is described in chapter 5.

5 Dual fluorescent PFPE nanoemulsions for improved optical imaging capabilities

5.1 Introduction

In this chapter, we addressed a common problem associated with standard epifluorescent microscopy methods for cell and tissue imaging, which use excitation lasers and filters that do not alternately support NIRF dye detection. In chapter 4, we found that in a cellular imaging experiment, full excitation of the NIRF dye by a standard 633 nm laser is difficult to achieve, which led to low fluorescent signal from labeled cells and possibly in future histology samples. Commonly used epifluorescent microscopes lack the optics required for NIRF imaging. To overcome the problem, a lower wavelength dye (e.g. Cellvue® Burgundy) was introduced to the system in order to match the optical properties of available fluorescence instruments. Although lower wavelength dyes are advantageous for experiments involving tissues and cells, NIRF dyes are required for *in vivo* imaging to obtain images with reduced background fluorescence. Therefore, in some reports, two dyes are introduced in the formulation to facilitate *in vivo* imaging as well as *ex vivo* histology and flow cytometry.[171] However, the presence of two dyes in the same environment has higher chance for chemical and optical interaction. To avoid these issues, the PFPE nanoemulsion (chapter 4) was modified with distinct fluorescent reporters with non-overlapping fluorescence spectra, introduced into distinct oil phases of the PFC nanoemulsion. Having each oil phase separately labeled by a fluorescent dye allows for improved correlation between *in vivo* imaging and histological data. Dual fluorescent labeling can improve intracellular

tracking of the nanodroplets and it can be used to assess nanoemulsion integrity in cells and tissues. Furthermore, long-term stability of NIRF dye in biological samples can be deduced by comparing the stability with lower wavelength dye. The *in vivo* imaging potential of the nanoemulsion is discussed at the end of the chapter. Development and *in vitro* characterization shown in this chapter was originally published elsewhere.[217]

5.2 Materials and methods

5.2.1 Materials

Cy3-PFPE conjugate was synthesized by Michael J. Patrick at Carnegie Mellon University per Patrick, and Janjic *et al.*[218] and Janjic *et al.*[170] synthetic methods, and used without further purification. DiR (1,1'-Dioctadecyl-3,3,3',3'-Tetramethylindotricarbocyanine Iodide) lipophilic tracer was purchased from Invitrogen and used without further purification. RAW 264.7 cells were cultured similar to section 3.2.1. Fluorescence measurements were performed on Tecan Safire2 fluorescence plate reader at Carnegie Mellon University.

5.2.2 Preparation and characterization of dual fluorescent nanoemulsions

Nanoemulsion preparation

Nanoemulsions were prepared at 25 mL scale following the method described in section 4.2.2. with some modifications. PFPE oxide (0.98 mL) and Cy3-PFPE (0.02 mL) were blended by vortex mixing in a 50 mL eppendorf tube. A mixture of 1 mL Miglyol 810N and 100 μL of 5 mM DiR dye in absolute ethanol (20 μM) was added to the Cy3-PFPE/PFPE mixture and vortex mixed. The remaining procedure is same as described in section 4.2.2. For stability studies, samples were stored at 4 °C. To prepare drug-

containing nanoemulsion, 5 mg celecoxib was dissolved in 1 mL of Miglyol 810N by overnight stirring and the nanoemulsion prepared following above procedure.

Nanoemulsion characterization

Nanoemulsions were characterized for droplet size, PDI, zeta potential, NIR imaging on a LiCOR Odyssey® imager at an 800 nm emission wavelength, ^{19}F NMR and ^{19}F content determination as noted in sections 3.2.1 and 4.2.2. Fluorescence measurements (by Michael Patrick) were performed on Tecan plate reader using a 10 nm bandwidth. Nanoemulsions were diluted 20 µL into 480 µL (4% v/v) of de-ionized water, and 150 µL of diluted sample was measured. Excitation spectra were obtained with an emission wavelength of 590 nm for Cy3 and 790 nm for DiR. The excitation wavelengths were scanned with a 2 nm step from 400 nm to 570 nm for Cy3 and 400 nm to 770 nm for DiR. Emission spectra were obtained with an excitation wavelength of 530 nm for Cy3 and 730nm for DiR, and emission wavelengths were scanned with a 2 nm step from 550 nm to 850 nm for Cy3 and 750 nm to 780 nm for DiR. Fluorescence signal stability measurements were determined by fluorescence synchronous scan (excitation 500 to 830 nm, with emission at a 20 nm offset and 4 nm step) using samples prepared as above in duplicate. Detector gain setting was automatically calculated by the instrument for the first time point and the same value kept for follow-up measurements. Correlation of fluorescence signals with nanoemulsion concentration was determined by preparing serial dilutions of nanoemulsion in deionized water and using 100 µL of sample in triplicate for fixed Ex/Em wavelength measurements at 544/564 nm (Cy3) and 748/768 nm (DiR).

Confocal microscopy

To visualize the cellular uptake of nanoemulsion, confocal microscopy was recorded for nanoemulsion-labeled macrophages (RAW 264.7). Briefly, 0.1 million macrophages were seeded in 6-well plate on a coverslip and incubated at 5% CO_2 and 37 °C. After 48 h, medium was aspirated, and cells washed with DPBS. Macrophages were exposed to nanoemulsion containing medium at 1.4 mg/mL concentration of PFPE. Dye-free nanoemulsion was used as a control, and macrophages that were not exposed to nanoemulsions were treated as negative control. Cover slips were transferred to glass slides and mounted with Prolong Gold. Dr. John A. Pollock performed confocal imaging. Imaging was achieved with 543 nm excitation and emission detection from 550-625 nm on a Leica SP2 spectral confocal for the detection of the Cy3 dye. DiR was detected with 633 nm excitation and emission detection from 650-850 nm, with simultaneous acquisition of transmitted DIC images of the cells. Multicolor merge was achieved with Leica image software version 2.3 and the image contrast/brightness was adjusted in Adobe® Photoshop CS6.

5.3 Results and discussion

PFC nanoemulsions have been labeled by fluorescent dyes before, either by introducing the fluorescent dye into the surfactant layer[160] or the fluorocarbon core of the PFC nanodroplet.[170] In the present PFC nanoemulsion, two fluorescent dyes are introduced, a cyanine dye (Cy3)[219] and a NIRF carbocyanine dye (DiR) into two distinct oil phases of the nanoemulsion. Cy3 is conjugated directly to PFPE and DiR was added to the Miglyol oil. Fluorescent dye conjugated to the PFPE chain is expected to remain entrapped in the PFPE core of the nanoemulsion droplet, following typical fluorous phase

colloidal behavior.[152,170] The Miglyol oil phase carries the NIRF tracer (DiR) and celecoxib, while the PFPE phase carries the Cy3-PFPE.

5.3.1 Colloidal and imaging characterization of dual fluorescent nanoemulsions

The present nanoemulsion is designed to serve two roles: the carrier of COX-2 inhibitors to macrophages, and a triple-imaging agent for fluorescent *in vitro* imaging of labeled cells and tissues, *in vivo* NIRF and ^{19}F MR imaging. Figure 5.1 shows the colloidal stability of the dual fluorescent nanoemulsion. The presence of celecoxib did not significantly affect the droplet size, PDI, and zeta potential of the nanoemulsion. Average droplet size was around 175 nm and PDI was 0.2. The zeta potential was negative (-43 ± 7.4 mV). Compared to the nanoemulsion reported in chapter 4, a larger zeta potential value was observed, possibly due to the presence of multiple fluorescent dyes in this complex system. Nanoemulsions stored at 4 °C and followed for at least 45 days showed no significant change in droplet size or PDI during that period (Figure 5.1).

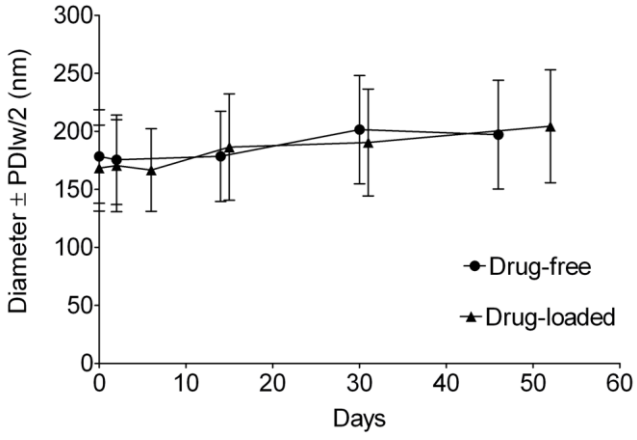

Figure 5.1. Droplet size changes with days of dual fluorescent nanoemulsions stored at 4 ° C. Originally published elsewhere. [217]

Fluorescence measurements were conducted to evaluate the stability of the two fluorescent dyes present in the nanoemulsion. Our goal was to assure that the entire formulation remains stable over time, including all three imaging modalities, to assure reproducibility of *in vivo* studies. Nanoemulsions with and without the drug were stored at three different temperatures, 4 °C, RT and 37 °C. Storage at higher temperatures (RT and 37 °C) led to loss of DiR fluorescence, Figure 5.2A (top). Figure 5.2A (bottom) shows visual color differences in representative nanoemulsion samples stored at the three different temperatures, indicating changes in the incorporated dyes. Synchronous excitation and emission scan measurements confirmed the presence of Cy3-PFPE, revealed some DiR conversion into a lower wavelength emitting product, DiI-(5) (peak around 650 nm). However, Figure 5.2C-D shows retention of normal spectral behavior of both dyes when incorporated into the nanoemulsion. Ex and Em of the dyes in the nanoemulsion are 552 nm and 564 nm for Cy3, and 750 nm and 768 nm for DiR. Fluorescence measurements show that nanoemulsions stored at 4 °C retained fluorescence signals for both Cy3 and DiR dyes. Fluorescent signals of Cy3-PFPE barely decreased (4%) upon storage for 49 days at 4 °C. Whereas, DiR showed a reduced fluorescence of 23% compared to day 0. Most NIRF dyes have stability issues.[220] For example, indocyanine green and cyanine 5 dyes have shown to undergo photobleaching and degradation mechanisms leading to reduced fluorescence intensity.[221,222] Therefore, presence of highly stable Cy3 can be advantageous for histological assessments, where a tissue undergoes several processing steps, which might degrade the labile NIRF dyes. It should be noted that NIRF dye is indispensible in the formulation in order to reduce

interference from autofluorescence in *in vivo* imaging. This combination is therefore an improvement to our nanoemulsion reported in chapter 4.

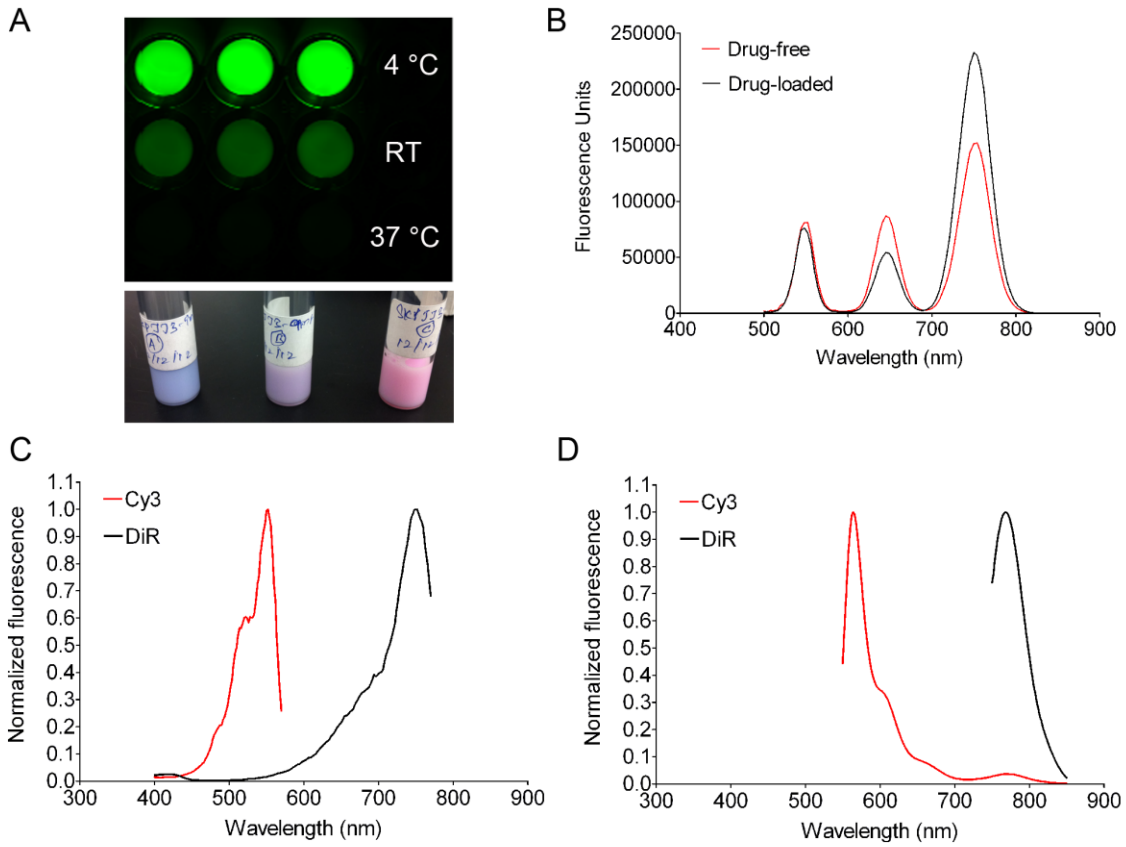

Figure 5.2. Optical assessment of dual fluorescent PFPE nanoemulsions.

A. NIR fluorescence image of nanoemulsions stored at different temperatures taken at 800 nm emission using Li-COR Odyssey® NIR imager (top). Representative photo of the nanoemulsion samples stored at 4 °C, RT and 37 °C (left to right) showing changes in color resulting from DiR changes. **B.** Synchronous excitation / emission scan of Cy3 and DiR in nanoemulsions with and without the drug. **C.** Excitation and **D.** Emission spectra showing both dyes in the nanoemulsion (fluorescence measurements by Michael J. Patrick, CMU, 2013).[217]

In this study, optical and ^{19}F MR properties of dual fluorescent theranostic nanoemulsions were evaluated *in vitro*. In order to use fluorescence and ^{19}F MRI as

complementary imaging techniques, a linear correlation between imaging signals and nanoemulsion concentration is expected. As shown in Figure 5.3, we observed a linear relationship between nanoemulsion concentration and ^{19}F atoms, DiR, and Cy3 fluorescence signal intensities. Lack of this relationship would potentially render the theranostics inflexible, in utilizing the imaging techniques interchangeably.

Similar to the results from chapter 4, confocal microscopy showed the presence of nanoemulsion droplets in the cytoplasm of macrophages (Figure 5.4) as distinct entities. In the transmitted light (DIC) image (Figure 5.4A bottom row), macrophages labeled with emulsions showed granularity in the cytoplasm, compared to untreated macrophages (no emulsion), confirming the uptake of nanoemulsion droplets. Macrophages with dye-free nanoemulsion did not show fluorescence, although granularity was observed in the DIC image (Figure 5.4A middle). Macrophages labeled with the dual fluorescent nanoemulsion showed fluorescence corresponding to DiR and Cy3 dyes (Figure 5.4A right column). Interestingly, a merged image showed that Cy3 and DiR signals are mostly co-incident indicating their co-presence (Figure 5.4B) in the endocytic compartments and probably in the nanoemulsion droplets. This image cannot conclusively prove that Cy3-PFPE and DiR are present in the nanodroplet together due to the resolution and instrument sensitivity issues to detect < 200 nm droplets. However, a qualitative assessment regarding the co-presence of both dyes from PFPE and HC phases in the nanoemulsion droplets indicate the integrity of nanoemulsion droplets during cell labeling.

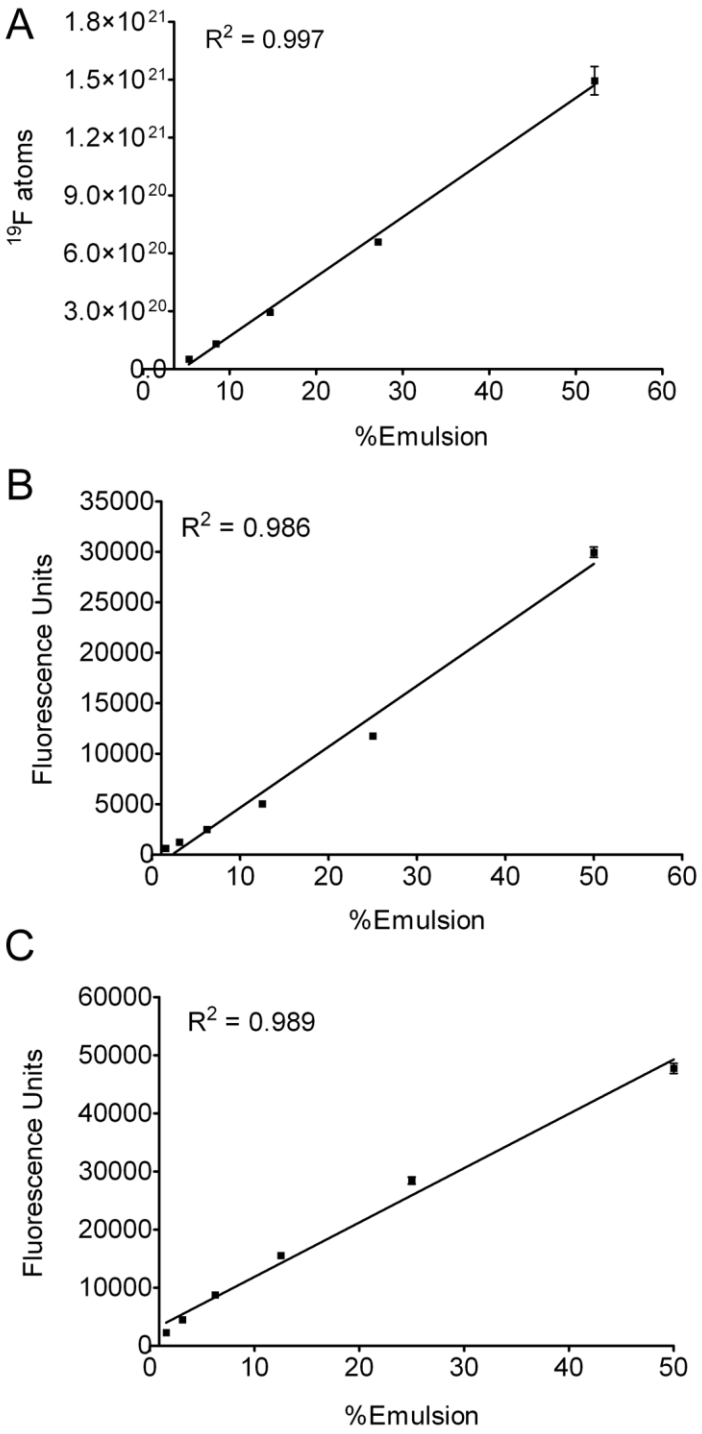

Figure 5.3. Linear correlation of imaging signals with nanoemulsion concentration.

Linear correlation is observed for **A.** ^{19}F atoms (n=2). **B.** Cy3 (n=3). **C.** DiR (n=3). Errors bars are standard deviation from mean.[217]

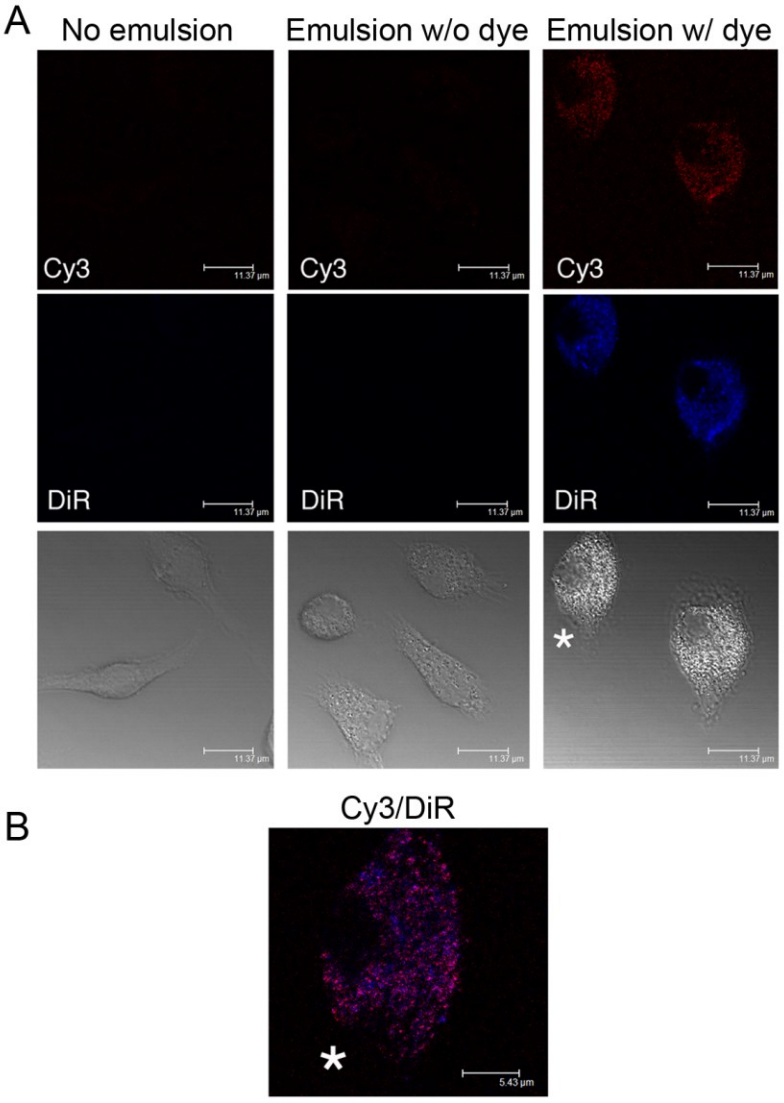

Figure 5.4. Confocal images of macrophages exposed to dual fluorescent nanoemulsion.

A. Confocal fluorescence images of RAW 264.7 macrophages exposed to culture medium (left column), nanoemulsion with no dyes (middle), and dual fluorescent celecoxib nanoemulsion (right). The scale bar = 11.37 μm. **B.** Merged image showing coincident DiR and Cy3 signals (scale bar = 5.43 μm). Image by Dr. John A. Pollock, 2013.[217]

5.3.2 Evaluation in a neuropathic pain rat model

For experimental details and results, see chapter 7. The goal of this study was to evaluate if nanoemulsion can be detected at the inflamed site using the two imaging functionalities. A neuropathic pain model was utilized, where ligation of sciatic nerve causes local inflammation and neuropathic pain. Of note, we evaluated a fluorescent PFCE nanoemulsion in this model for simultaneous imaging and therapy (reduced inflammation and pain), which is partly described in chapter 7. Doctoral thesis by Kiran Vasudeva contains the full details of the study. In the current study, fluorescence was observed at the inflammatory site confirming the delivery of nanoemulsion. Live animal fluorescence imaging and *ex vivo* tissue imaging (Figure 7.10) separately confirmed the presence of nanoemulsion at the injured sciatic nerve, but not in the contralateral nerve and the sciatic region of healthy animal. However, ^{19}F NMR assessed after tissue collection showed undetectable ^{19}F signal in the injured nerve. These results necessitated further studies to be conducted to increase the ^{19}F MRI sensitivity, which is described in chapters 6 and 7.

5.4 Conclusions

The study clearly shows that the nanoemulsion platform developed in chapter 4 is amenable to modifications to obtain a dual fluorescent theranostic system. The reported theranostic nanoemulsion was designed to offer flexibility for *in vitro* and *in vivo* inflammation imaging, and histological analysis using three distinct imaging functionalities (visible and NIRF, and ^{19}F MR). Despite the multifunctional nature, the nanoemulsion displayed moderate storage stability based on size analysis for at least 45 days. Both dyes were detected in the nanoemulsion and in cells. The spectral

characteristics of the two dyes in the nanoemulsion were retained following processing and storage at low temperature. Due to the degradation of DiR dye to a lower wavelength product, careful consideration has to be given for possible spectral interference during imaging. The pilot *in vivo* experiment showed encouraging results for the utility of this nanoemulsion to detect inflammation using NIRF imaging. However, the complementary imaging method (^{19}F MR) requires further investigation to increase imaging sensitivity (described in chapters 6 and 7).

6 Development and *in vitro* characterization of PFPE nanoemulsion for increased MR sensitivity

6.1 Rationale

Our goal was to design, develop and evaluate fluorescent PFC theranostic nanoemulsions for macrophage imaging and monitoring of therapeutic efficacy. In chapters 3, 4, and 5, our efforts to develop stable non-toxic nanoemulsions were encountered with problems pertaining to toxicity, cost, drug solubility and imaging functionality. The results from these studies provided valuable information to be considered for successful theranostic design. For example, the choice of the components needs careful investigation in order to attain drug solubility, while realizing formation of a stable and non-toxic nanoemulsion. Due to the instability of NIRF (DiR) dye, a balance has to be maintained to achieve optimum stability and *in vivo* imaging. In this chapter, the formulation from chapter 4 is further modified with increased amount of PFPE and a lower wavelength carbocyanine dye (DiD) to resolve ^{19}F MR sensitivity problem as well as instability of NIRF dye. *In vivo* evaluation of the developed theranostic is presented in chapter 7.

As mentioned before, formulations utilized for *in situ* macrophage labeling contain high amount of PFCs, 10-40% v/v (18-72% w/w). The high concentration of PFCs is required due to the inherent insensitivity of NMR principles. The amount of ^{19}F at the inflamed site depends on the extent of macrophage infiltration. If passive accumulation through damaged vasculature is involved in the accumulation, then the extent of EPR in the inflammation model also dictates the nanoemulsion accumulation,

thus affecting the sensitivity. The concentration of PFPE reported in chapters 4 and 5 is 4% v/v, which is significantly lower than the formulations reported in the literature. Additionally, the low EPR effect and macrophage infiltration in the localized nerve inflammation would have led to low accumulation of nanoemulsion, thus affecting the MR sensitivity. Previously, a fluorescent nanoemulsion containing high PFC content (20 % v/v) detected neuronal injury by ^{19}F MRI and fluorescence.[223] Therefore, we proposed to prepare nanoemulsions with increased amount of PFPE.

Nanoemulsion design

The droplet size and stability of the nanoemulsion could be affected by the amount of surfactant (seen in chapter 3) and processing conditions. An increase in surfactant amount could be required in order to stabilize the increased interfacial area due to proposed use of high PFPE content. The effect of surfactant amount and processing conditions on the PFPE nanoemulsion size and stability is not investigated in the previous chapters. We initially proposed to evaluate the effect of these factors on droplet size, PDI and stability by employing statistical design of experiments. Specifically, we proposed to use Box-Behnken design with three factors (surfactant, pulses, PFPE) and three levels as shown in Table 6.1. The levels for PFPE are selected between 8-12.5% v/v (15-22.5% w/v), which is still lower than literature reported concentrations for PFCE[223] because PFPE has two-fold greater ^{19}F atoms compared to PFCE. The amount of Miglyol was not changed. Surfactant levels were proposed based on oil-to-surfactant ratio (O/S) and the total amount utilized in the nanoemulsion. Due to the presence of CrEL, concentration more than 5-6% w/v were not preferred. The range of O/S (3.4 to 13.1)

obtained includes the O/S (3.4) for formulations reported in chapters 4 and 5. Based on this design, three nanoemulsions were experimented and one of them met the desired criteria. Therefore, the design was not completed. This nanoemulsion was further modified with fluorescent dye for dual mode imaging and evaluated for colloidal stability, toxicity, effect on phenotype, and uptake kinetics in RAW 264.7 cells.

Table 6.1. Proposed factors and levels for nanoemulsion optimization

Factors/levels	Old formulation	Low	Medium	High
PFPE (w/v)	7.2	15	18.75	22.5
Surfactant (w/v)	2.3	2	3.75	5.5
Pulses	30	30	38	46

6.2 Materials and methods

6.2.1 Materials

All chemicals and cell culture reagents were obtained from commercial sources and used without purification. DiD (1,1'-Dioctadecyl-3,3,3',3'-tetramethylindodicarbocyanine perchlorate) dye was purchased from Life Technologies. Cytochalasin B was obtained from Sigma Aldrich. Griess Reagent System for nitrite measurements was purchased from Promega (Madison, WI, USA). Phycoerythrin conjugated Rat anti-mouse CD86 (CD86-PE) antibody and Rat $IgG_{2a,k}$ conjugated to PE (isotype control) were obtained from BD Biosciences (San Jose, CA, USA). RAW 264.7 cells were cultured as previously reported in chapters 3, 4, and 5. The sources of all other reagents are same as mentioned in chapters 3, 4, and 5.

6.2.2 Preparation and characterization of fluorescent PFPE nanoemulsions

Preparation of nanoemulsions

Nanoemulsion formulation components and their amounts are shown in Table 6.2. Nanoemulsions were prepared as discussed in chapter 4 with some modifications. Celecoxib (5 mg) was solubilized in neat hydrocarbon oil, Miglyol 810N (0.95 g), by overnight stirring. For drug-free nanoemulsions, neat Miglyol 810N with or without the DiD dye was used. For dye-loaded nanoemulsions, DiD dye (100 μL of 2.5 mM ethanol stock) was added to Miglyol 810N with or without the solubilized drug and vortexed in the dark. PFPE, in required amounts (Table 6.2), was added and vortexed followed by the addition of surfactant mixture in 2 mL portions. The surfactant mixture contained 3% w/v CrEL and 2% w/v Pluronic® P105 dissolved in de-ionized water. After the addition of deionized water, the mixture was vortexed and processed on a microfluidizer (Microfluidics, M110S) for 30, 38 or 46 pulses at 6 bar inlet pressure. The total volume of the prepared nanoemulsions was 25 mL. The obtained nanoemulsions were sterile filtered (0.22 μm, Millipore) after equilibration for one day at 4 °C. pH of the drug-free nanoemulsion (DFNE) and celecoxib-loaded nanoemulsion (CXBNE) were recorded after filtration.

Colloidal characterization

Size and zeta potential analyzed similar to chapter 4. To assess serum stability, nanoemulsions were dispersed in complete cell culture media at 1:40 dilution, stored at 37 °C, and the sizes were recorded without further dilution. Similarly, nanoemulsions

were dispersed in buffered solutions at pH 5.0 and 7.4 at 1:40 dilution, incubated at 37 °C and sizes recorded at predetermined intervals. Samples for follow-up stability analysis were stored at 4, 25 and 37 °C. For formulation optimization studies, samples were also stored at 60 °C and analyzed for droplet size and PDI.

Drug loading

Briefly, 50 µL of nanoemulsion was dispersed in methanol in a glass centrifuge tube and vortexed for 1 min. This dispersion was subjected to centrifugation at 2000 rpm for 5 min at 4 °C to separate PFPE oxide. The supernatant was assayed without further dilution in triplicate using HPLC method reported in section 4.2.2.

Nanoemulsion characterization for fluorescent properties

To assess fluorescent properties, nanoemulsions were diluted with de-ionized water (8% v/v) and 150 µL of this dispersion was measured for fluorescence excitation and emission on Tecan Safire2 plate reader using a 10 nm bandwidth. Emission spectrum was obtained by measuring fluorescence intensity from 630-798 nm with 4 nm step size using excitation wavelength of 610 nm. The excitation spectrum was obtained by measuring fluorescence intensity for wavelengths 400-668 nm with 4 nm step size using emission wavelength of 690 nm. To assess fluorescence of dye in solution, the stock solution of DiD dye (2.5 mM in ethanol) was dispersed 40 µL in 460 µL of ethanol. This solution was further diluted 40 µL with 460 µL of di-water. 150 µL of this dispersion was assessed for fluorescence emission. To obtain nanoemulsion spectra, 40 µL of

nanoemulsion (10 μM DiD dye) was diluted with 460 μL of di-water and 150 μL of this dispersion was assessed for fluorescence.

In vitro cytotoxicity

The effect of nanoemulsions on the viability of RAW 264.7 macrophages was evaluated after a 24 h incubation at 37 °C with different concentrations of nanoemulsion dispersed in whole media. Control cells were not exposed to any treatments. Cells were plated at 10,000/well in 96 well plates and incubated overnight for adhesion, followed by 24 h incubation with treatments. After incubation, cells were washed twice with DPBS (1x). CellTiter-Glo® analyte was added (40 μL/well) to induce cell lysis by shaking in the dark for 20 min at RT. The obtained cell lysates (80 μL) were transferred to a white opaque plate and luminescence recorded. To assess the effect of nanoemulsion on cell number, a microscopy cell counting experiment was conducted after labeling the cells with Hoechst dye, which stains the nucleus. In this experiment, cells exposed to nanoemulsion as mentioned above in 96 well plates were fixed in 150 μL of 4% PFA and 50 μL cell culture media. Plates were incubated at RT for 20 min, washed twice with DPBS and exposed to Hoechst nuclear staining dye (5 μg/mL in DPBS) for 20 min at RT in dark. Cells were washed twice with DPBS and stored in 100 μL of DPBS at 4 °C until imaging on EVOS fluorescence microscope.

CD86 expression and nitric oxide release

In order to evaluate if nanoemulsion delivery affects any inflammatory mediators, nitric oxide (NO) release and CD86 cell surface markers were assessed in macrophages.

Cells plated in 6-well plates were incubated with DFNE or CXBNE (9.3 μM celecoxib) overnight. Cells exposed to LPS (200 ng/mL) were used as positive control, while the negative control cells were left untreated. Supernatants were analyzed for NO concentration using commercially available Griess reagent according to manufacturer instructions. Cells were collected by trypsinization and labeled with PE-conjugated anti-CD86 antibody or isotype control. After repeated washings with centrifugation (300g, 5 min) in DPBS / 2% FBS, cells were fixed with 2% paraformaldehyde, washed and re-suspended in DPBS. Samples were analyzed using flow cytometry (BD™Accuri) and 50,000 events were recorded. Nanoemulsion was detected in FL4, while CD86 fluorescence was recorded in FL2 channel. Gating was applied based on forward scatter (FSC) and side scatter (SSC) as shown in Figure 6.1. The mean fluorescence of gated cells was utilized for analysis. A moderate 20% reduction in viability was observed with LPS at 200 ng/mL.

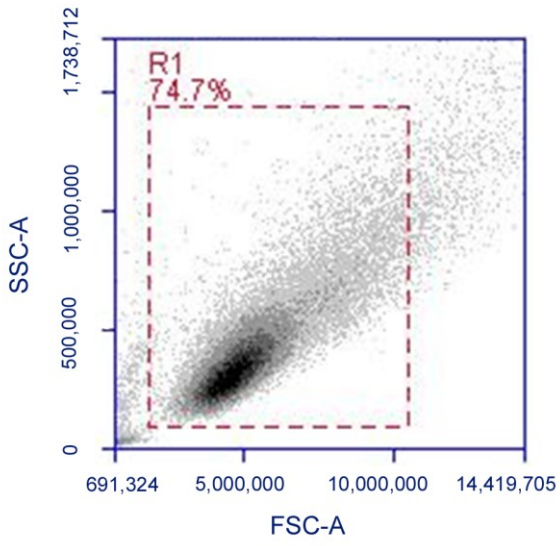

Figure 6.1. Gating strategy employed in flow cytometry based on FSC and SSC of cells.

Cellular uptake

Time- and concentration-dependent uptake kinetics of nanoemulsions was determined in macrophages. RAW 264.7 cells were grown in 6-well plates (0.3 x 10^6/well), incubated overnight for attachment, and followed by exposure to different doses of nanoemulsion (0, 2, 4, 6, 8 mg/mL PFPE) for 24 h in triplicates. Cells were trypsinized and washed by centrifugation. Cells were lysed using lysing buffer containing Triton-X100 (1%) (Sigma-Aldrich). A portion of the lysate was used for measuring protein content using Bradford protein assay (Bio-Rad, Hercules, CA). Cell lysates (150 μL) were transferred to a clear bottom 96-well plate and fluorescence intensity was recorded on a plate reader (Tecan Safire 2) at excitation wavelength of 610 nm and emission wavelength of 670 nm. The obtained fluorescence intensity was normalized to protein content (RFU/μg) and plotted against nanoemulsion concentration. For time-dependent uptake, cells were grown in 12-well plates (0.25 x 10^6/well). After overnight incubation, cells were exposed to nanoemulsion at single dose (4.2 mg/mL PFPE) for different time points (5, 15, 30, 60, 120, 240, 360 and 420 min) in triplicates. Cells were collected by trypsinization, re-suspended in DPBS / 2% FBS, and washed twice by centrifugation (300g, 5 min). Cells were fixed with 2% PFA and analyzed by flow cytometry (BD Accuri™). 20,000 events were recorded in the gated region (Figure 6.1) and the nanoemulsion was detected in FL4. Data were plotted as mean fluorescence at each time point for triplicate samples.

To assess the effect of phagocytosis inhibition on uptake, cells were plated in 12 well plates (0.2 x 10^6 cells) and left for attachment overnight. After aspiration of media and washing with DPBS, cells were exposed to different doses of nanoemulsion with or

without cytochalasin B (5 μg/mL) for 2.5 h in triplicates. Cells were collected by trypsinization, washed twice by centrifugation (300g, 5 min, 4 °C) in DPBS / 2% FBS, and fixed with 2% PFA. Cells re-suspended in DPBS were analyzed by flow cytometry (BD Accuri™). Nanoemulsion was detected in FL4 and 30,000 events per sample were collected in the gated region (Figure 6.1). The concentration of cytochalasin B was chosen based on a dose-dependent toxicity assessment performed in these cells for 2.5 h. Effect on cell viability was assessed by luminescent assay as described in chapter 3.

Confocal microscopy

RAW 264.7 macrophages (0.2 x 10^6 cells) were seeded on glass coverslips in a 24 well plate and left for adhesion overnight. Cells were then incubated with nanoemulsion (30 μL) in culture media (1 mL) for two hours at 37 °C. Cell were then washed with DPBS and fixed with 4% paraformaldehyde (PFA) for 20 min at RT and stained with Hoechst for nuclei visualization. For kinetic studies, cells were incubated with nanoemulsion (30 μL in 1 mL medium) for 5, 15, 30 and 60 min at 4 and 37 °C, fixed with 4% PFA, and stained with DAPI. After washing with DPBS, coverslips were mounted using Diamond anti-fading medium (Invitrogen, Grand Island, NY). Fluorescence was monitored using a Zeiss Apotome system equipped with a Zeiss HPO PL APO 63x oil immersion lens (numerical aperture 1.4-0.6). For co-localization with acidic compartments, cells were seeded on a glass bottom dishes and left for adhesion. Cells were then incubated with nanoemulsion (30 μL in 1 mL medium) for 45 min at 37 °C, and Lysotracker Green DND-26 (1 μM) (Invitrogen, Grand Island, NY) was added for 15 min at 37 °C. Cells were washed with DPBS and immediately imaged using a

Zeiss Apotome system equipped with a Zeiss HPO PL APO 63x oil immersion lens (numerical aperture 1.4-0.6). Kinetics study and co-localization study was performed by Dr. Wissam Beaino at University of Pittsburgh.

PGE_2 assessment

To assess the effect of CXBNE delivery on COX-2 inhibition, PGE_2 was quantified in activated macrophages (RAW 264.7). Cells were plated at 0.3 million/well in 6 well plates and left to adhere overnight. Cells were exposed to DFNE, CXBNE, DMSO, and free celecoxib in DMSO or media. Celecoxib was used at 10 μM in nanoemulsion and free drug treatment groups. After 24 h exposure, cells were washed 2x with DPBS and exposed to LPS containing media (0.5 μg/mL) or media alone. LPS was used at 0.5 μg/mL. After 3.5 h, supernatant was collected and analyzed according to manufacturer instructions (PGE_2 ELISA kit) for PGE_2 assessment.

6.3 Results and discussion

6.3.1 Preparation and characterization of nanoemulsions

The PFPE nanoemulsions reported in chapters 4 and 5 required further optimization to increase detection sensitivity using *in vivo* ^{19}F MRI. In an attempt to achieve this, three design points were experimented from Table 6.1. However, the full design was not completed as one of the three tested nanoemulsions met the desired criteria. Our criteria was size < 150 nm, PDI < 0.2 and stability at 60 °C for at least one month. All nanoemulsions were devoid of multiple size populations showing monomodal distribution and displayed PDI less than 0.15 (Table 6.2). Nanoemulsions prepared with 2% w/v surfactant (NE2 and NE3) showed smaller droplet size compared to 3.75% w/v

(NE1) (Table 6.2). We observed an increase in average size of approximately 20 nm in nanoemulsion with increased surfactant amount (NE1), while NE2 and NE3 showed comparable average droplet size (Table 6.2, Figure 6.2A). At elevated temperature (60 °C), size was monitored for at least 2 months in order to select the nanoemulsion with superior stability. NE1 did not show significant increase in size for up to 2 months compared to NE2 and NE3, which increased size within two weeks of high temperature exposure (Figure 6.2B), demonstrating high colloidal stability of NE1. To compare storage stability of the nanoemulsions, droplet size was monitored for samples stored at 4, 25, and 37 °C (Figure 6.2C-E). The droplet size for all nanoemulsions tested showed no significant changes at 4 and 25 °C. However, samples stored at 37 °C showed an increase in size for NE2 and NE3, while NE1 remained stable throughout the test period of one month (Figure 6.2C-E). All the nanoemulsions showed a negative zeta potential (Table 6.2). Based on the results from these three formulations, it appears that high surfactant amount (low O/S) is required for high colloidal stability under storage and at elevated temperature. However, in comparison to PFPE formulations in chapters 4 and 5, the optimized nanoemulsion has higher O/S (5.96 vs. 4.78) i.e. lower amount of surfactant to total oil content.

Table 6.2. DLS characterization of nanoemulsions NE1, NE2 and NE3.

Code	PFPE (%w/v)	Surfactant (%w/v)	Pulses	O/S[a]	Size (nm)	PDI	Zeta potential (mV)
NE1	18.75	3.75	38	5.96	156	0.12	-14.0
NE2	18.75	2	30	11.17	136	0.10	-12.1
NE3	18.75	2	46	11.17	133	0.10	-12.8

[a]O/S = Oil to surfactant ratio. Oil phase includes Miglyol 810N and PFPE oxide

The effect on cell viability was comparable for nanoemulsions with low and high surfactant amounts (Figure 6.3). We observed an increase in cell metabolic activity with these nanoemulsions. In order to assess if this increase in metabolic activity is due to increased cell number, a separate experiment was conducted. Cell number was obtained for each treatment in triplicates by counting the nuclei of fluorescently stained cells. An increase in cell number at some concentrations of nanoemulsion was observed (Figure 6.3B) for NE1. A plausible explanation for this cellular behavior is the gas-dissolving capability of PFCs. During processing and storage, nanoemulsions could dissolve oxygen. An increased cell metabolic activity and number could be the result of the oxygen supplied to cells in culture. Of note, this increase in cell metabolic activity and numbers is not a toxic event and hence further studies to explore the associated mechanisms were not attempted. Based on these results, the composition and processing conditions of NE1 were selected as optimized to prepare fluorescent nanoemulsions for *in vitro* and *in vivo* studies.

The optimized nanoemulsion was modified for fluorescence imaging using a lipophilic fluorescent dye, DiD. The addition of the dye reduced the droplet size by 20-25 nm, probably due to its adsorption in the surfactant layer. A small reduction in zeta potential was also observed compared to dye-free nanoemulsions (-6 mV vs. -14 mV). There was no influence of drug incorporation on average droplet size and zeta potential (Figure 6.4A). The stability of the nanoemulsions was investigated by monitoring average size changes with time at 4 °C storage, serum exposure, and variation in dispersant pH. Both DFNE and CXBNE displayed high stability under storage at 4 °C (Figure 6.4B). Even after 100 days, the size distribution by intensity showed a single

peak (Figure 6.4C). A small increase in size of less than 15 nm was noted after 100 days and PDI remained below 0.15. Incubation of nanoemulsions with serum-containing media showed a small reduction in size (Figure 6.4D). However, the serum did not affect the size distribution (Figure 6.4E). Average droplet size and size distribution of nanoemulsions remained unaltered after incubation at pH 5.0 and 7.4 for 5 days (Figure 6.4F). The pH of the undiluted nanoemulsions was between 6.75 and 7.1, which is close to physiological pH of 7.4. These results clearly indicate that the nanoemulsion is stable under different stress conditions and was acceptable for *in vitro* and *in vivo* biomedical applications.

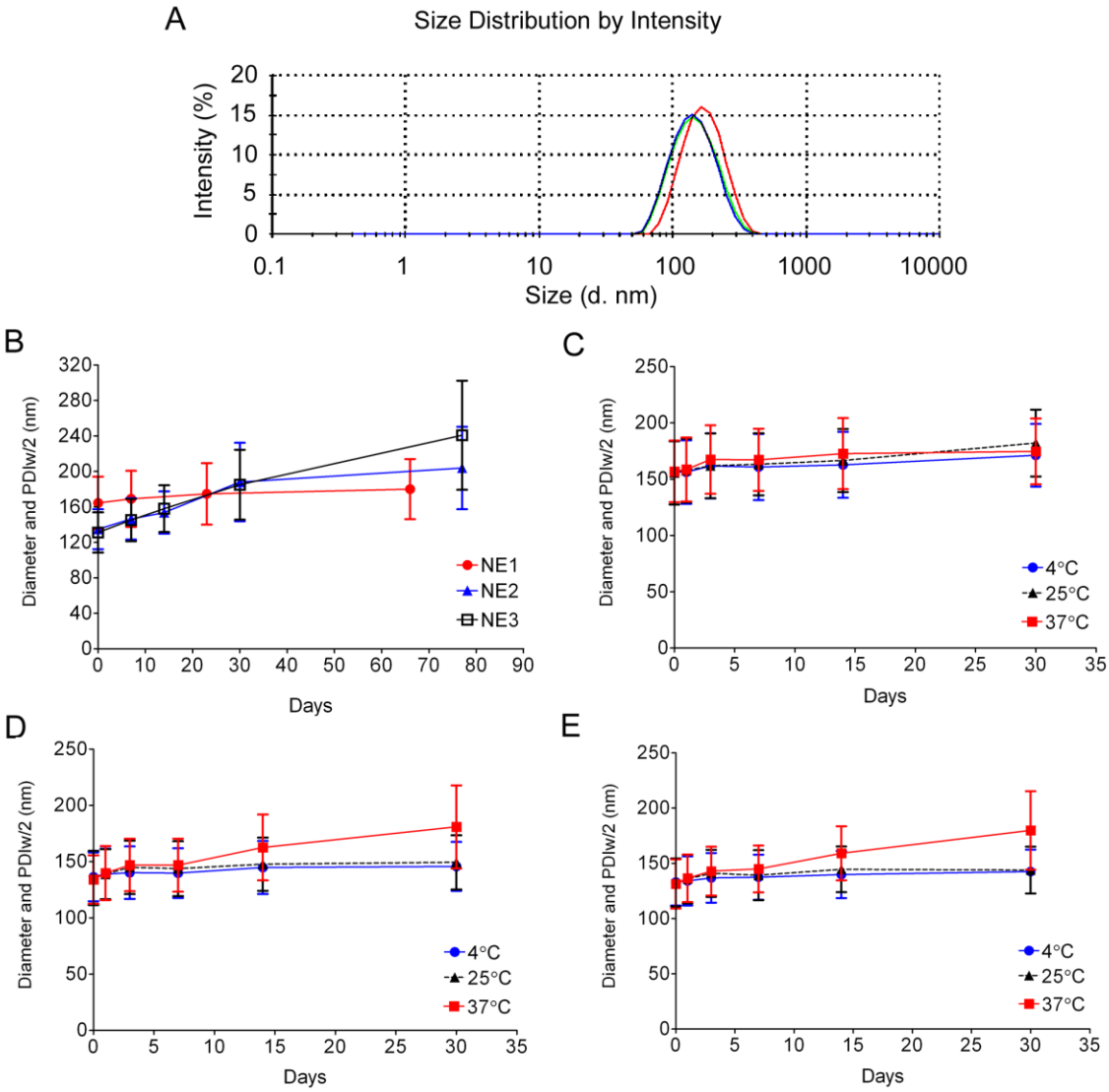

Figure 6.2. Size and stability of dye-free PFPE nanoemulsions.

A. Size distribution of nanoemulsions NE1 (red), NE2 (blue), and NE3 (green). **B.** Nanoemulsion droplet diameter changes with time stored at 60 °C. Storage stability of nanoemulsions **C.** NE1, **D.** NE2, and **E.** NE3 stored at 4, 25 and 37 °C. Error bars represent PDIw/2.

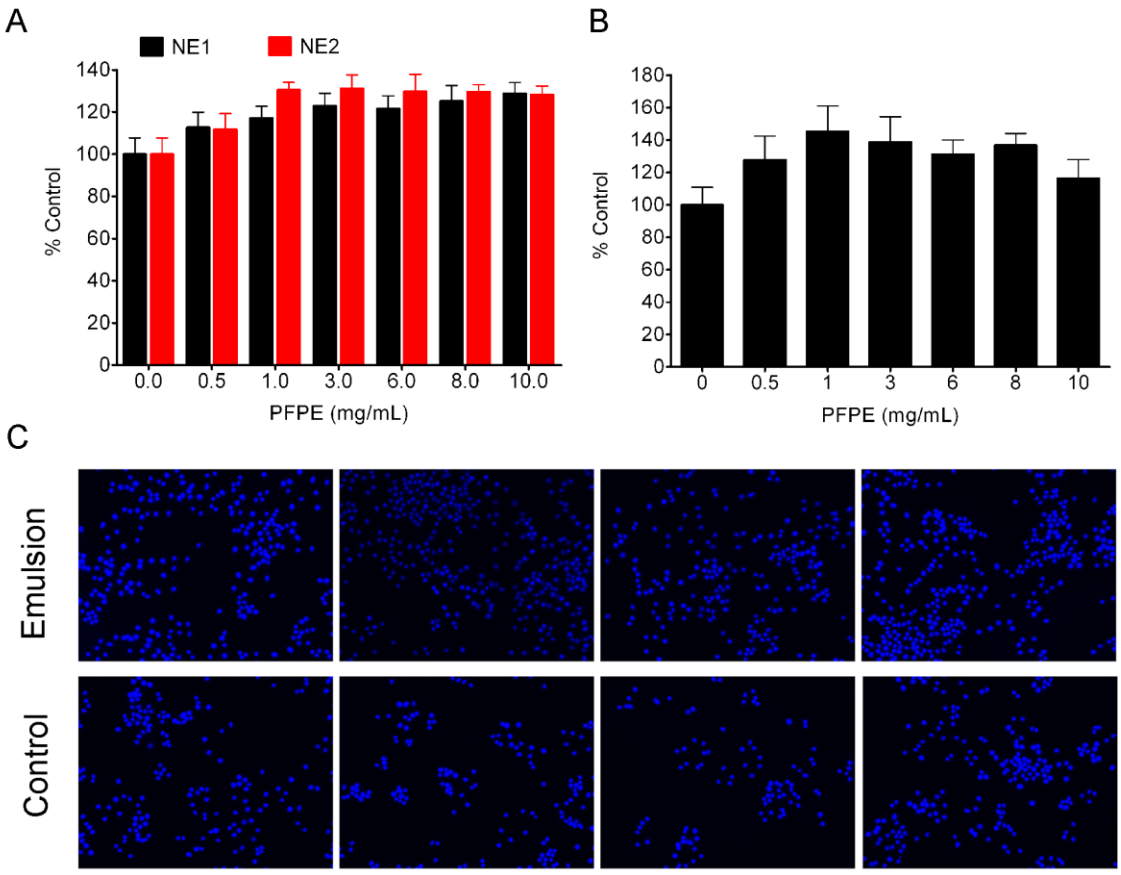

Figure 6.3. Effect of dye-free PFPE nanoemulsions on macrophage viability.

A. Cell viability assessed for NE1 and NE2 by quantitation of ATP. **B.** Effect of cell growth based on nuclei counts of NE1 exposed cells. **C.** Representative microscopy image of nuclei for nanoemulsion-exposed and untreated cells showing visible difference in cell number. Data is obtained from at least triplicate measurements.

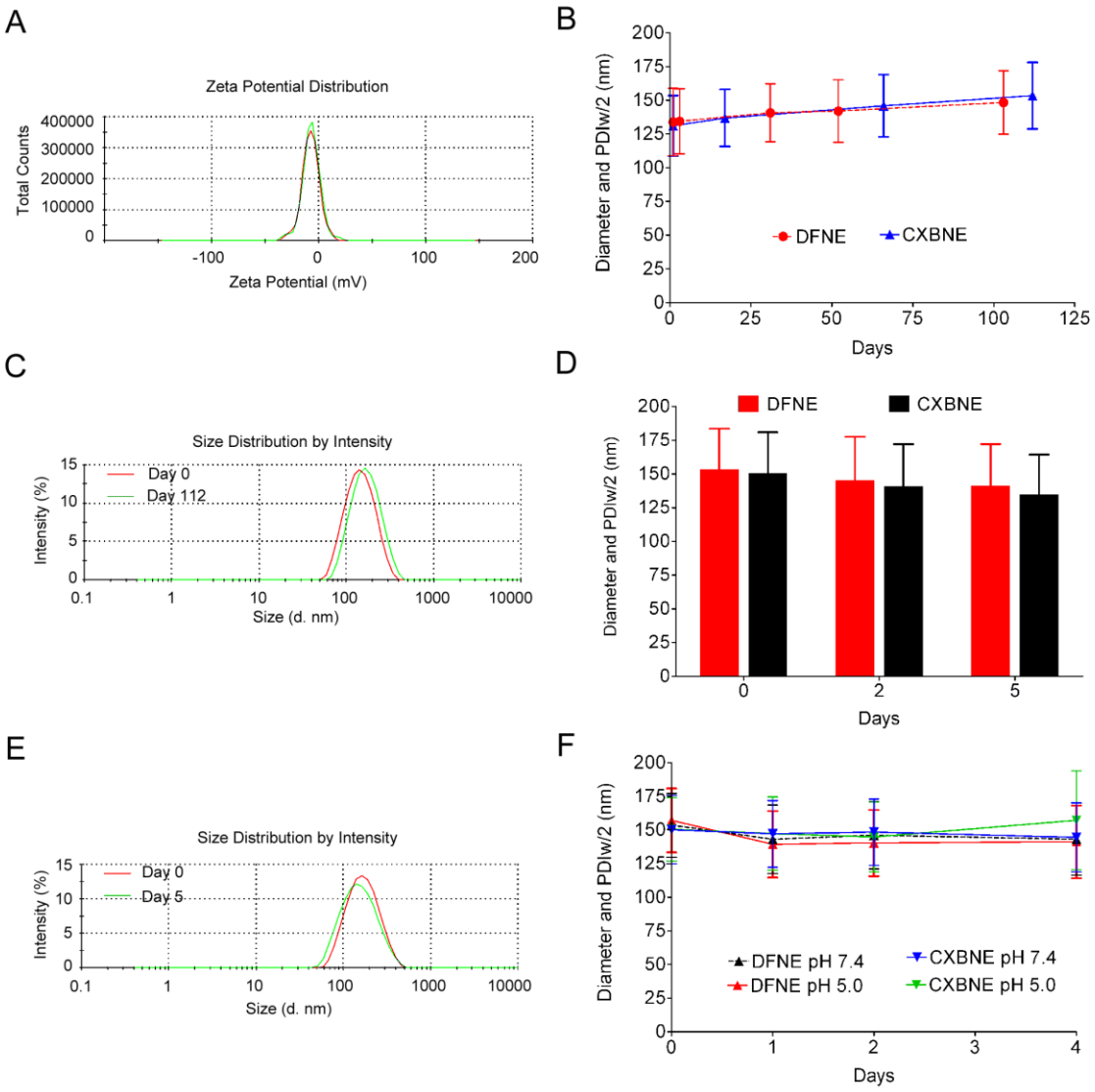

Figure 6.4. Characterization of the optimized fluorescent dye-loaded nanoemulsions, DFNE and CXBNE, using DLS.

A. Zeta potential distribution of DFNE (red) and CXBNE (green). **B.** Graph showing droplet diameter changes with time (days) for nanoemulsions stored at 4 °C. **C.** Comparison of size distribution for CXBNE at day 0 vs. day 112, showing single peak. **D.** Droplet diameter changes in serum containing cell culture media at 37 °C. **E.** Overlay of size distribution for media exposed CXBNE showing monomodal distribution. **F.** Droplet diameter changes of CXBNE incubated in pH 5.0 and 7.4 buffer at 37 °C.

Nanoemulsions were characterized by ^{19}F NMR spectroscopy and fluorescence. ^{19}F NMR of the nanoemulsions (not included) showed characteristic peaks similar to the spectrum of pure PFPE oxide.[205] In order to determine the appropriate fluorescence conditions for *in vitro* and *in vivo* studies, emission and excitation spectra for DFNE and CXBNE were determined. Ex/Em of 648 / 668 nm were observed for both nanoemulsions (Figure 6.5A-B). The presence of drug did not show any shift in the emission and excitation spectra. A slight blue shift was observed compared to the free dye (Figure 6.5C) dissolved in ethanol/water mixture (654 / 678 nm), possibly due to the presence of surfactants in the nanoemulsion. However, the fluorescence properties remained in the NIR region, which is ideal for *in vivo* imaging due to the reduced autofluorescence.

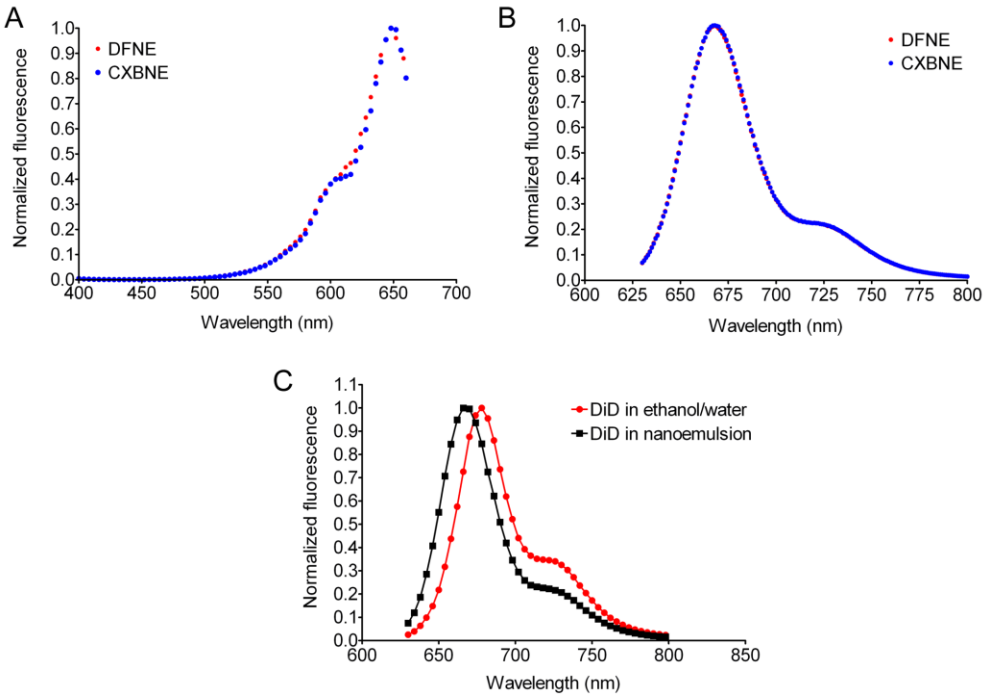

Figure 6.5. Fluorescence characterization of DiD dye in nanoemulsions and solution.

A. Excitation and **B.** Emission spectra. **C.** Comparison of emission spectra for DiD dye in ethanol/water mixture and nanoemulsion.

6.3.2 *In vitro* evaluation in RAW 264.7 macrophages

The optimized nanoemulsion, with and without celecoxib, was tested at different doses in macrophages and did not affect their viability after 24 h exposure (Figure 6.6A). In order to ascertain that these nanoemulsions did not produce any pro-inflammatory effects, NO release and CD86 expression changes were monitored after 24 h of exposure. A non-toxic concentration of LPS was used and cells were activated for 18 h. NO and CD86 were chosen as the markers for macrophage activation. LPS was used as a positive control to induce the pro-inflammatory phenotype in macrophages, which leads to increased CD86 expression and NO release. CD86 expression and NO release were not altered by nanoemulsions (Figure 6.6B-C). CD86 and NO levels were comparable to untreated cells, and significantly lower than LPS-activated cells, which clearly indicate that nanoemulsions do not stimulate pro-inflammatory phenotype in macrophages.

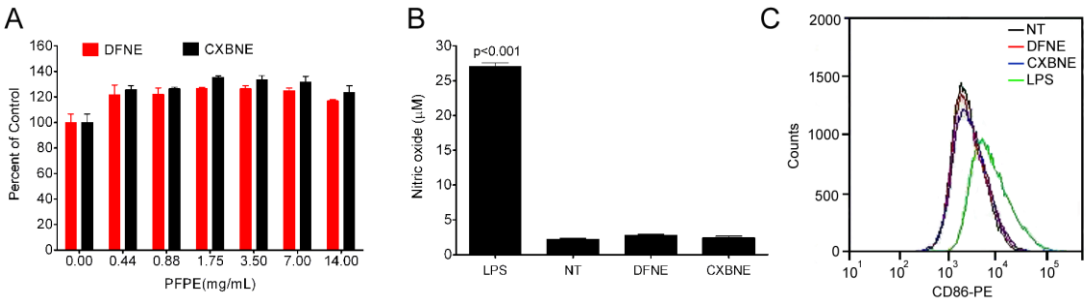

Figure 6.6. Effect of DFNE and CXBNE on macrophage viability and activation.

A. Viability of RAW 264.7 macrophages exposed to DFNE and CXBNE for 24 h (n = 4). **B.** Nitric oxide release from macrophages exposed to nanoemulsions for 24 h (n = 3). Data in panels A and B is shown as mean ± SD **C.** CD86 expression in macrophages exposed to nanoemulsions for 24 h. Cells not exposed to any treatment are designated as NT (no treatment).

To understand the uptake and intracellular fate of nanoemulsions, cellular uptake studies were conducted in RAW 264.7 macrophages. Fluorescence analysis of cells exposed to nanoemulsion showed an identical emission profile (Figure 6.7A) to that of dye in solution and nanoemulsion (Figure 6.5). Whereas, untreated cells did not display fluorescence. This result confirms that the fluorescent properties of the theranostics are not altered and can be detected in cells using fluorescence microscopy. Confocal microscopy showed that the nanoemulsions were readily internalized by macrophages (Figure 6.7B) and localized to acidic endosomal/lysosomal compartments (Figure 6.7B-C). This experiment was conducted 45 minutes after labeling the cells with the nanoemulsion. Typically, NPs sort through the endosomal-lysosomal compartments, unless a lysosomal escape mechanism is made part of the system. Based on the pharmacological effect we observed in the cells (demonstrated in the next section), it is likely that the nanoemulsion could physically dissociate and release the drug to act on the COX-2 enzyme. In order to probe the exact mechanism, a time-dependent co-localization study with endosomal and lysosomal-specific antibodies has to be conducted.

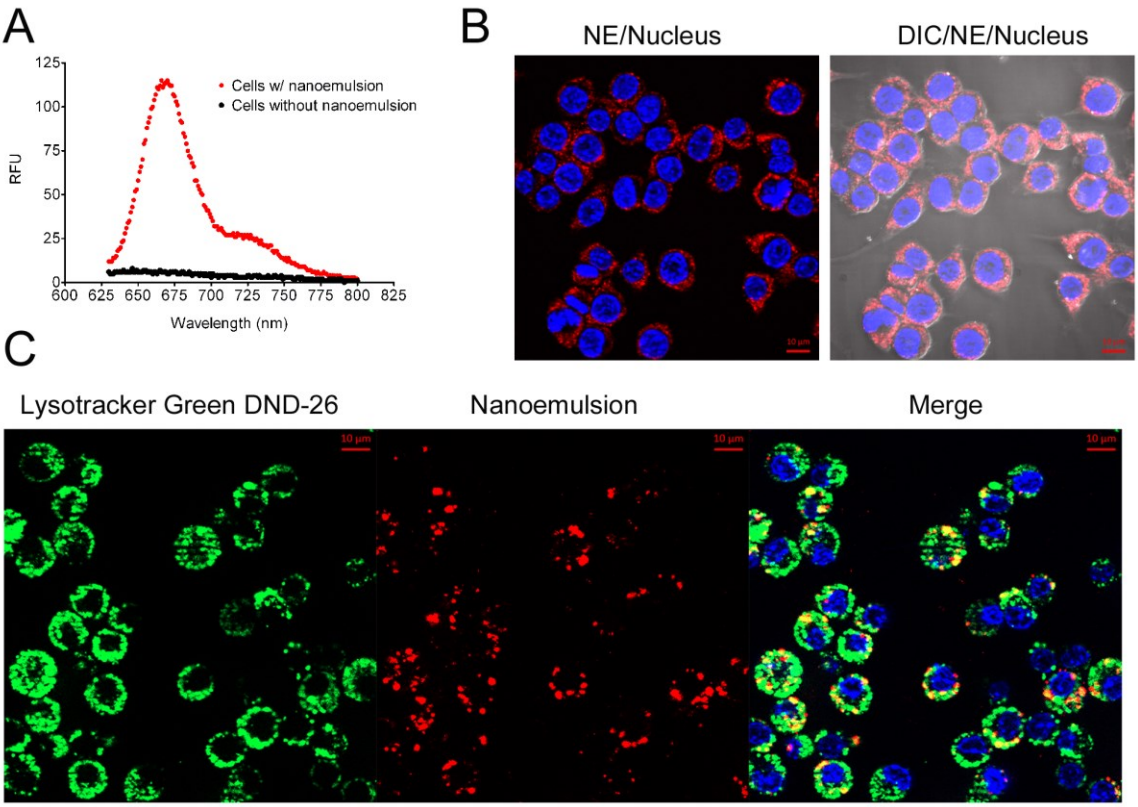

Figure 6.7. Characterization of nanoemulsion uptake in macrophages using fluorescence methods.

A. Comparison of fluorescence emission of cells treated with or without CXBNE showing Em at 670 nm. **B.** Confocal microscopy of cells incubated with nanoemulsion (30 µL/mL) for 2 h at 37 °C. **C.** Confocal images showing co-localization of nanoemulsion (red) with acidic compartments (green) labeled with Lysotracker Green-DND. Merged image show the co-localized pixels (yellow). Nuclei are stained with DAPI (blue). Images are recorded by Dr. Wissam Beaino, University of Pittsburgh, 2014.

^{19}F NMR of cells exposed to nanoemulsion also confirmed the uptake based on characteristic peaks of PFPE (not included). Two possible mechanisms of nanoemulsion internalization exist in macrophages. Nanoemulsions can enter cells either passively through membrane penetration or actively via phagocytosis, endocytosis and pinocytosis.[224] In order to identify the mechanism of internalization, RAW 264.7 macrophages were incubated with the nanoemulsion for 5, 15, 30, and 60 min. At 37 °C,

nanoemulsion was easily detected at the cell membrane as early as 5 min, and the internalization increased overtime with a punctuated fluorescent staining pattern indicative of localization in discrete vesicular compartments, suggestive of an endocytic pathway of internalization. At 4 °C, barely detectable levels of nanoemulsion was observed after 5 min, and minimal internalization was noted after 60 min (Figure 6.8A). These results demonstrate predominantly energy-dependent active mechanisms of nanoemulsion internalization in macrophages. In addition, dose- and time-dependent uptake of nanoemulsion was observed in macrophages (Figure 6.8B-C). The cell-associated fluorescence reached saturation at higher nanoemulsion concentrations, which is typical for an endocytic pathway of uptake.[225] A similar uptake profile was observed with the PFPE nanoemulsion reported in chapter 4, Figure 4.6, suggesting a related mechanism of uptake of these nanoemulsions. A linear increase in uptake with time was observed at a single concentration of nanoemulsion; within 2 h of exposure, more than 90% of cells were shown to be positive for nanoemulsion. The uptake is expected to saturate with increased incubation time and higher concentration. The highest incubation time used was below 12 h in order to avoid variation in cell number across time points due to the excepted cell division at longer time points.

One of the key mechanisms of NP uptake in macrophages is phagocytosis. To assess if phagocytosis is involved in the internalization of nanoemulsions, cellular uptake was compared in the presence and absence of the phagocytosis inhibitor cytochalasin B. Cellular uptake was significantly lower with cytochalasin B (Figure 6.8D). In the presence of cytochalasin B, nanoemulsion uptake was reduced at least by 70%, and this result was observed at all tested nanoemulsion concentrations, confirming that the uptake

is predominantly mediated through phagocytosis. Based on the presented results, it can be proposed that nanoemulsion enters the cells via an endocytic mechanism and moves intracellularly via the endosome-lysosome pathway.

The pharmacological effect of celecoxib delivery was evaluated by quantitation of PGE_2 in activated macrophages. Similar to our previously reported results in chapter 4, CXBNE produced significant reduction in PGE_2 produced by LPS-activated macrophages compared to DFNE (Figure 6.9). This reduction was comparable to free drug delivered in DMSO. Together, these data strongly suggest that the nanoemulsion, efficiently internalized by macrophages in a dose- and time-dependent manner and inhibiting COX-2 enzyme activity can produce anti-inflammatory effects *in vivo.* To test the *in vivo* efficacy of these nanoemulsions as imaging and therapeutic agents, a paw inflammation mouse model was used, which is described in chapter 7.

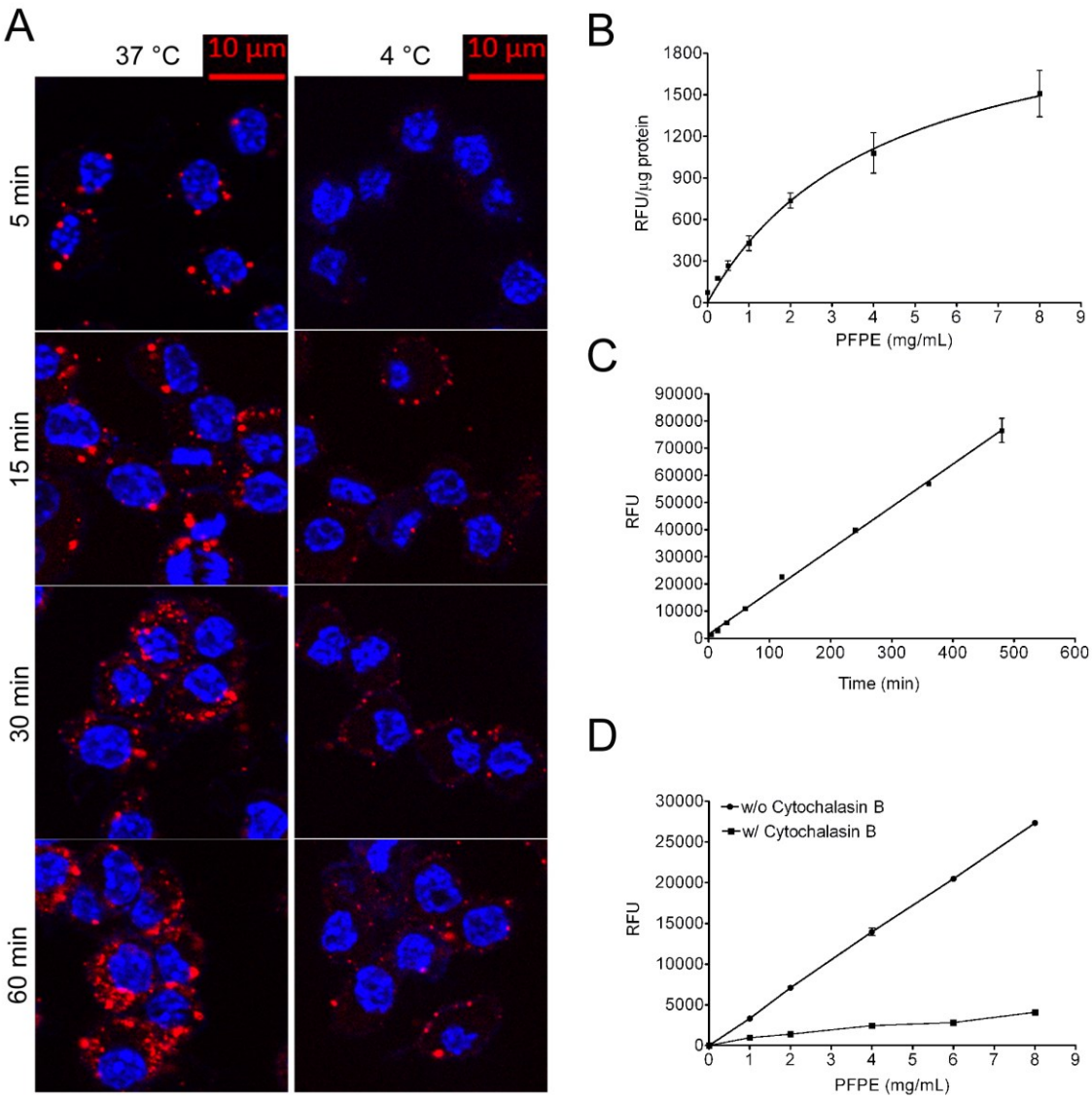

Figure 6.8. Cellular uptake kinetics of nanoemulsions.

A. Confocal images of cells exposed to nanoemulsion for 5, 15, 30, and 60 min incubated at 4 and 37 °C (Microscopy by Dr. Wissam Beaino, University of Pittsburgh, 2014). **B.** Dose dependent uptake of nanoemulsion in macrophages. Dose is represented on x-axis as PFPE (mg/mL). **C.** Time-dependent uptake of nanoemulsion (4 mg/ml PFPE) in macrophages. **D.** Comparison of uptake between cells exposed to different doses of nanoemulsion with or without phagocytosis inhibitor cytochalasin B (5 µg/mL). Uptake was performed for 2.5 h. Data in panels B, C, and D is from triplicates expressed as mean ± SD.

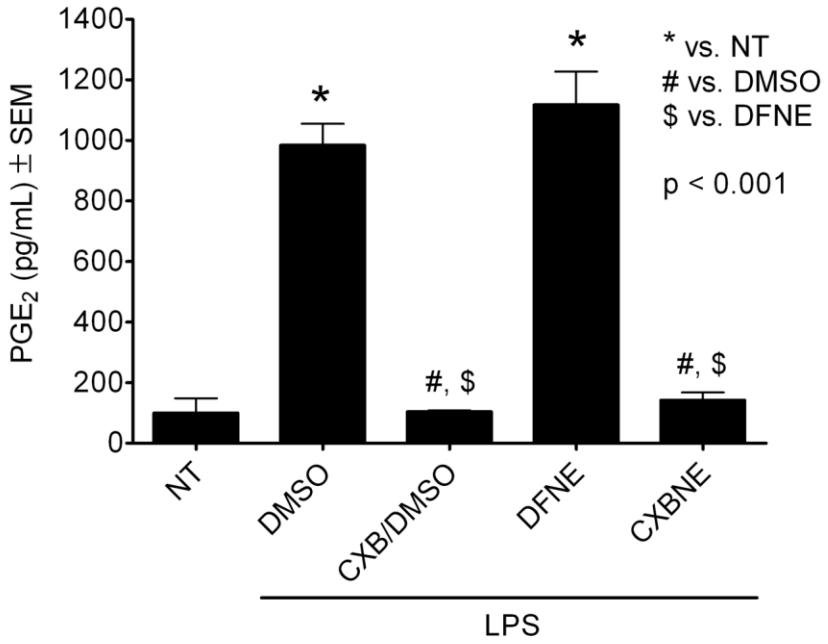

Figure 6.9. Comparison of PGE_2 in supernatants of LPS activated macrophages pretreated with celecoxib in solution and nanoemulsion.

Cells that are not exposed to LPS are designated as no-treatment (NT). All the groups were compared with one-way ANOVA and Tukey's post-hoc multiple comparison test with statistical significance set at $p < 0.05$. Data is represented as mean ± SEM (n = 3).

6.4 Conclusions

The optimized nanoemulsions with increased PFPE content showed comparable droplet size and PDI to nanoemulsions reported in chapter 4. These nanoemulsions were shown to be stable under storage, serum exposure and varying pH. The individual imaging signatures namely ^{19}F MR and fluorescence excitation/emission were well conserved in the nanoemulsion and cells. Most importantly, nanoemulsions did not induce toxicity and inflammatory markers. The cellular uptake was shown to be dose- and time-dependent occurring predominantly through phagocytosis. In addition to internalization by macrophages, the multimodal theranostic was able to achieve

pharmacological activity in macrophages. With these encouraging results, the theranostic nanoemulsion was tested in a mouse inflammation model as described in chapter 7.

7 *In vivo* evaluation of PFC nanoemulsions in inflammatory models

7.1 Introduction

In this chapter, *in vivo* application of the theranostic nanoemulsions developed in chapters 5 and 6 is described. Specifically, PFPE nanoemulsion developed in chapter 6 was assessed for its capability to detect macrophages in inflammation and monitor changes in macrophage infiltration using optical *in vivo* imaging. This study was conducted in collaboration with Dr. Carolyn Anderson and Dr. Wissam Beaino at the University of Pittsburgh. The imaging potential of dual fluorescent PFPE nanoemulsion developed in chapter 5 is also demonstrated in a neuropathic pain rat model. Furthermore, the utility of a previously reported fluorescent PFCE theranostic nanoemulsion to detect neuronal injury and assessment of pain behavior in response to celecoxib delivered to macrophages will be discussed. The studies in neuropathic pain rat model were conducted in collaboration with Dr. John A. Pollock, Kiran Vasudeva and Muzamil Saleem at Duquesne University.

7.2 Materials and methods

7.2.1 Inflammation models

A mouse paw inflammation model was generated by subcutaneous (s.c.) injection of complete Freund's adjuvant (CFA) or carrageenan (CG) in the right hind paw. In these studies six to eight week old female ICR animals and SKH1 hairless (immune-competent) were purchased from Charles River Laboratories (Horsham, Pennsylvania). All animal studies were performed under the Guide for the Care and Use of Laboratory Animals under the auspices of Division of Laboratory Animal Resources (DLAR) of the

University of Pittsburgh. Mouse imaging was performed on IVIS® Lumina XR (Perkin Elmer, Waltham, MA, USA) at University of Pittsburgh Cancer Institute.

A neuropathic pain rat model included neuronal injury by sciatic nerve ligation. The studies with this model were performed by Kiran Vasudeva as previously described.[223] Rats were imaged on LiCOR Pearl® Impulse imaging station (LI-COR Biosciences, Lincoln, NE, USA) at Duquesne University.

7.2.2 *In vivo* studies in a mouse paw inflammation model

7.2.2.1 Pilot study to assess the imaging potential of nanoemulsion

In the pilot study, ICR animals were divided into two groups receiving either CFA or CG. Animals were injected with DFNE (150 μL) via tail vein under anesthesia. After 12 h, each group (n=3/group) received CFA (50 μL) or CG (40 μL) via s.c. injection in the right hind paw, while the left hind paw received normal saline. Animals were imaged at 2, 6, 9, 12, 24, 27, 30, and 48 h post-inflammation using the same imaging parameters. Paw thickness was measured before the injection of adjuvants and at all imaging time points. Lateral, translateral and ankle thickness was noted using Vernier calipers. Imaging was performed on IVIS® Lumina XR (Perkin Elmer, Waltham, MA). For each mouse, X-ray, white light and fluorescence images were co-registered. Imaging parameters included F/stop 2, medium binning, 3 sec exposure, high lamp level, and excitation and emission of 640 and 700 nm respectively. Settings were optimized to obtain an image that did not lead to detector saturation. To avoid saturation from the bladder and the abdominal region, a black cloth was used to cover these areas during imaging (Figure 7.1). At the end of the study, representative paws were collected for *ex vivo* ^{19}F NMR analysis. After 24 h, one animal from each group was sacrificed for cell collection and

development of flow cytometry method to detect nanoemulsion labeled macrophages. *In vivo* images were quantified by drawing a region of interest (ROI) around the inflamed leg and the contralateral control leg (Figure 7.1). Total fluorescence radiant efficiency was calculated after background subtraction. Data are presented as the fluorescence ratio of inflamed to control leg.

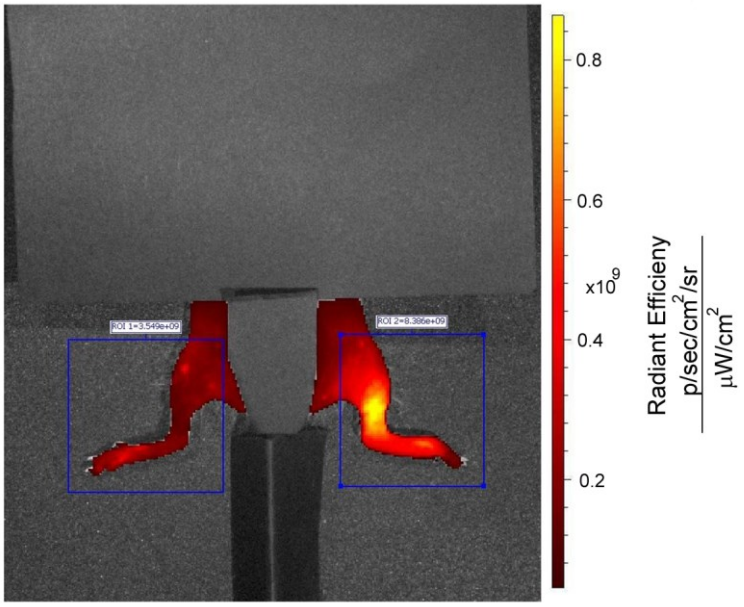

Figure 7.1. Representative fluorescence/white light image showing *in vivo* imaging method and ROIs used for quantification.

7.2.2.2 In vivo study to evaluate theranostic potential of nanoemulsions

SKH1 hairless mice were injected via tail vein with CXBNE (150 µL, 437.6 µM) (n = 5) or DFNE (150 µL) and free celecoxib dissolved in a surfactant mixture containing CrEL and P105 (115 µL) (n= 5) 12 h prior to paw inflammation induction by CFA. Live animals under anesthesia were imaged using *in vivo* fluorescence imaging using an IVIS® Lumina XR (Perkin Elmer; Waltham, MA) imaging station with 640 nm and

700 nm filters for excitation and emission, respectively. Images were acquired at 2, 6, 10, 24, 34, 48 and 72 h post CFA injection. Imaging parameters (exposure 1 sec, binning medium, lamp high, F/stop 2) were maintained for all time points. Images were quantified as described above. Mice were sacrificed (n = 3) after 72 h imaging time point, and organs were collected and imaged using the IVIS® Lumina XR imaging station, and then weighed. ROIs were drawn around each organ, and total radiant efficiency was calculated and normalized to the organ weight. The total dose was calculated by quantifying the fluorescence of a standard nanoemulsion dilution imaged with the same imaging parameters.

Ex vivo histological analysis

Following the *in vivo* studies at 72 h post-inflammation, mice injected with either CXBNE or DFNE and free celecoxib dissolved in the surfactant mixture were sacrificed and the inflamed paw was collected and snap frozen. In a separate experiment, SKH1 hairless mice were injected with DFNE (150 μL), and paw inflammation was induced by injection of CFA (50 μL) s.c. in the right hind paw. After 24 h, mice were sacrificed; spleens and paws were collected and snap frozen.

Dr. Wissam Beaino at University of Pittsburgh performed histology. Briefly, tissues were embedded in optimal cutting temperature (OCT) medium. 10 μm sections were obtained using a cryotome. Sections were fixed and stained for macrophages and neutrophils using CD68 and Gr1 antibodies, followed by secondary fluorescent antibodies for microscopy using a Zeiss Apotome system equipped with a Zeiss HPO PL APO 40x or 63x oil immersion lens (numerical aperture 1.4-0.6).

Statistical Analysis

A Two-way repeated-measures ANOVA with Bonferroni post-hoc test was utilized to compare mean fluorescence intensity of groups treated with DFNE or CXBNE at each imaging time point. Imaging time point and treatment were chosen as factors for this analysis. A student's t-test was used to compare mean fluorescence intensity of organs between groups treated with DFNE or CXBNE. Statistical significance level was set at $p < 0.05$ and data was analyzed using GraphPad Prism 6.

7.2.3 *In vivo* imaging in a neuropathic pain rat model

In vivo neuropathic pain model was utilized as a proof of principle study to assess whether the dual fluorescent nanoemulsion (prepared in chapter 5) can be detected *in vivo* at the inflammation site. Additionally, a previously published DiR-labeled PFCE nanoemulsion[215] from our lab was also utilized in this model to assess the effect of celecoxib delivery on pain behavior changes.

The following procedure was performed by Kiran Vasudeva in Dr. John Pollock's laboratory. Briefly, on 8th day post-sciatic nerve ligation, 0.3 mL of the nanoemulsion (chapter 5) was injected via tail vein. A healthy rat was used as the control. After 72 h, anesthetized animals were imaged on LiCOR Pearl® small animal imaging station. Due to the limited field of view, only a portion of the rat could be imaged. Rats were laid on the side and images were collected ensuring sciatic nerve regions are captured within the obtained image. Fluorescence (800 nm) and white light images were co-registered at focus offset -1. After live animal imaging, tissues, namely left and right sciatic nerves, lungs, kidneys, heart, liver and spleen, from both animals were collected and stored in 2% PFA in DPBS fixing solution at 4 °C.

The same procedure was utilized to evaluate the DiR-labeled PFCE nanoemulsion. Kiran Vasudeva, in her dissertation thesis, described experimental details and full results of the study. Figure 7.11 shows the author credits for this work. Briefly, animals receiving sham surgery and sciatic nerve ligation were used. Sham rats were used as control for pain behavior. Pain behavior was tested according to the protocol published in Vasudeva *et al.*[223], before the surgery and different days (up to 12 days) after the surgery. Sham rats did not receive any treatment. On day 8, rats with induced neuropathic pain were injected via tail vein, either drug-free or drug-loaded PFCE nanoemulsion or free drug dissolved in the surfactant mixture. Pain behavior was assessed on day 9, 10, 11, and 12. At the end of the study, sciatic nerves were collected from drug-free and drug-loaded nanoemulsions and assessed for ^{19}F content and NIRF imaging. Sciatic nerves were fixed, weighed and transferred to NMR tubes with fixing solution.

Ex vivo tissue ^{19}F NMR and NIRF imaging

The collected organs were cut into thin slices to fit into 5 mm NMR tubes. Inflamed sciatic nerves were cut, while the control and non-inflamed ones are placed intact in the NMR tubes. All the tissues were weighed on a digital balance, followed by the addition of fixing solution. These NMR tubes were imaged on LiCOR Odyssey® in 800 nm channel. ROIs were drawn using instrument software and the integrated fluorescence was obtained. Same tubes with tissues were assessed for ^{19}F content using ^{19}F NMR. For reference, a sealed capillary containing 0.02% v/v aq. TFA was placed inside the NMR tube. The height of the tube was adjusted such that the tissue sample is

with in the active region of NMR machine. NMR was performed on Bruker 500 MHz with delay time of 10 sec and 128 scans.

7.3 Results and discussion

7.3.1 *In vivo* studies in a mouse paw inflammation model

To test the *in vivo* diagnostic and therapeutic potential of the theranostic nanoemulsion, a murine inflammation model was utilized. The goal of these studies was: 1) to test the efficiency of nanoemulsions to detect the inflammation loci and 2) to image the response to celecoxib delivery i.e. changes in macrophage infiltration. Our working hypothesis is summarized in Figure 7.2.

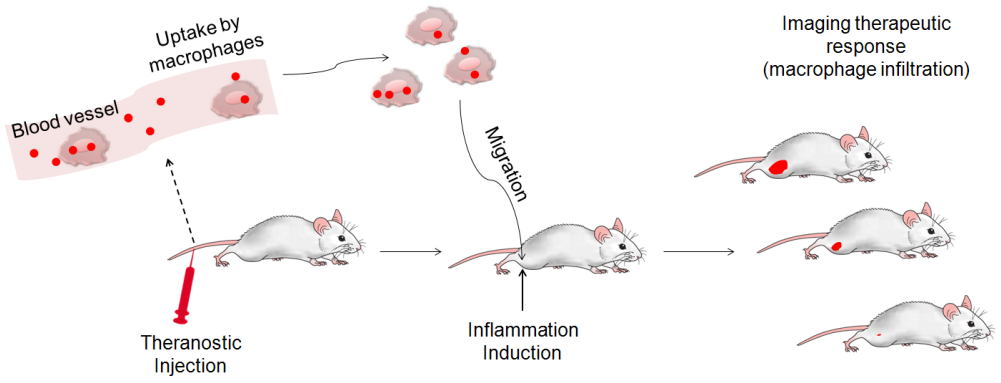

Figure 7.2. Schematic showing the proposed theranostic potential of PFPE nanoemulsion.

In the pilot study, CFA and CG were compared to assess the severity of inflammation based on the nanoemulsion fluorescence from the inflamed paw. CFA is an emulsion containing inactivated mycobacterium tuberculosis and it has been shown to induce local inflammation leading to increased leukocyte recruitment.[226,227] CG is a sugar and widely employed to induce local inflammation in rodents and arthritis in rats.[228]

Drug-free fluorescent PFC nanoemulsion, DFNE, was injected (tail vein) 12 h prior to inducing paw inflammation in order to label the monocytes/macrophages with nanoemulsion and subsequently monitor their infiltration to the inflamed site. Fluorescence imaging showed higher paw fluorescence from right paw injected with adjuvant (CFA/CG) compared to left paw receiving normal saline (Figure 7.3A). As shown in Figure 7.3B, paw thickness increased immediately after the adjuvant injection. Inflammation was higher and persisted longer with CFA compared to CG (Figure 7.3C). *Ex vivo* ^{19}F NMR of a paw tissue section from CFA-injected animal showed peaks from PFPE (Figure 7.3D), further confirming the presence of nanoemulsion at the inflamed site. Due to the high fluorescence observed, CFA was utilized for further studies.

To test the theranostic potential of the nanoemulsion, hairless SKH1 mice were used because our study showed background fluorescence due to shaving-induced skin irritation in ICR mice complicating the fluorescence quantification from the paw region. In these mice, first we evaluated the potential of the nanoemulsion to be delivered to macrophages. Immunofluorescence staining of the inflamed paw and spleen from mice injected with the nanoemulsion showed a strong and major co-localization of the nanoemulsion with macrophages and undetectable co-localization with neutrophils (Figure 7.4). These results show that the nanoemulsion is specifically internalized by macrophages *in vivo* at the site of inflammation and in spleen and is suitable to image and deliver therapeutics to macrophages. It should be noted that other antigen presenting or phagocytic cells like DCs and B cells, which are not investigated in our study, could also internalize the nanoemulsion.

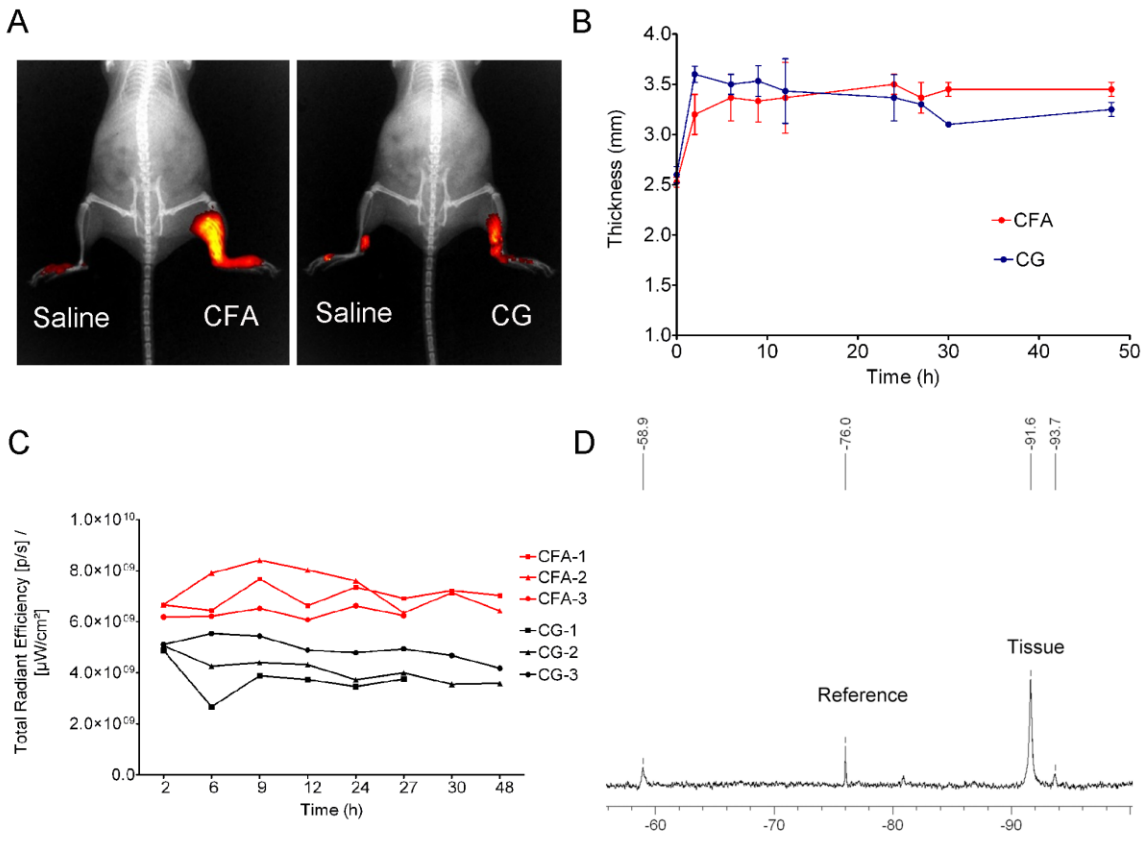

Figure 7.3. Pilot *in vivo* study showing characterization of CFA and CG mouse models.

A. Representative X-ray/fluorescence composite images show high fluorescence signal from CFA and CG injected paw compared to saline. **B.** Evolution of paw thickness for CFA and CG injected animals. **C.** Paw fluorescence changes with time of individual animals. **D.** Representative ^{19}F NMR of paw section showing presence of specific PFPE peaks. Data in panel B is represented as mean ± SD from three animals until 27 h and two animals thereafter.

With these results, the theranostic potential of the nanoemulsion *in vivo* in an inflammation setting was assessed by delivering celecoxib to macrophages and monitoring the subsequent therapeutic response using longitudinal fluorescence imaging. We evaluated this effect by comparing changes in fluorescence from inflamed paws between free drug and drug encapsulated in the nanoemulsion. In order to visualize

macrophage accumulation changes in the group receiving free drug, a drug-free nanoemulsion, DFNE (vehicle), was also co-administered. Based on the live animal imaging at different time points, a visible difference in fluorescence intensity was seen between the groups with time (Figure 7.5A). For both groups, we did not observe a statistically significant difference in the ratio of fluorescence intensity between inflamed paw and control paw until 10 h (Figure 7.5B). At the 24 h, significant reduction in the fluorescence ratio was observed for the group receiving CXBNE, which further reduced at 34 h time point and persisted till 72 h (Figure 7.5B). In the animals receiving free drug, paw fluorescence remained high at all the time points. The fluorescence intensity was assessed for both the nanoemulsions in order to exclude the contribution of differential nanoemulsion fluorescence to the observed fluorescence changes between the animal groups. Fluorescence intensity was observed to be slightly higher in CXBNE, which further supports the claim that CXBNE group showed reduced fluorescence with time compared to DFNE.

A plausible rationalization for the differences observed between the two groups could be attributed to the elimination of celecoxib from the body in the free drug group. Because there was a 12 h lag time before inducing inflammation, systemic concentration of celecoxib would have reduced ($t_{1/2}$ = 11.2 h for celecoxib) compared to celecoxib encapsulated in the nanoemulsion. Nanoemulsion-mediated celecoxib delivery is advantageous because it may reduce the drug elimination and also increases target accumulation, which leads to lower frequency of administration in future studies to induce anti-inflammatory effects.

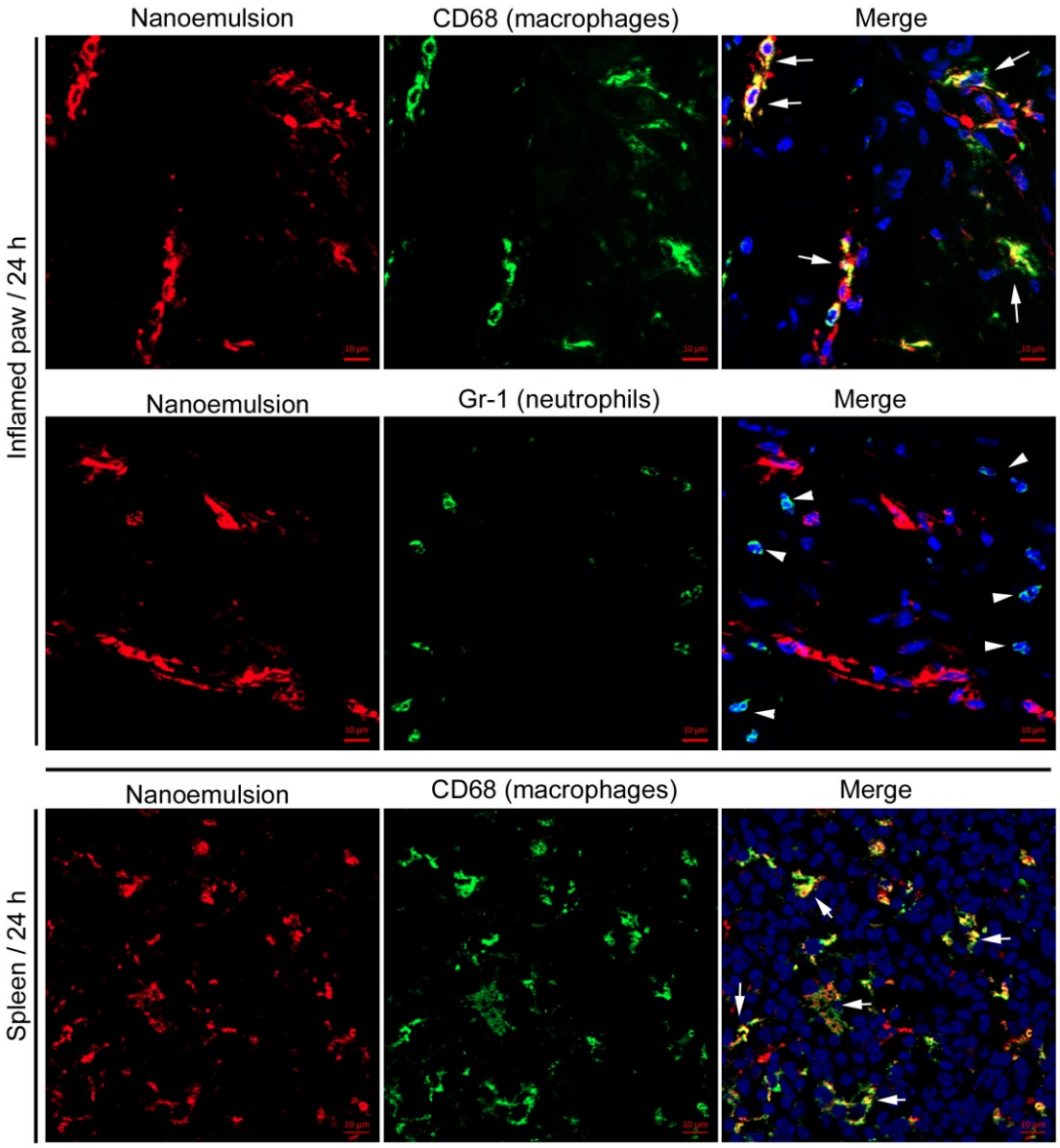

Figure 7.4. Tissue analysis for nanoemulsion accumulation in macrophages and neutrophils.

Representative immunofluorescence sections of inflamed paw and spleen from mouse injected with nanoemulsion 24 h post-inflammation. Nanoemulsion was injected 12 h pre-inflammation. Sections were stained with anti-CD68 for macrophages and anti-Gr-1 for neutrophils. Merge images shows co-localization (arrows) of the nanoemulsion (red) with macrophages (green) in inflamed paw and spleen and no co-localization (arrow head) of nanoemulsion (red) with neutrophils (green). Histology by Dr. Wissam Beaino, University of Pittsburgh, 2014.

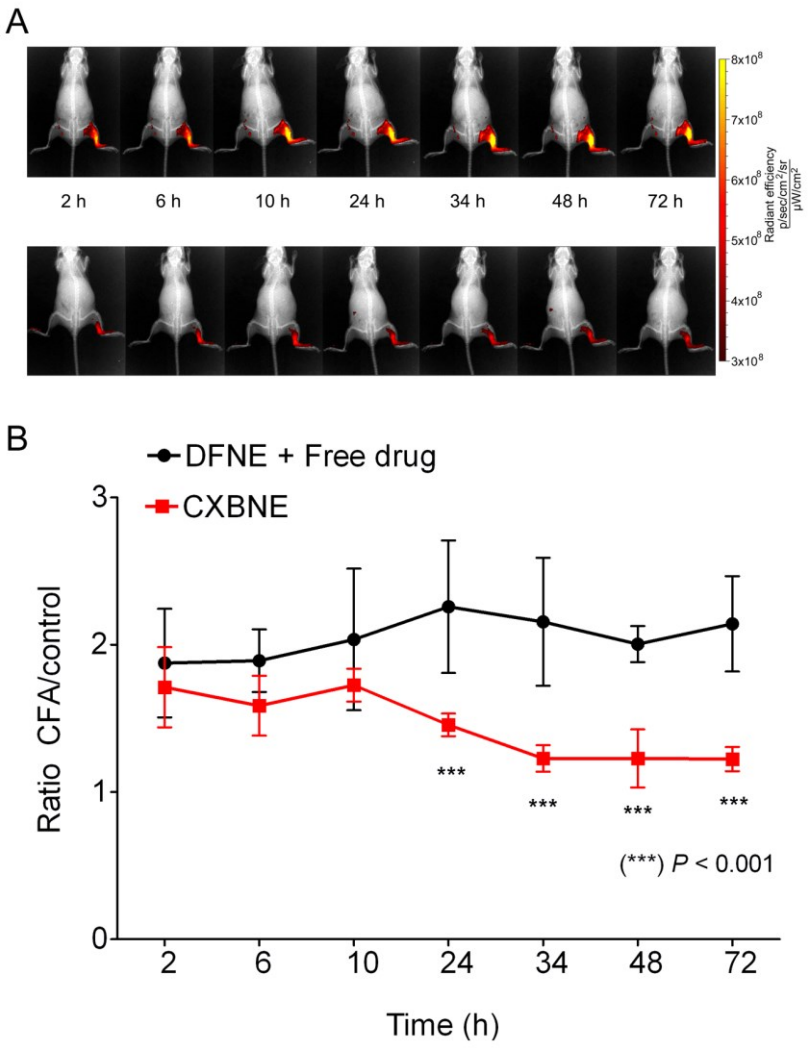

Figure 7.5. *In vivo* NIRF imaging of DFNE and CXBNE in mouse paw inflammation model.

A. Representative fluorescence/X-ray images showing the accumulation of nanoemulsion in the site of inflammation (right paw) at different time points. **B.** Ratio of quantified fluorescence of inflamed paw compared to non-inflamed paw. Data is shown as mean ± SD (n = 5).

The biodistribution study revealed that the majority of the nanoemulsion is accumulated in liver and spleen (Figure 7.6A). This result is expected because these organs are sites at which macrophages accumulate to the greatest extent. Interestingly, the

percent-injected dose accumulated in the spleen was higher for the group receiving CXBNE compared to the free drug (Figure 7.6B). Recently, it has been reported that monocytes/macrophages of spleen, in addition to blood monocytes, are recruited to the injured site during inflammation.[229] We speculate that the increased nanoemulsion-associated fluorescence in the spleen of these animals is due to the reduced recruitment of nanoemulsion-internalized monocytes/macrophages to the inflamed paw, owing to the reduced production of chemokines required for macrophage recruitment. This result also coincides with the decrease in macrophage infiltration of the inflamed paw observed in CXBNE group compared to the free drug group (Figure 7.5B).

Finally, a ^{19}F MR image of the excised paw was registered in 8 min and 32 sec as shown in Figure 7.7. A clear presence of PFPE can be seen throughout the excised paw, indicating that ^{19}F MRI can detect the nanoemulsion with increased PFPE content. Because the image was obtained in reasonable amount of time (clinically applicable time scale), nanoemulsions could be utilized for longitudinal live animal imaging using ^{19}F MRI for quantitative assessment of nanoemulsion at the inflamed site. Unlike NIRF, this method is applicable to image and quantify surface and deep tissue inflammation.

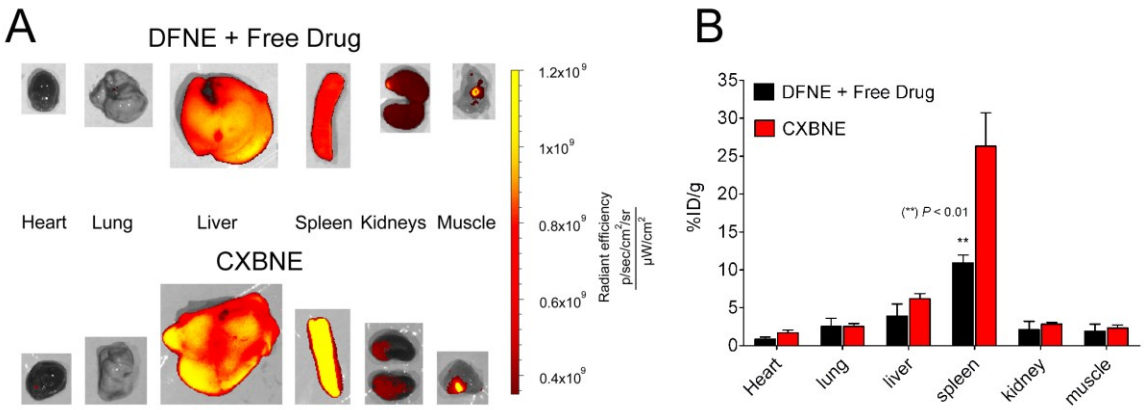

Figure 7.6. Biodistribution of DFNE and CXBNE.

A. Representative fluorescence images of different organs showing nanoemulsion biodistribution at 72 h after inducing inflammation evaluated by fluorescence *ex vivo* imaging. **B.** Biodistribution of nanoemulsion in different organs. Data is shown as mean ± SD (n = 3).

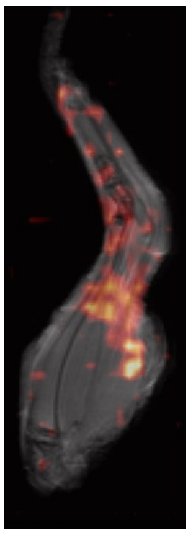

Figure 7.7. Representative $^{1}H/^{19}F$ MRI composite image of excised inflamed paw.

Images were obtained at 4 x 4 cm field of view in 8 min and 32 sec on Bruker Biospec Avance III 7-T. PFPE is seen in the paw as red hot iron signal superimposed on the anatomical ^{1}H MRI shown in grey. Image by Dr. Kevin Hitchens, Pittsburgh NMR Center for Biomedical Research, Carnegie Mellon University, 2014.

Histological analysis of the inflamed paw revealed a high level of macrophage infiltration (Figure 7.8). A majority of the nanoemulsion droplets are co-localized with macrophages (CD68+) expressing the target enzyme, COX-2. Further, CXBNE and DFNE showed accumulation specifically in macrophages compared to neutrophils (Figure 7.9), similar to the histology data from 24 h after inflammation (Figure 7.4). The combination of *in vivo* imaging and histological studies confirm that the nanoemulsion is efficiently taken up by macrophages in the inflamed tissue. *In vivo* live animal data indicate that by delivering celecoxib in a nanoemulsion, macrophage infiltration is reduced over time. We showed that the theranostic system not only delivered celecoxib to the target cells, but also facilitated the visualization of therapeutic response (reduced macrophage infiltration). Most importantly, the combined therapy and response monitoring was achieved after a single dose administration of the theranostic system. We acknowledge that the approach presented in this study utilized theranostic injection prior to inducing inflammation, which is contrary to the common mode of treatment, where therapeutic intervention ensues after the disease state is established. Prior labeling of blood monocytes was expected to facilitate visualization of these labeled monocytes fluxing to the inflamed site and reduces interference due to accumulation of nanoemulsion at the inflamed site through EPR. Yet, this approach has clinical significance, for example, to monitor macrophages in post-surgery and transplantation settings. In the next section, combined imaging and diagnostic features were demonstrated in a neuropathic pain model, which is more representative of clinical treatment setting for chronic pain.

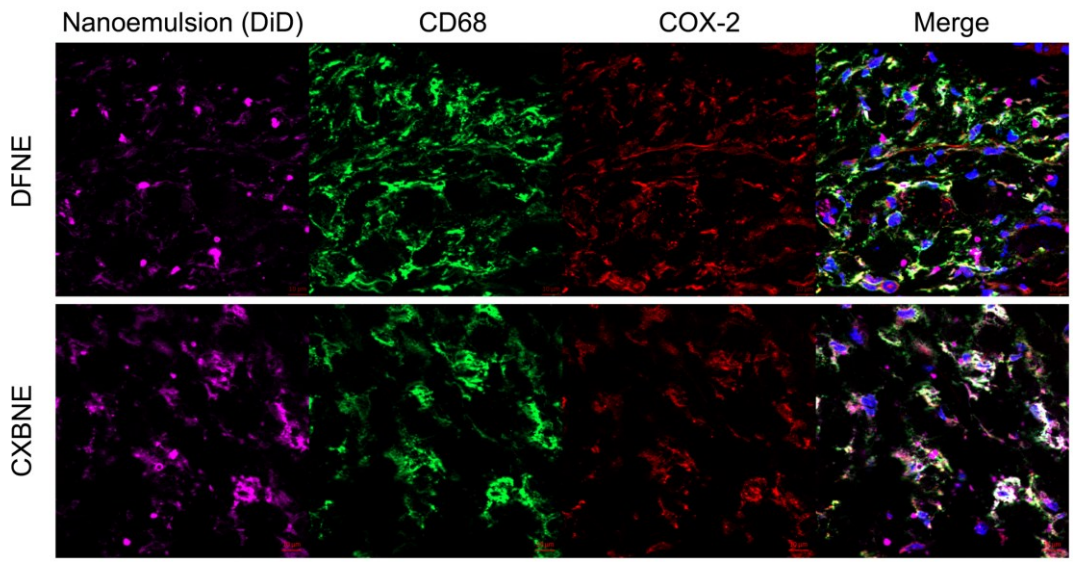

Figure 7.8. Histology of excised paw 72 h after CFA injection showing nanoemulsion accumulation in COX-2 expressing macrophages.

Representative immunofluorescence sections of inflamed paw from mouse injected with DFNE and CXBNE (purple) and stained for macrophages (Rat anti mouse-CD68, green) and COX-2 (Goat anti mouse-COX-2, red). Merged panel shows the co-localization of nanoemulsion fluorescence (DiD) with macrophages and COX-2 staining. Experiment by Dr. Wissam Beaino, University of Pittsburgh, 2014.

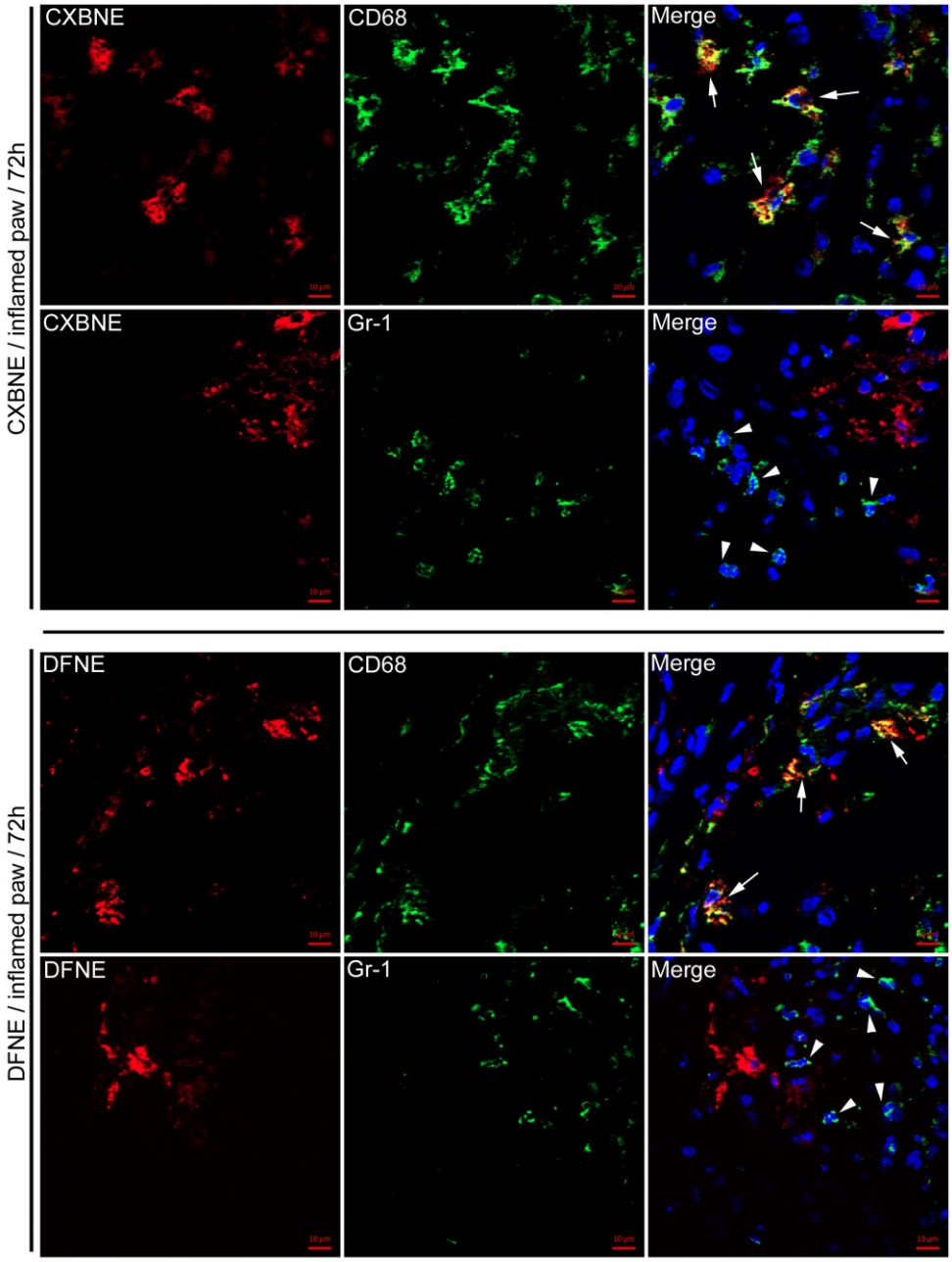

Figure 7.9. Histology of paw 72 h after inducing inflammation to assess nanoemulsion accumulation in macrophages and neutrophils.

Representative immunofluorescence sections of inflamed paw stained for macrophages (Rat anti mouse-CD68, green) or (Rat anti mouse-Gr-1-FITC, green) show nanoemulsion co-localization with macrophages (arrows), but not neutrophils (arrow head) in the merged panel.

7.3.2 *In vivo* studies in a neuropathic pain rat model

A neuropathic pain model was utilized to test the imaging potential of dual fluorescent PFPE nanoemulsion reported in chapter 5. As described in chapter 5, live animal imaging showed fluorescence at the surgical site (right sciatic nerve), but not in the contralateral side of the neuropathic pain animal (Figure 7.10). Both sciatic nerve regions of control rats were also lacking fluorescence signal. This result confirms that the nanoemulsion is specifically accumulated at the injured site. *Ex vivo* fluorescence (Figure 7.10) of the nerves also validate this result. Unfortunately, ^{19}F NMR did not detect PFPE at the inflamed site. Spleen and liver of both rats showed significant accumulation of nanoemulsion by fluorescence and ^{19}F NMR. This led to the speculation that PFPE is below the detection limits at the inflamed site in this animal model. Previously Dr. Janjic and Dr. Pollock's group[223] has employed a nanoemulsion incorporating 20% v/v PFCE for successful detection of nerve injury in this model. The results from this study were crucial to design new nanoemulsions in chapter 6 to increase ^{19}F MRI sensitivity.

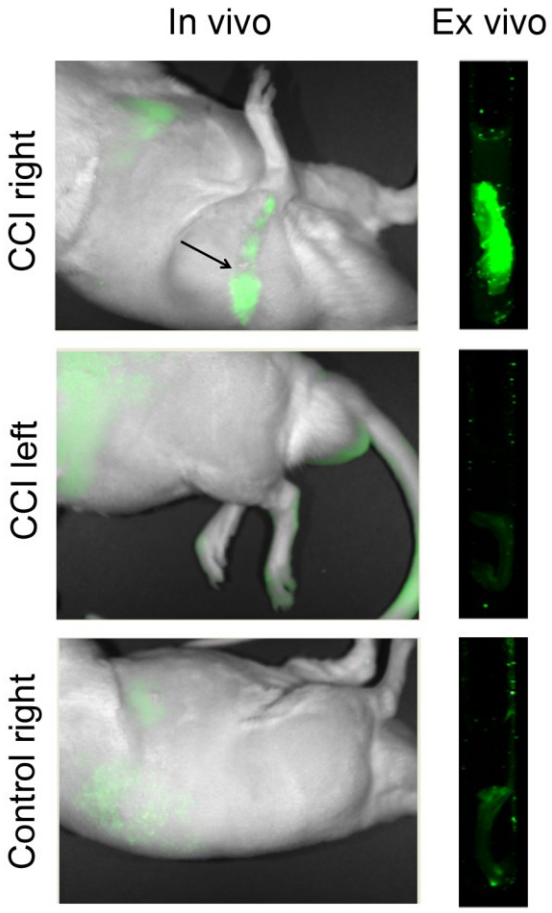

Figure 7.10. *In vivo* and *ex vivo* NIRF imaging of neuropathic pain rat model to assess dual fluorescent PFPE nanoemulsion accumulation. Arrow points to the surgical site showing fluorescence at the injured sciatic nerve in chronic constriction injury (CCI) rat.

This model was also utilized to investigate the pain sensitivity changes in response to COX-2 inhibition in macrophages using a celecoxib theranostic nanoemulsion.[215] This theranostic system is prepared with same ingredients as nanoemulsions reported in chapter 4, 5, and 6, but PFCE was utilized instead of PFPE. Animals with neuropathic pain were injected with free drug or drug-loaded or drug-free fluorescent PFCE nanoemulsions. Animals injected with free-drug also received drug-free fluorescent PFCE nanoemulsion (vehicle) to facilitate imaging. Sham animals were

used as controls for pain behavior testing. As shown in Figure 7.11, animals experienced less pain with celecoxib-loaded nanoemulsion compared to free drug and drug-free nanoemulsion starting on day 8 (2^{nd} day after nanoemulsion injection). Representative sciatic nerves (from one animal) from drug-loaded and free drug treated groups were analyzed by *ex vivo* ^{19}F NMR, ^{19}F MRI and NIRF imaging. The results from three methods show a reduction in imaging signal in the animals receiving celecoxib nanoemulsion compared to free drug. There was also a significant difference in CD68 macrophages between these groups (Kiran Vasudeva, Dissertation 2015). These results indicate that by inhibiting COX-2 in macrophages, macrophage infiltration as well as pain sensitivity will be reduced, validating the theranostic potential of the nanoemulsion in a different inflammation model.

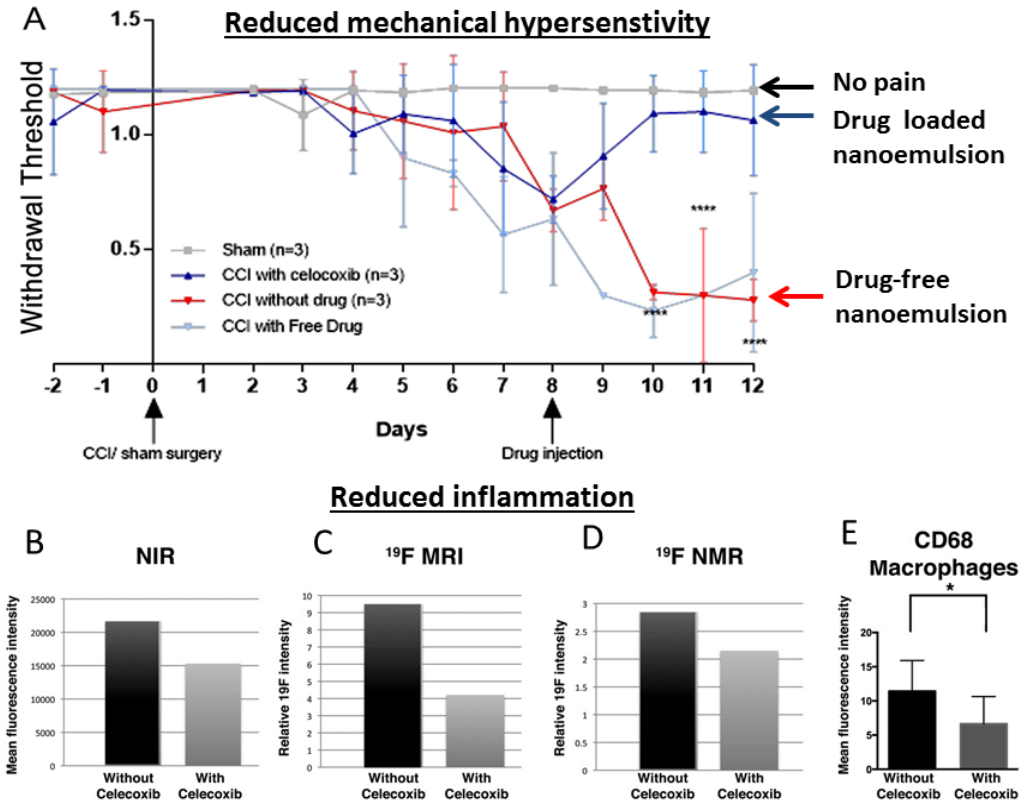

Figure 7.11. Imaging and pain behavior assessment of theranostic PFCE nanoemulsion in a neuropathic pain rat model.

A. Pain sensitivity test performed in rats with sham surgery (grey) and sciatic nerve ligation (red blue, light blue), chronic constriction injury (CCI). Mechanical hypersensitivity is quantified based on paw withdrawal in response to filament poking. Reduction in withdrawal threshold is read as increase in pain. Comparison between rats (neuropathic pain) injected with and without celecoxib-loaded theranostic using **B.** *Ex vivo* NIRF, **C.** ^{19}F MRI, **D.** ^{19}F NMR and **E.** CD68-macrophages. *Author credits: Behavior testing by Kiran Vasudeva and Muzamil Saleem, nanoemulsion designed by Dr. Jelena M. Janjic and Sravan kumar Patel, in vivo NIRF imaging, ex vivo NIRF and ^{19}F NMR by Sravan Kumar Patel, in vivo NIRF imaging by Dr. John A. Pollock, ^{19}F MRI by Dr. Kevin Hitchens, CMU, and histology for CD68 detection by Kiran Vasudeva.*

7.4 Conclusions

As hypothesized, theranostic nanoemulsions detected inflamed locus in preclinical inflammatory models. ^{19}F NMR, MRI, and fluorescence imaging methods unequivocally

confirmed the nanoemulsion presence at the inflammation site. In the mouse paw inflammation model, theranostic nanoemulsion was specifically localized to macrophages compared to neutrophils. In both inflammation models, a temporal reduction in fluorescence intensity at the inflammation site with celecoxib-nanoemulsion indicated a reduced macrophage accumulation. Further, reduced mechanical hypersensitivity as a measure of pain in response to macrophage-targeted drug delivery was observed. This result was concomitant with reduced number of macrophages and imaging signal at the injured sciatic nerve. Ultimately, the studies presented in this chapter showed that the celecoxib-loaded theranostic nanoemulsion produces anti-inflammatory effects i.e. reduced macrophage accumulation and the associated pain, while the effect can be simultaneously visualized.

8 Summary and future directions

The treatment of chronic inflammatory diseases needs a personalized approach to increase therapeutic efficacy and reduce unwanted side effects. NP-based theranostics can be effective towards driving disease management strategy to a personalized medicine realm by reducing intra- and inter-patient variability. A common aspect among several inflammatory diseases is the infiltration of macrophages that participate in disease pathogenesis. Targeting these cells for combined therapeutic and diagnostic purposes is an attractive approach applicable to multiple diseases. In this dissertation, the treatment aspects of macrophages (i.e. diagnosis and therapy) were carefully exploited to demonstrate the concept of simultaneous therapy and therapy response monitoring through the use of theranostic nanoemulsions.

The work presented in this dissertation identified that the inhibition of COX-2 in macrophages is an effective strategy for obtaining both therapeutic and diagnostic information. Furthermore, the dissertation led to the development of PFC nanoemulsions that can be utilized for therapeutic and diagnostic purposes, separately and together. A rational methodology was followed from idea conception to theranostic platform design and development, and ultimately, to *in vivo* application. In the first phase of research, lipophilic PFC conjugates were synthesized to address specific challenges in the current ^{19}F magnetic materials pertaining to MR sensitivity, body residence time and formulation challenges. After solving the instability problems, nanoemulsions with high droplet stability and macrophage labeling potential were produced. This formulation was not taken forward to *in vivo* studies due to the large time and cost investments that would be required for large-scale synthesis and pre-formulation studies. Nevertheless, this work led

to the development of a stable formulation of a new PFC conjugate. Due to its single ^{19}F resonance peak, which is easily distinguishable from the widely used PFCs, the reported nanoemulsion can be used as an imaging tracer in multi-spectral ^{19}F MRI applications. The developed platform serves as a starting point for future investigations involving drug and dye incorporation for the development of a potential theranostic system.

In the second phase of the work presented in chapters 4, 5, and 6, PFPE nanoemulsions were developed and sequentially optimized for increased MR imaging efficiency. The developed platform was amenable to the incorporation of additional dye, which can facilitate *in vivo* fluorescence and ^{19}F MR imaging as well as *ex vivo* histology. The formulation could not be detected in a neuropathic pain model using ^{19}F MR. Most likely, this was due to the low amount of PFPE in the nanoemulsion, as well as the presence of a localized low degree of inflammation. However, this formulation has the potential to be used in models with significant inflammation such as cancer and graft rejection. To address the MR sensitivity, nanoemulsions with increased PFPE content were prepared. In this multimodal theranostic platform, therapeutic and imaging functionalities were preserved in cells and tissues. In the mouse paw inflammation model, these nanoemulsions showed specific localization in macrophages (CD68+) expressing COX-2 compared to neutrophils. With a single dose administration of the celecoxib-loaded theranostic, we observed a reduction in fluorescence in the inflamed paw with time, indicating a reduction in macrophage infiltration. Essentially, infiltrating macrophages that would, otherwise, produce pro-inflammatory effects by PGE_2 release and further recruitment of blood monocytes, were converted into immunotherapeutic cells carrying theranostics. Evaluation in a neuropathic model validated our results that

the inhibition of macrophage COX-2 leads to a reduction in neuropathic pain and macrophage infiltration, which can be sensed by the theranostic nanoemulsion. Our data strongly suggest that the delivery of select agents to infiltrating macrophages can potentially lead to new inflammatory disease treatments in which macrophage behavioral changes are monitored *in vivo*. For the first time, the work presented here showed both simultaneous therapy and response monitoring after a single dose administration.

One can envision that additional inflammatory drugs could be delivered using the above-presented theranostic nanoemulsions, and that select pathways inside these cells could be inhibited or modulated for potentially therapeutic effects. Therefore, the work presented here sets the stage for a new type of inflammation treatment, with macrophages as the therapeutic and diagnostic targets. With PFCs showing ultrasound echogenic properties and suitability of the developed theranostic system for photoacoustic imaging, a suite of imaging methods could be used for noninvasive detection. The gas-dissolving capacity of PFCs could be exploited to deliver oxygen to hypoxic tumor tissue, as well as to increase sensitivity to radiation therapy. Given these functionalities, the PFC theranostic platform has great potential to be applied in varied inflammatory models. A potential future study could employ a graft rejection model to assess if pre-administration of theranostic nanoemulsion is able to reduce macrophage burden and rejection at the graft site. In addition to providing mechanistic information in preclinical pathological settings, application of these theranostics in the clinic could assist physicians in risk assessment, decision-making and strategizing treatment options leading to personalized medicine.

9 References

1. Tabas I, Glass CK 2013. Anti-inflammatory therapy in chronic disease: challenges and opportunities. Science 339(6116):166-172.
2. Patel SK, Janjic JM 2015. Macrophage targeted theranostics as personalized nanomedicine strategies for inflammatory diseases. Theranostics 5(2):150-172.
3. Nathan C 2002. Points of control in inflammation. Nature 420(6917):846-852.
4. Medzhitov R 2010. Inflammation 2010: new adventures of an old flame. Cell 140(6):771-776.
5. Hootman JM, Helmick CG, Brady TJ 2012. A public health approach to addressing arthritis in older adults: the most common cause of disability. Am J Public Health 102(3):426-433.
6. Office of Surveillance, Epidemiology and Laboratory Services (OSELS) 2011. Asthma in the US. ed.: Centers for Disease Control and Prevention. http://www.cdc.gov/VitalSigns/asthma/. Accessed: February 11 2015.
7. National Center for Chronic Disease Prevention and Health Promotion 2010. Heart disease and stroke prevention. ed.: Centers for Disease Control and Prevention. http://www.cdc.gov/chronicdisease/resources/publications/AAG/dhdsp.htm. Accessed: February 11 2015.
8. Drazen JM, Silverman EK, Lee TH 2000. Heterogeneity of therapeutic responses in asthma. Br Med Bull 56(4):1054-1070.
9. Lindberg J, af Klint E, Ulfgren A-K, Stark A, Andersson T, Nilsson P, Klareskog L, Lundeberg J 2006. Variability in synovial inflammation in rheumatoid arthritis investigated by microarray technology. Arthritis Res Ther 8(2):R47.
10. Swindell WR, Xing X, Stuart PE, Chen CS, Aphale A, Nair RP, Voorhees JJ, Elder JT, Johnston A, Gudjonsson JE 2012. Heterogeneity of inflammatory and cytokine networks in chronic plaque psoriasis. PLoS One 7(3):e34594.
11. Aaron SD, Vandemheen KL, Ramsay T, Zhang C, Avnur Z, Nikolcheva T, Quinn A 2010. Multi analyte profiling and variability of inflammatory markers in blood and induced sputum in patients with stable COPD. Respir Res 11(41):1-12.
12. Tak PP 2012. A personalized medicine approach to biologic treatment of rheumatoid arthritis: a preliminary treatment algorithm. Rheumatology (Oxford) 51(4):600-609.
13. Thurlings RM, Wijbrandts CA, Mebius RE, Cantaert T, Dinant HJ, van der Pouw-Kraan TC, Verweij CL, Baeten D, Tak PP 2008. Synovial lymphoid neogenesis does not define a specific clinical rheumatoid arthritis phenotype. Arthritis Rheum 58(6):1582-1589.
14. van der Maas A, van den Bemt BJ, Wolbink G, van den Hoogen FH, van Riel PL, den Broeder AA 2012. Low infliximab serum trough levels and anti-infliximab antibodies are prevalent in rheumatoid arthritis patients treated with infliximab in daily clinical practice: results of an observational cohort study. BMC Musculoskelet Disord 13(1):184.
15. Bendtzen K, Geborek P, Svenson M, Larsson L, Kapetanovic MC, Saxne T 2006. Individualized monitoring of drug bioavailability and immunogenicity in rheumatoid arthritis patients treated with the tumor necrosis factor alpha inhibitor infliximab. Arthritis Rheum 54(12):3782-3789.

16. Lethbridge-Cejku M, Schiller JS, Bernadel L 2004. Summary health statistics for U.S. adults: National Health Interview Survey, 2002. Vital Health Stat 10 (222):1-151.
17. Blackwell DL, Lucas JW, Clarke TC 2014. Summary health statistics for U.S. adults: national health interview survey, 2012. Vital Health Stat 10 (260):1-161.
18. Mura S, Couvreur P 2012. Nanotheranostics for personalized medicine. Adv Drug Deliver Rev 64(13):1394-1416.
19. U.S. Food and Drug Administration 2013. Paving the way for personalized medicine: FDA's role in a rew era of medical product development. ed., U.S. Food and Drug Administration. http://www.fda.gov/downloads/ScienceResearch/SpecialTopics/PersonalizedMedicine/UCM372421.pdf. Accessed: March 17 2015.
20. Gajria D, Chandarlapaty S 2011. HER2-amplified breast cancer: mechanisms of trastuzumab resistance and novel targeted therapies. Expert Rev Anticancer Ther 11(2):263-275.
21. Pene F, Courtine E, Cariou A, Mira J-P 2009. Toward theragnostics. Crit Care Med 37(1):S50-S58.
22. Janib SM, Moses AS, MacKay JA 2010. Imaging and drug delivery using theranostic nanoparticles. Adv Drug Deliver Rev 62(11):1052-1063.
23. Couvreur P 2013. Nanoparticles in drug delivery: past, present and future. Adv Drug Deliver Rev 65(1):21-23.
24. Ganta S, Devalapally H, Shahiwala A, Amiji M 2008. A review of stimuli-responsive nanocarriers for drug and gene delivery. J Control Release 126(3):187-204.
25. Fang J, Nakamura H, Maeda H 2011. The EPR effect: unique features of tumor blood vessels for drug delivery, factors involved, and limitations and augmentation of the effect. Adv Drug Deliver Rev 63(3):136-151.
26. Jain S, Amiji M. 2012. Macrophage-targeted nanoparticle delivery systems. In Svenson S, Prud'homme R, editors. Multifunctional Nanoparticles for Drug Delivery Applications, ed.: Springer. p 47-83.
27. Kao YH, Tan EH, Lim KY, Ng CE, Goh SW 2012. Yttrium-90 internal pair production imaging using first generation PET/CT provides high-resolution images for qualitative diagnostic purposes. Br J Radiol 85(1015):1018-1019.
28. Raval M, Bande D, Pillai AK, Blaszkowsky LS, Ganguli S, Beg MS, Kalva SP 2014. Yttrium-90 radioembolization of hepatic metastases from colorectal cancer. Front Oncol 4(120):1-8.
29. Hamilton JA, Tak PP 2009. The dynamics of macrophage lineage populations in inflammatory and autoimmune diseases. Arthritis Rheum 60(5):1210-1221.
30. van der Heijden JW, Dijkmans BA, Scheper RJ, Jansen G 2007. Drug Insight: resistance to methotrexate and other disease-modifying antirheumatic drugs--from bench to bedside. Nat Clin Pract Rheumatol 3(1):26-34.
31. Moore T, Chen H, Morrison R, Wang F, Anker JN, Alexis F 2014. Nanotechnologies for noninvasive measurement of drug release. Mol Pharm 11(1):24-39.
32. Ahsan F, Rivas IP, Khan MA, Torres Suárez AI 2002. Targeting to macrophages: role of physicochemical properties of particulate carriers—liposomes and microspheres—on the phagocytosis by macrophages. J Control Release 79(1):29-40.
33. Hawkey C 1999. COX-2 inhibitors. Lancet 353(9149):307-314.

34. Antoniou K, Malamas M, Drosos AA 2007. Clinical pharmacology of celecoxib, a COX-2 selective inhibitor. Expert Opin Pharmacother 8(11):1719-1732.
35. Jacob S, Laury-Kleintop L, Lanza-Jacoby S 2008. The select cyclooxygenase-2 inhibitor celecoxib reduced the extent of atherosclerosis in apo E-/-mice. J Surg Res 146(1):135-142.
36. Jendrossek V 2013. Targeting apoptosis pathways by celecoxib in cancer. Cancer Lett 332(2):313-324.
37. Raval M, Frank PG, Laury-Kleintop L, Yan G, Lanza-Jacoby S 2010. Celecoxib combined with atorvastatin prevents progression of atherosclerosis. J Surg Res 163(2):e113-e122.
38. Reddy BS, Hirose Y, Lubet R, Steele V, Kelloff G, Paulson S, Seibert K, Rao CV 2000. Chemoprevention of colon cancer by specific cyclooxygenase-2 inhibitor, celecoxib, administered during different stages of carcinogenesis. Cancer Res 60(2):293-297.
39. Sanchez-Pernaute R, Ferree A, Cooper O, Yu M, Brownell AL, Isacson O 2004. Selective COX-2 inhibition prevents progressive dopamine neuron degeneration in a rat model of Parkinson's disease. J Neuroinflammation 1(6):1-11.
40. Wang K, Tarakji K, Zhou Z, Zhang M, Forudi F, Zhou X, Koki AT, Smith ME, Keller BT, Topol EJ 2005. Celecoxib, a selective cyclooxygenase-2 inhibitor, decreases monocyte chemoattractant protein-1 expression and neointimal hyperplasia in the rabbit atherosclerotic balloon injury model. J Cardiovasc Pharmacol 45(1):61-67.
41. Amrite A, Pugazhenthi V, Cheruvu N, Kompella U 2010. Delivery of celecoxib for treating diseases of the eye: influence of pigment and diabetes. Expert Opin Drug Deliv 7(5):631-645.
42. Amrite AC, Ayalasomayajula SP, Cheruvu NP, Kompella UB 2006. Single periocular injection of celecoxib-PLGA microparticles inhibits diabetes-induced elevations in retinal PGE2, VEGF, and vascular leakage. Invest Ophthalmol Vis Sci 47(3):1149-1160.
43. Baboota S, Faiyaz S, Ahuja A, Ali J, Shafiq S, Ahmad S 2007. Development and validation of a stability-indicating HPLC method for analysis of celecoxib (CXB) in bulk drug and microemulsion formulations. Acta Chromatogr 18:116-129.
44. Soliman SM, Abdel Malak NS, El-Gazayerly ON, Abdel Rehim A 2010. Formulation of microemulsion gel systems for transdermal delivery of celecoxib: In vitro permeation, anti-inflammatory activity and skin irritation tests. Drug Discov Ther 4(6):459-471.
45. Thakkar H, Sharma RK, Mishra AK, Chuttani K, Murthy RR 2005. Albumin microspheres as carriers for the antiarthritic drug celecoxib. AAPS PharmSciTech 6(1):E65-E73.
46. Venkatesan P, Puvvada N, Dash R, Prashanth Kumar B, Sarkar D, Azab B, Pathak A, Kundu SC, Fisher PB, Mandal M 2011. The potential of celecoxib-loaded hydroxyapatite-chitosan nanocomposite for the treatment of colon cancer. Biomaterials 32(15):3794-3806.
47. Fujiwara N, Kobayashi K 2005. Macrophages in inflammation. Curr Drug Targets Inflamm Allergy 4(3):281-286.
48. Yang C, Nilsson L, Cheema MU, Wang Y, Frokiaer J, Gao S, Kjems J, Norregaard R 2015. Chitosan/siRNA nanoparticles targeting cyclooxygenase type 2

attenuate unilateral ureteral obstruction-induced kidney injury in mice. Theranostics 5(2):110-123.
49. Chen EP. 2014. Augmenting anti-tumor immunity by targeting macrophage COX-2 in breast cancer. ed., Publicly Accessible Penn Dissertations: University of Pennsylvania. p 1-157.
50. Muller WA 2013. Getting leukocytes to the site of inflammation. Vet Pathol 50(1):7-22.
51. Medzhitov R 2008. Origin and physiological roles of inflammation. Nature 454(7203):428-435.
52. Murray PJ, Wynn TA 2011. Protective and pathogenic functions of macrophage subsets. Nat Rev Immunol 11(11):723-737.
53. Geissmann F, Manz MG, Jung S, Sieweke MH, Merad M, Ley K 2010. Development of monocytes, macrophages, and dendritic cells. Science 327(5966):656-661.
54. Kinne RW, Stuhlmüller B, Burmester G-R 2007. Cells of the synovium in rheumatoid arthritis. Macrophages. Arthritis Res Ther 9(6):224.
55. Tesch G 2007. Role of macrophages in complications of type 2 diabetes. Clin Exp Pharmacol Physiol 34(10):1016-1019.
56. Glass CK 2002. The macrophage foam cell as a target for therapeutic intervention. Nat Med 8(11):1235-1242.
57. Baay M, Brouwer A, Pauwels P, Peeters M, Lardon F 2011. Tumor cells and tumor-associated macrophages: secreted proteins as potential targets for therapy. Clin Dev Immunol 2011:1-12.
58. Boorsma CE, Draijer C, Melgert BN 2013. Macrophage heterogeneity in respiratory diseases. Mediators Inflamm 2013:1-19.
59. Gate D, Rezai-Zadeh K, Jodry D, Rentsendorj A, Town T 2010. Macrophages in Alzheimer's disease: the blood-borne identity. J Neural Transm 117(8):961-970.
60. Sica A, Mantovani A 2012. Macrophage plasticity and polarization: in vivo veritas. J Clin Invest 122(3):787-795.
61. Mantovani A, Bottazzi B, Colotta F, Sozzani S, Ruco L 1992. The origin and function of tumor-associated macrophages. Immunol Today 13(7):265-270.
62. Libby P, Ridker PM, Maseri A 2002. Inflammation and atherosclerosis. Circulation 105(9):1135-1143.
63. Gui T, Shimokado A, Sun Y, Akasaka T, Muragaki Y 2012. Diverse roles of macrophages in atherosclerosis: from inflammatory biology to biomarker discovery. Mediators Inflamm 2012:1-14.
64. Weissleder R, Nahrendorf M, Pittet MJ 2014. Imaging macrophages with nanoparticles. Nat Mater 13(2):125-138.
65. Trivedi RA, Mallawarachi C, JM UK-I, Graves MJ, Horsley J, Goddard MJ, Brown A, Wang L, Kirkpatrick PJ, Brown J, Gillard JH 2006. Identifying inflamed carotid plaques using in vivo USPIO-enhanced MR imaging to label plaque macrophages. Arterioscler Thromb Vasc Biol 26(7):1601-1606.
66. Yilmaz A, Dengler MA, van der Kuip H, Yildiz H, Rösch S, Klumpp S, Klingel K, Kandolf R, Helluy X, Hiller K-H 2013. Imaging of myocardial infarction using ultrasmall superparamagnetic iron oxide nanoparticles: a human study using a multi-

parametric cardiovascular magnetic resonance imaging approach. Eur Heart J 34(6):462-475.
67. Gaglia JL, Guimaraes AR, Harisinghani M, Turvey SE, Jackson R, Benoist C, Mathis D, Weissleder R 2011. Noninvasive imaging of pancreatic islet inflammation in type 1A diabetes patients. J Clin Invest 121(1):442.
68. Van Der Laken CJ, Elzinga EH, Kropholler MA, Molthoff CF, van der Heijden JW, Maruyama K, Boellaard R, Dijkmans BA, Lammertsma AA, Voskuyl AE 2008. Noninvasive imaging of macrophages in rheumatoid synovitis using 11C-(R)-PK11195 and positron emission tomography. Arthritis Rheum 58(11):3350-3355.
69. Tang TY, Howarth SP, Miller SR, Graves MJ, Patterson AJ, Jean-Marie U, Li ZY, Walsh SR, Brown AP, Kirkpatrick PJ 2009. The ATHEROMA (Atorvastatin Therapy: Effects on Reduction of Macrophage Activity) Study: evaluation using ultrasmall superparamagnetic iron oxide-enhanced magnetic resonance imaging in carotid disease. J Am Coll Cardiol 53(22):2039-2050.
70. Lameijer MA, Tang J, Nahrendorf M, Beelen RH, Mulder WJ 2013. Monocytes and macrophages as nanomedicinal targets for improved diagnosis and treatment of disease. Expert Rev Mol Diagn 13(6):567-580.
71. Chellat F, Merhi Y, Moreau A, Yahia LH 2005. Therapeutic potential of nanoparticulate systems for macrophage targeting. Biomaterials 26(35):7260-7275.
72. Frohlich E 2012. The role of surface charge in cellular uptake and cytotoxicity of medical nanoparticles. Int J Nanomedicine 7:5577-5591.
73. Kelly C, Jefferies C, Cryan SA 2011. Targeted liposomal drug delivery to monocytes and macrophages. J Drug Deliv 2011:1-11.
74. Yu SS, Lau CM, Thomas SN, Jerome WG, Maron DJ, Dickerson JH, Hubbell JA, Giorgio TD 2012. Size- and charge-dependent non-specific uptake of PEGylated nanoparticles by macrophages. Int J Nanomedicine 7:799-813.
75. Jokerst JV, Lobovkina T, Zare RN, Gambhir SS 2011. Nanoparticle PEGylation for imaging and therapy. Nanomedicine (Lond) 6(4):715-728.
76. Thomas TP, Goonewardena SN, Majoros IJ, Kotlyar A, Cao Z, Leroueil PR, Baker JR 2011. Folate-targeted nanoparticles show efficacy in the treatment of inflammatory arthritis. Arthritis Rheum 63(9):2671-2680.
77. Chen WC, Kawasaki N, Nycholat CM, Han S, Pilotte J, Crocker PR, Paulson JC 2012. Antigen delivery to macrophages using liposomal nanoparticles targeting sialoadhesin/CD169. PLoS One 7(6):e39039.
78. Jain S, Doshi AS, Iyer AK, Amiji MM 2013. Multifunctional nanoparticles for targeting cancer and inflammatory diseases. J Drug Target 21(10):888-903.
79. Buch MH, Conaghan PG, Quinn MA, Bingham SJ, Veale D, Emery P 2004. True infliximab resistance in rheumatoid arthritis: a role for lymphotoxin α? Ann Rheum Dis 63(10):1344-1346.
80. Szefler S, Leung D 1997. Glucocorticoid-resistant asthma: pathogenesis and clinical implications for management. Eur Respir J 10(7):1640-1647.
81. Cailhier JF, Partolina M, Vuthoori S, Wu S, Ko K, Watson S, Savill J, Hughes J, Lang RA 2005. Conditional macrophage ablation demonstrates that resident macrophages initiate acute peritoneal inflammation. J Immunol 174(4):2336-2342.
82. Mirza R, DiPietro LA, Koh TJ 2009. Selective and specific macrophage ablation is detrimental to wound healing in mice. Am J Pathol 175(6):2454-2462.

83. Verheye S, Martinet W, Kockx MM, Knaapen MW, Salu K, Timmermans J-P, Ellis JT, Kilpatrick DL, De Meyer GR 2007. Selective clearance of macrophages in atherosclerotic plaques by autophagy. J Am Coll Cardiol 49(6):706-715.
84. Danenberg HD, Fishbein I, Gao J, Mönkkönen J, Reich R, Gati I, Moerman E, Golomb G 2002. Macrophage depletion by clodronate-containing liposomes reduces neointimal formation after balloon injury in rats and rabbits. Circulation 106(5):599-605.
85. Barrera P, Blom A, Van Lent PL, Van Bloois L, Beijnen JH, Van Rooijen N, De Waal Malefijt MC, Van De Putte L, Storm G, Van Den Berg WB 2000. Synovial macrophage depletion with clodronate-containing liposomes in rheumatoid arthritis. Arthritis Rheum 43(9):1951-1959.
86. Zeisberger S, Odermatt B, Marty C, Zehnder-Fjällman A, Ballmer-Hofer K, Schwendener R 2006. Clodronate-liposome-mediated depletion of tumour-associated macrophages: a new and highly effective antiangiogenic therapy approach. Br J Cancer 95(3):272-281.
87. Celli JP, Spring BQ, Rizvi I, Evans CL, Samkoe KS, Verma S, Pogue BW, Hasan T 2010. Imaging and photodynamic therapy: mechanisms, monitoring, and optimization. Chem Rev 110(5):2795-2838.
88. Rai P, Mallidi S, Zheng X, Rahmanzadeh R, Mir Y, Elrington S, Khurshid A, Hasan T 2010. Development and applications of photo-triggered theranostic agents. Adv Drug Deliver Rev 62(11):1094-1124.
89. Schmitt F, Lagopoulos L, Käuper P, Rossi N, Busso N, Barge J, Wagnières G, Laue C, Wandrey C, Juillerat-Jeanneret L 2010. Chitosan-based nanogels for selective delivery of photosensitizers to macrophages and improved retention in and therapy of articular joints. J Control Release 144(2):242-250.
90. McCarthy JR, Jaffer FA, Weissleder R 2006. A macrophage-targeted theranostic nanoparticle for biomedical applications. Small 2(8-9):983-987.
91. McCarthy JR, Korngold E, Weissleder R, Jaffer FA 2010. A light-activated theranostic nanoagent for targeted macrophage ablation in inflammatory atherosclerosis. Small 6(18):2041-2049.
92. Shon S-M, Choi Y, Kim J-Y, Lee DK, Park J-Y, Schellingerhout D, Kim D-E 2013. Photodynamic therapy using a protease-mediated theranostic agent reduces cathepsin-B activity in mouse atheromata in vivo. Arterioscler Thromb Vasc Biol 33(6):1360-1365.
93. Kosuge H, Sherlock SP, Kitagawa T, Dash R, Robinson JT, Dai H, McConnell MV 2012. Near infrared imaging and photothermal ablation of vascular inflammation using single-walled carbon nanotubes. J Am Heart Assoc 1(6):e002568.
94. Choi R, Yang J, Choi J, Lim E-K, Kim E, Suh J-S, Huh Y-M, Haam S 2010. Thiolated dextran-coated gold nanorods for photothermal ablation of inflammatory macrophages. Langmuir 26(22):17520-17527.
95. Ma LL, Feldman MD, Tam JM, Paranjape AS, Cheruku KK, Larson TA, Tam JO, Ingram DR, Paramita V, Villard JW 2009. Small multifunctional nanoclusters (nanoroses) for targeted cellular imaging and therapy. ACS Nano 3(9):2686-2696.
96. Pissuwan D, Valenzuela SM, Killingsworth MC, Xu X, Cortie MB 2007. Targeted destruction of murine macrophage cells with bioconjugated gold nanorods. J Nanopart Res 9(6):1109-1124.

97. Chakravarthy KV, Davidson BA, Helinski JD, Ding H, Law W-C, Yong K-T, Prasad PN, Knight PR 2011. Doxorubicin-conjugated quantum dots to target alveolar macrophages and inflammation. Nanomedicine 7(1):88-96.
98. Kluza E, Yeo SY, Schmid S, Van der Schaft DW, Boekhoven RW, Schiffelers RM, Storm G, Strijkers GJ, Nicolay K 2011. Anti-tumor activity of liposomal glucocorticoids: the relevance of liposome-mediated drug delivery, intratumoral localization and systemic activity. J Control Release 151(1):10-17.
99. Ragheb RR, Kim D, Bandyopadhyay A, Chahboune H, Bulutoglu B, Ezaldein H, Criscione JM, Fahmy TM 2013. Induced clustered nanoconfinement of superparamagnetic iron oxide in biodegradable nanoparticles enhances transverse relaxivity for targeted theranostics. Magn Reson Med 70(6):1748-1760.
100. Tracy E, Bowman M, Henderson B, Baumann H 2012. Interleukin-1α is the major alarmin of lung epithelial cells released during photodynamic therapy to induce inflammatory mediators in fibroblasts. Br J Cancer 107(9):1534-1546.
101. Harel-Adar T, Mordechai TB, Amsalem Y, Feinberg MS, Leor J, Cohen S 2011. Modulation of cardiac macrophages by phosphatidylserine-presenting liposomes improves infarct repair. Proc Natl Acad Sci 108(5):1827-1832.
102. Nakanishi Y, Nakatsuji M, Seno H, Ishizu S, Akitake-Kawano R, Kanda K, Ueo T, Komekado H, Kawada M, Minami M 2011. COX-2 inhibition alters the phenotype of tumor-associated macrophages from M2 to M1 in ApcMin/+ mouse polyps. Carcinogenesis 32(9):1333-1339.
103. Shen J, Chelvam V, Cresswell G, Low PS 2013. Use of folate-conjugated imaging agents to target alternatively activated macrophages in a murine model of asthma. Mol Pharm 10(5):1918-1927.
104. Melancon MP, Lu W, Huang Q, Thapa P, Zhou D, Ng C, Li C 2010. Targeted imaging of tumor-associated M2 macrophages using a macromolecular contrast agent PG-Gd-NIR813. Biomaterials 31(25):6567-6573.
105. Leuschner F, Dutta P, Gorbatov R, Novobrantseva TI, Donahoe JS, Courties G, Lee KM, Kim JI, Markmann JF, Marinelli B 2011. Therapeutic siRNA silencing in inflammatory monocytes in mice. Nat Biotechnol 29(11):1005-1010.
106. Aouadi M, Tesz GJ, Nicoloro SM, Wang M, Soto E, Ostroff GR, Czech MP 2009. Orally delivered siRNA targeting macrophage Map4k4 suppresses systemic inflammation. Nature 458(7242):1180-1184.
107. Yin L, Song Z, Qu Q, Kim KH, Zheng N, Yao C, Chaudhury I, Tang H, Gabrielson NP, Uckun FM, Cheng J 2013. Supramolecular self-assembled nanoparticles mediate oral delivery of therapeutic TNF-alpha siRNA against systemic inflammation. Angew Chem Int Ed Engl 52(22):5757-5761.
108. Komano Y, Yagi N, Onoue I, Kaneko K, Miyasaka N, Nanki T 2012. Arthritic joint-targeting small interfering RNA-encapsulated liposome: implication for treatment strategy for rheumatoid arthritis. J Pharmacol Exp Ther 340(1):109-113.
109. Cho S, Hwang O, Lee I, Lee G, Yoo D, Khang G, Kang PM, Lee D 2012. Chemiluminescent and antioxidant micelles as theranostic agents for hydrogen peroxide associated-inflammatory diseases. Adv Funct Mater 22(19):4038-4043.
110. Maiseyeu A, Badgeley MA, Kampfrath T, Mihai G, Deiuliis JA, Liu C, Sun Q, Parthasarathy S, Simon DI, Croce K 2012. In vivo targeting of inflammation-associated

myeloid-related protein 8/14 via gadolinium immunonanoparticles. Arterioscler Thromb Vasc Biol 32(4):962-970.
111. Esposito E, Cuzzocrea S 2009. TNF-alpha as a therapeutic target in inflammatory diseases, ischemia-reperfusion injury and trauma. Curr Med Chem 16(24):3152-3167.
112. Tobinick E, Gross H, Weinberger A, Cohen H 2006. TNF-alpha modulation for treatment of Alzheimer's disease: a 6-month pilot study. MedGenMed 8(2):25.
113. Schellekens H 2005. Follow-on biologics: challenges of the 'next generation'. Nephrol Dial Transplant 20(suppl 4):iv31-iv36.
114. Rajakariar R, Yaqoob MM, Gilroy DW 2006. COX-2 in inflammation and resolution. Mol Interv 6(4):199.
115. Lipsky PE, Brooks P, Crofford LJ, DuBois R, Graham D, Simon LS, van de Putte LB, Abramson SB 2000. Unresolved issues in the role of cyclooxygenase-2 in normal physiologic processes and disease. Arch Intern Med 160(7):913-920.
116. Kalinski P 2012. Regulation of immune responses by prostaglandin E2. J Immunol 188(1):21-28.
117. Park TY, Baik EJ, Lee SH 2013. Prostaglandin E(2)-induced intercellular adhesion molecule-1 expression is mediated by cAMP/Epac signalling modules in bEnd.3 brain endothelial cells. Br J Pharmacol 169(3):604-618.
118. Tajima T, Murata T, Aritake K, Urade Y, Hirai H, Nakamura M, Ozaki H, Hori M 2008. Lipopolysaccharide induces macrophage migration via prostaglandin D(2) and prostaglandin E(2). J Pharmacol Exp Ther 326(2):493-501.
119. Uddin MJ, Crews BC, Blobaum AL, Kingsley PJ, Gorden DL, McIntyre JO, Matrisian LM, Subbaramaiah K, Dannenberg AJ, Piston DW 2010. Selective visualization of cyclooxygenase-2 in inflammation and cancer by targeted fluorescent imaging agents. Cancer Res 70(9):3618-3627.
120. Uddin MJ, Crews BC, Ghebreselasie K, Huda I, Kingsley PJ, Ansari MS, Tantawy MN, Reese J, Marnett LJ 2011. Fluorinated COX-2 inhibitors as agents in PET imaging of inflammation and cancer. Cancer Prev Res 4(10):1536-1545.
121. Anderson GD, Hauser SD, McGarity KL, Bremer ME, Isakson PC, Gregory SA 1996. Selective inhibition of cyclooxygenase (COX)-2 reverses inflammation and expression of COX-2 and interleukin 6 in rat adjuvant arthritis. J Clin Invest 97(11):2672.
122. Markosyan N, Chen EP, Smyth EM 2014. Targeting COX-2 abrogates mammary tumorigenesis: Breaking cancer-associated suppression of immunosurveillance. Oncoimmunology 3:e29287.
123. Solomon SD, McMurray JJ, Pfeffer MA, Wittes J, Fowler R, Finn P, Anderson WF, Zauber A, Hawk E, Bertagnolli M 2005. Cardiovascular risk associated with celecoxib in a clinical trial for colorectal adenoma prevention. N Engl J Med 352(11):1071-1080.
124. Thun MJ, Henley SJ, Patrono C 2002. Nonsteroidal anti-inflammatory drugs as anticancer agents: mechanistic, pharmacologic, and clinical issues. J Natl Cancer Inst 94(4):252-266.
125. Linton MF, Fazio S 2004. Cyclooxygenase-2 and inflammation in atherosclerosis. Curr Opin Pharmacol 4(2):116-123.

126. Fiala M, Liu Q, Sayre J, Pop V, Brahmandam V, Graves M, Vinters H 2002. Cyclooxygenase-2-positive macrophages infiltrate the Alzheimer's disease brain and damage the blood–brain barrier. Eur J Clin Invest 32(5):360-371.
127. Teismann P, Tieu K, Choi D-K, Wu D-C, Naini A, Hunot S, Vila M, Jackson-Lewis V, Przedborski S 2003. Cyclooxygenase-2 is instrumental in Parkinson's disease neurodegeneration. Proc Natl Acad Sci 100(9):5473-5478.
128. Patel SK, Zhang Y, Pollock JA, Janjic JM 2013. Cyclooxgenase-2 inhibiting perfluoropoly (ethylene glycol) ether theranostic nanoemulsions-in vitro study. PLoS One 8(2):e55802.
129. Kreuzer J, Denger S, Jahn L, Bader J, Ritter K, von Hodenberg E, Kübler W 1996. LDL stimulates chemotaxis of human monocytes through a cyclooxygenase-dependent pathway. Arterioscler Thromb Vasc Biol 16(12):1481-1487.
130. Chen L, Yang G, Monslow J, Todd L, Cormode DP, Tang J, Grant GR, DeLong JH, Tang SY, Lawson JA, Pure E, Fitzgerald GA 2014. Myeloid cell microsomal prostaglandin E synthase-1 fosters atherogenesis in mice. Proc Natl Acad Sci U S A 111(18):6828-6833.
131. Chen EP, Markosyan N, Connolly E, Lawson JA, Li X, Grant GR, Grosser T, FitzGerald GA, Smyth EM 2014. Myeloid Cell COX-2 deletion reduces mammary tumor growth through enhanced cytotoxic T-lymphocyte function. Carcinogenesis 35(8):1788-1797.
132. Seedher N, Bhatia S 2003. Solubility enhancement of Cox-2 inhibitors using various solvent systems. AAPS PharmSciTech 4(3):36-44.
133. Paulson SK, Vaughn MB, Jessen SM, Lawal Y, Gresk CJ, Yan B, Maziasz TJ, Cook CS, Karim A 2001. Pharmacokinetics of celecoxib after oral administration in dogs and humans: effect of food and site of absorption. J Pharmacol Exp Ther 297(2):638-645.
134. Paulson SK, Zhang JY, Breau AP, Hribar JD, Liu NW, Jessen SM, Lawal YM, Cogburn JN, Gresk CJ, Markos CS 2000. Pharmacokinetics, tissue distribution, metabolism, and excretion of celecoxib in rats. Drug Metab Dispos 28(5):514-521.
135. Howe LR, Subbaramaiah K, Patel J, Masferrer JL, Deora A, Hudis C, Thaler HT, Muller WJ, Du B, Brown AM 2002. Celecoxib, a selective cyclooxygenase 2 inhibitor, protects against human epidermal growth factor receptor 2 (HER-2)/neu-induced breast cancer. Cancer Res 62(19):5405-5407.
136. Harris R 2009. Cyclooxygenase-2 (cox-2) blockade in the chemoprevention of cancers of the colon, breast, prostate, and lung. Inflammopharmacology 17(2):55-67.
137. Grosser T, Fries S, FitzGerald GA 2006. Biological basis for the cardiovascular consequences of COX-2 inhibition: therapeutic challenges and opportunities. J Clin Invest 116(1):4-15.
138. Cooper DL, Harirforoosh S 2014. Effect of formulation variables on preparation of celecoxib loaded polylactide-co-glycolide nanoparticles. PLoS One 9(12):e113558.
139. Erdog A, Putra Limasale YD, Keskin D, Tezcaner A, Banerjee S 2013. In vitro characterization of a liposomal formulation of celecoxib containing 1,2-distearoyl-sn-glycero-3-phosphocholine, cholesterol, and polyethylene glycol and its functional effects against colorectal cancer cell lines. J Pharm Sci 102(10):3666-3677.

140. Limasale YD, Tezcaner A, Ozen C, Keskin D, Banerjee S 2015. Epidermal growth factor receptor-targeted immunoliposomes for delivery of celecoxib to cancer cells. Int J Pharm 479(2):364-373.
141. Shakeel F, Baboota S, Ahuja A, Ali J, Shafiq S 2008. Celecoxib nanoemulsion: Skin permeation mechanism and bioavailability assessment. J Drug Target 16(10):733-740.
142. Krafft MP, Riess JG 2009. Chemistry, physical chemistry, and uses of molecular fluorocarbon--hydrocarbon diblocks, triblocks, and related compounds--unique "apolar" components for self-assembled colloid and interface engineering. Chem Rev 109(5):1714-1792.
143. Krafft MP, Riess JG 2007. Perfluorocarbons: Life sciences and biomedical uses Dedicated to the memory of Professor Guy Ourisson, a true RENAISSANCE man. J Polym Sci A Polym Chem 45(7):1185-1198.
144. Mattrey RF 1989. Perfluorooctylbromide: a new contrast agent for CT, sonography, and MR imaging. Am J Roentgenol 152(2):247-252.
145. Tatum JL, Kelloff GJ, Gillies RJ, Arbeit JM, Brown JM, Chao KS, Chapman JD, Eckelman WC, Fyles AW, Giaccia AJ, Hill RP, Koch CJ, Krishna MC, Krohn KA, Lewis JS, Mason RP, Melillo G, Padhani AR, Powis G, Rajendran JG, Reba R, Robinson SP, Semenza GL, Swartz HM, Vaupel P, Yang D, Croft B, Hoffman J, Liu G, Stone H, Sullivan D 2006. Hypoxia: importance in tumor biology, noninvasive measurement by imaging, and value of its measurement in the management of cancer therapy. Int J Radiat Biol 82(10):699-757.
146. Thomas S, Millard R, Pratt R, Shiferaw Y, Samaratunga R 1994. Quantitative pO2 imaging in vivo with perfluorocarbon F-19 NMR: tracking oxygen from the airway through the blood to organ tissues. Artif Cells Blood Substit Biotechnol 22(4):1029-1042.
147. Chan GY, Hughes TC, McLean KM, McFarland GA, Nguyen X, Wilkie JS, Johnson G 2006. Approaches to improving the biocompatibility of porous perfluoropolyethers for ophthalmic applications. Biomaterials 27(8):1287-1295.
148. Tirotta I, Dichiarante V, Pigliacelli C, Cavallo G, Terraneo G, Bombelli FB, Metrangolo P, Resnati G 2014. 19F Magnetic Resonance Imaging (MRI): from design of materials to clinical applications. Chem Rev 115(2):1106-1129.
149. Hannah AS, VanderLaan D, Chen Y-S, Emelianov SY 2014. Photoacoustic and ultrasound imaging using dual contrast perfluorocarbon nanodroplets triggered by laser pulses at 1064 nm. Biomed Opt Express 5(9):3042-3052.
150. Jacoby C, Temme S, Mayenfels F, Benoit N, Krafft MP, Schubert R, Schrader J, Flögel U 2014. Probing different perfluorocarbons for in vivo inflammation imaging by 19F MRI: image reconstruction, biological half-lives and sensitivity. NMR Biomed 27(3):261-271.
151. Srinivas M, Heerschap A, Ahrens ET, Figdor CG, Vries IJM 2010. 19F MRI for quantitative in vivo cell tracking. Trends Biotechnol 28(7):363-370.
152. Janjic JM, Ahrens ET 2009. Fluorine-containing nanoemulsions for MRI cell tracking. Wiley Interdiscip Rev Nanomed Nanobiotechnol 1(5):492-501.
153. Plewes DB, Kucharczyk W 2012. Physics of MRI: a primer. J Magn Reson Imaging 35(5):1038-1054.

154. Srinivas M, Boehm-Sturm P, Figdor CG, de Vries IJ, Hoehn M 2012. Labeling cells for in vivo tracking using (19)F MRI. Biomaterials 33(34):8830-8840.
155. Ruiz-Cabello J, Barnett BP, Bottomley PA, Bulte JW 2011. Fluorine (19F) MRS and MRI in biomedicine. NMR Biomed 24(2):114-129.
156. Ahrens ET, Helfer BM, O'Hanlon CF, Schirda C 2014. Clinical cell therapy imaging using a perfluorocarbon tracer and fluorine-19 MRI. Magn Reson Med 72(6):1696-1701.
157. Lichtman JW, Conchello JA 2005. Fluorescence microscopy. Nat Methods 2(12):910-919.
158. Frangioni J 2003. In vivo near-infrared fluorescence imaging. Curr Opin Chem Biol 7(5):626-634.
159. Luo S, Zhang E, Su Y, Cheng T, Shi C 2011. A review of NIR dyes in cancer targeting and imaging. Biomaterials 32(29):7127-7138.
160. TaikáLim Y, HyunáChung B 2009. Multifunctional perfluorocarbon nanoemulsions for 19 F-based magnetic resonance and near-infrared optical imaging of dendritic cells. Chem Commun (45):6952-6954.
161. Ahrens ET, Zhong J 2013. In vivo MRI cell tracking using perfluorocarbon probes and fluorine-19 detection. NMR Biomed 26(7):860-871.
162. Srinivas M, Turner MS, Janjic JM, Morel PA, Laidlaw DH, Ahrens ET 2009. In vivo cytometry of antigen-specific t cells using 19F MRI. Magn Reson Med 62(3):747-753.
163. Srinivas M, Morel PA, Ernst LA, Laidlaw DH, Ahrens ET 2007. Fluorine-19 MRI for visualization and quantification of cell migration in a diabetes model. Magn Reson Med 58(4):725-734.
164. Ahrens ET, Flores R, Xu H, Morel PA 2005. In vivo imaging platform for tracking immunotherapeutic cells. Nat Biotechnol 23(8):983-987.
165. Weibel S, Basse-Luesebrink TC, Hess M, Hofmann E, Seubert C, Langbein-Laugwitz J, Gentschev I, Sturm VJF, Ye Y, Kampf T 2013. Imaging of intratumoral inflammation during oncolytic virotherapy of tumors by 19F-magnetic resonance imaging (MRI). PLoS One 8(2):e56317.
166. Balducci A, Helfer BM, Ahrens ET, O'Hanlon CF, Wesa AK 2012. Visualizing arthritic inflammation and therapeutic response by fluorine-19 magnetic resonance imaging (19F MRI). J Inflamm (Lond) 9(1):24-34.
167. Kadayakkara DK, Ranganathan S, Young WB, Ahrens ET 2012. Assaying macrophage activity in a murine model of inflammatory bowel disease using fluorine-19 MRI. Lab Invest 92(4):636-645.
168. Ebner B, Behm P, Jacoby C, Burghoff S, French BA, Schrader J, Flögel U 2010. Early assessment of pulmonary inflammation by 19F MRI in vivo. Circ Cardiovasc Imaging 3(2):202-210.
169. Hitchens TK, Ye Q, Eytan DF, Janjic JM, Ahrens ET, Ho C 2011. 19F MRI detection of acute allograft rejection with in vivo perfluorocarbon labeling of immune cells. Magn Reson Med 65(4):1144-1153.
170. Janjic JM, Srinivas M, Kadayakkara DK, Ahrens ET 2008. Self-delivering nanoemulsions for dual fluorine-19 MRI and fluorescence detection. J Am Chem Soc 130(9):2832-2841.

171. Balducci A, Wen Y, Zhang Y, Helfer BM, Hitchens TK, Meng WS, Wesa AK, Janjic JM 2013. A novel probe for the non-invasive detection of tumor-associated inflammation. Oncoimmunology 2(2):e23034.
172. Lee S-J, Schlesinger PH, Wickline SA, Lanza GM, Baker NA 2011. Interaction of melittin peptides with perfluorocarbon nanoemulsion particles. J Phys Chem B 115(51):15271-15279.
173. Zhou H-f, Yan H, Hu Y, Springer LE, Yang X, Wickline SA, Pan D, Lanza GM, Pham CT 2014. Fumagillin prodrug nanotherapy suppresses macrophage inflammatory response via endothelial nitric oxide. ACS Nano 8(7):7305-7317.
174. Rapoport N 2012. Phase-shift, stimuli-responsive perfluorocarbon nanodroplets for drug delivery to cancer. Wiley Interdiscip Rev Nanomed Nanobiotechnol 4(5):492-510.
175. Chen J, Pan H, Lanza GM, Wickline SA 2013. Perfluorocarbon nanoparticles for physiological and molecular imaging and therapy. Adv Chronic Kidney Dis 20(6):466-478.
176. Kaneda MM, Caruthers S, Lanza GM, Wickline SA 2009. Perfluorocarbon nanoemulsions for quantitative molecular imaging and targeted therapeutics. Ann Biomed Eng 37(10):1922-1933.
177. Fang J-Y, Hung C-F, Hua S-C, Hwang T-L 2009. Acoustically active perfluorocarbon nanoemulsions as drug delivery carriers for camptothecin: drug release and cytotoxicity against cancer cells. Ultrasonics 49(1):39-46.
178. Patel SK, Williams J, Janjic JM 2013. Cell labeling for 19F MRI: new and improved approach to perfluorocarbon nanoemulsion design. Biosensors (Basel) 3(3):341-359.
179. Tadros T, Izquierdo P, Esquena J, Solans C 2004. Formation and stability of nano-emulsions. Adv Colloid Interface Sci 108-109:303-318.
180. Mason TG, Wilking JN, Meleson K, Chang CB, Graves SM 2006. Nanoemulsions: formation, structure, and physical properties. J Phys Condens Matter 18(41):R635-R666.
181. Tang SY, Shridharan P, Sivakumar M 2013. Impact of process parameters in the generation of novel aspirin nanoemulsions--comparative studies between ultrasound cavitation and microfluidizer. Ultrason Sonochem 20(1):485-497.
182. Maa Y-F, Hsu CC 1999. Performance of sonication and microfluidization for liquid-liquid emulsification. Pharm Dev Technol 4(2):233-240.
183. Sivakumar M, Tang SY, Tan KW 2014. Cavitation technology - a greener processing technique for the generation of pharmaceutical nanoemulsions. Ultrason Sonochem 21(6):2069-2083.
184. Cook EJ, Lagace AP. 1985. Liquid jet interaction chamber block. ed.: Google Patents.
185. Taylor P 1998. Ostwald ripening in emulsions. Adv Colloid Interface Sci 75(2):107-163.
186. Capek I 2004. Degradation of kinetically-stable o/w emulsions. Adv Colloid Interface Sci 107(2-3):125-155.
187. Lifshitz IM, Slyozov VV 1961. The kinetics of precipitation from supersaturated solid solutions. J Phys Chem Solids 19(1):35-50.

188. Wagner C 1961. Ostwald ripening theory. Ber Bunsenges Phys Chem 65:581-591.
189. Kabalnov A, Makarov K, Shcherbakova O, Nesmeyanov A 1990. Solubility of fluorocarbons in water as a key parameter determining fluorocarbon emulsion stability. J Fluor Chem 50(3):271-284.
190. Kabalnov AS, Shchukin ED 1992. Ostwald ripening theory: applications to fluorocarbon emulsion stability. Adv Colloid Interface Sci 38:69-97.
191. Heurtault B 2003. Physico-chemical stability of colloidal lipid particles. Biomaterials 24(23):4283-4300.
192. Frisken BJ 2001. Revisiting the method of cumulants for the analysis of dynamic light-scattering data. Appl Opt 40(24):4087-4091.
193. Koppel DE 1972. Analysis of macromolecular polydispersity in intensity correlation spectroscopy: the method of cumulants. J Chem Phys 57(11):4814.
194. nanoComposix. 2012. Guidelines for dynamic light scattering measurement and analysis. ed.: nanoComposix. http://50.87.149.212/sites/default/files/nanoComposix Guidelines for DLS Measurements and Analysis.pdf. Accessed: March 17 2015.
195. Jiang Z-X, Yu YB 2007. The design and synthesis of highly branched and spherically symmetric fluorinated oils and amphiles. Tetrahedron 63(19):3982-3988.
196. Janjic J, Ahrens ET. 2012. Compositions and methods for producing cellular labels for nuclear magnetic resonance techniques. ed.: Google Patents. WO 2009009105 A2.
197. Welin-Berger K, Bergenståhl B 2000. Inhibition of Ostwald ripening in local anesthetic emulsions by using hydrophobic excipients in the disperse phase. Int J Pharm 200(2):249-260.
198. Collett J. 2005. Poloxamer. In RC Rowe PS, SC Owen, editor Handbook of Pharmaceutical Excipients, 5 ed., USA: Pharmaceutical Press & American Pharmacists Association. p 535-538.
199. Strickley RG 2004. Solubilizing excipients in oral and injectable formulations. Pharm Res 21(2):201-230.
200. Alexandridis P, Hatton TA 1995. Poly (ethylene oxide) poly (propylene oxide) poly (ethylene oxide) block copolymer surfactants in aqueous solutions and at interfaces: thermodynamics, structure, dynamics, and modeling. Colloids Surf A Physicochem Eng Asp 96(1):1-46.
201. Uskoković V, Odsinada R, Djordjevic S, Habelitz S 2011. Dynamic light scattering and zeta potential of colloidal mixtures of amelogenin and hydroxyapatite in calcium and phosphate rich ionic milieus. Arch Oral Biol 56(6):521-532.
202. Davis MJ, Tsang TM, Qiu Y, Dayrit JK, Freij JB, Huffnagle GB, Olszewski MA 2013. Macrophage M1/M2 polarization dynamically adapts to changes in cytokine microenvironments in Cryptococcus neoformans infection. MBio 4(3):e00264-00213.
203. Berghaus LJ, Moore JN, Hurley DJ, Vandenplas ML, Fortes BP, Wolfert MA, Boons GJ 2010. Innate immune responses of primary murine macrophage-lineage cells and RAW 264.7 cells to ligands of Toll-like receptors 2, 3, and 4. Comp Immunol Microbiol Infect Dis 33(5):443-454.
204. Bonetto F, Srinivas M, Heerschap A, Mailliard R, Ahrens ET, Figdor CG, de Vries IJM 2011. A novel 19F agent for detection and quantification of human dendritic cells using magnetic resonance imaging. Int J Cancer 129(2):365-373.

205. Gerhardt GE, Lagow RJ 1978. Synthesis of the perfluoropoly (ethylene glycol) ethers by direct fluorination. J Org Chem 43(23):4505-4509.
206. Moss G. 2009. Medium-chain triglycerides. In RC Rowe PS, ME Quinn, editor Handbook of Pharmaceutical Excipients, 6th ed., Newyork: Pharmaceutical Press. p 429-431.
207. Guideline ICH Harmonised Tripartite. 2005. Validation of analytical procedures: Text and Methodology Q2 (R1). ed., The International Conference on Harmonisation of Technical Requirements for Registration of Pharmaceuticals for Human Use (ICH).
208. Zhang W 2003. Fluorous technologies for solution-phase high-throughput organic synthesis. Tetrahedron 59(25):4475-4489.
209. Zarzar LD, Sresht V, Sletten EM, Kalow JA, Blankschtein D, Swager TM 2015. Dynamically reconfigurable complex emulsions via tunable interfacial tensions. Nature 518(7540):520-524.
210. Pertsov AV, Soboleva OA, Nazarov VG, Protsenko PV 2008. Selective wetting in a hydrocarbon liquid-perfluorocarbon liquid-solid system. Colloid J 70(6):759-762.
211. Gelderblom H, Verweij J, Nooter K, Sparreboom A 2001. Cremophor EL: the drawbacks and advantages of vehicle selection for drug formulation. Eur J Cancer 37(13):1590-1598.
212. 2011. Taxol (Pacltaxel injection). ed., FDA drug safety label.
213. Ta-Chung C, Zyting C, Ling-Ming T, Tzeon-Jye C, Ruey-Kuen H, Wei-Shu W, Chueh-Chuan Y, Muh-Hwa Y, Liang-Tsai H, Jin-Hwang L 2005. Paclitaxel in a novel formulation containing less Cremophor EL as first-line therapy for advanced breast cancer: a phase II trial. Invest New Drugs 23(2):171-177.
214. Wang Y, Wu K-C, Zhao B-X, Zhao X, Wang X, Chen S, Nie S-F, Pan W-S, Zhang X, Zhang Q 2011. A novel paclitaxel microemulsion containing a reduced amount of Cremophor EL: pharmacokinetics, biodistribution, and in vivo antitumor efficacy and safety. Biomed Res Int 2011:1-10.
215. Janjic JM, Shao P, Zhang S, Yang X, Patel SK, Bai M 2014. Perfluorocarbon nanoemulsions with fluorescent, colloidal and magnetic properties. Biomaterials 35(18):4958-4968.
216. Rieger AM, Hall BE, Barreda DR 2010. Macrophage activation differentially modulates particle binding, phagocytosis and downstream antimicrobial mechanisms. Dev Comp Immunol 34(11):1144-1159.
217. Patel SK, Patrick MJ, Pollock JA, Janjic JM 2013. Two-color fluorescent (near-infrared and visible) triphasic perfluorocarbon nanoemuslions. J Biomed Opt 18(10):101312.
218. Patrick MJ, Janjic JM, Teng H, O'Hear MR, Brown CW, Stokum JA, Schmidt BF, Ahrens ET, Waggoner AS 2013. Intracellular pH measurements using perfluorocarbon nanoemulsions. J Am Chem Soc 135(49):18445-18457.
219. Mujumdar RB, Ernst LA, Mujumdar SR, Lewis CJ, Waggoner AS 1993. Cyanine dye labeling reagents: sulfoindocyanine succinimidyl esters. Bioconjug Chem 4(2):105-111.
220. GA Casay DS, G Patonay. 1994. Near-infrared fluorescent probes. In Lakowicz J, editor Topics in Fluorescence Spectroscopy, ed., New York: Plenum Press. p 183-217.

221. Shao P, Bai M 2012. Photostable, hydrophilic and functional near infrared quaterrylenediimide-cored dendrimers for biomedical imaging. Chem Commun (Camb) 48(76):9498-9500.
222. Stennett EM, Ciuba MA, Levitus M 2014. Photophysical processes in single molecule organic fluorescent probes. Chem Soc Rev 43(4):1057-1075.
223. Vasudeva K, Andersen K, Zeyzus-Johns B, Hitchens TK, Patel SK, Balducci A, Janjic JM, Pollock JA 2014. Imaging neuroinflammation in vivo in a neuropathic pain rat model with near-infrared fluorescence and 19F magnetic resonance. PLoS One 9(2):e90589.
224. Wang T, Bai J, Jiang X, Nienhaus GU 2012. Cellular uptake of nanoparticles by membrane penetration: a study combining confocal microscopy with FTIR spectroelectrochemistry. ACS Nano 6(2):1251-1259.
225. Raynal I, Prigent P, Peyramaure S, Najid A, Rebuzzi C, Corot C 2004. Macrophage endocytosis of superparamagnetic iron oxide nanoparticles: mechanisms and comparison of ferumoxides and ferumoxtran-10. Invest Radiol 39(1):56-63.
226. Billiau A, Matthys P 2001. Modes of action of Freund's adjuvants in experimental models of autoimmune diseases. J Leukoc Biol 70(6):849-860.
227. Barin JG, Baldeviano GC, Talor MV, Wu L, Ong S, Quader F, Chen P, Zheng D, Caturegli P, Rose NR 2012. Macrophages participate in IL-17-mediated inflammation. Eur J Immunol 42(3):726-736.
228. Morris CJ. 2003. Carrageenan-induced paw edema in the rat and mouse. Inflammation Protocols, ed.: Springer. p 115-121.
229. Swirski FK, Nahrendorf M, Etzrodt M, Wildgruber M, Cortez-Retamozo V, Panizzi P, Figueiredo J-L, Kohler RH, Chudnovskiy A, Waterman P 2009. Identification of splenic reservoir monocytes and their deployment to inflammatory sites. Science 325(5940):612-616.